NASA Technical Paper 1075

Forebody and Afterbody Solutions of the Navier-Stokes Equations for Supersonic Flow Over Blunt Bodies in a Generalized Orthogonal Coordinate System

Peter A. Gnoffo

FEBRUARY 1978

NASA

NASA Technical Paper 1075

Forebody and Afterbody Solutions of the Navier-Stokes Equations for Supersonic Flow Over Blunt Bodies in a Generalized Orthogonal Coordinate System

Peter A. Gnoffo
Langley Research Center
Hampton, Virginia

NASA
National Aeronautics
and Space Administration

Scientific and Technical
Information Office

1978

CONTENTS

SUMMARY

The coordinate transformation procedure and solution technique described herein have been shown to be well suited for the calculation of the complete flow field surrounding various two-dimensional and axisymmetric bodies. This conclusion is supported by the good comparisons obtained between predicted values and experimental data for pressure coefficient distribution and heat-transfer distribution on a cylinder and for density distributions and shock standoff distance on spheres. The solutions for the flow over the Viking aeroshell and a Jupiter probe were obtained by simply adjusting five transformation constants without having to perform any adjustment on boundary conditions. The versatility of the technique in being able to model many different axisymmetric blunt body shapes and its ability to calculate both the forebody and wake flow over these shapes represent a significant advance in aerothermodynamic technology.

An upper limit on Reynolds number on the order of 1000 is imposed because of an inability to resolve a thin boundary layer with a reasonable number of computational mesh points. A lower limit on Reynolds number on the order of 100 is imposed so that continuum theory is applicable. An upper limit on Mach number approximately equal to 4.0 is imposed because of a tendency to calculate negative static enthalpies in the process of capturing the bow shock for large Mach numbers. These limitations are a consequence of the numerical method used and not of the coordinate system itself. A more refined numerical method could ease some of these restrictions.

INTRODUCTION

The calculation of the complete flow field surrounding axisymmetric or two-dimensional blunt bodies in a supersonic stream has been a goal of fluid dynamicists which has only recently been made practically attainable through advances in high-speed computers. Inviscid shock-layer solutions (refs. 1 to 4), viscous shock-layer solutions (ref. 5), and solutions of the full Navier-Stokes equations (ref. 6) have been obtained for the shock layer ahead of various blunt configurations. Many of those solutions have been specialized for various flow regimes which range from high Reynolds number flow (ref. 7) to low Reynolds number flow of a viscous rarefied gas (ref. 8).

Mathematical descriptions of the flow in the wake of a blunt body are more difficult to obtain. Boundary-layer approximations which are successfully used in the shock layer are not applicable to a large portion of the wake where viscous forces are dominant (ref. 9); however, early predictions of the wake flow used these approximations (refs. 10 to 13). Weiss (ref. 14) improved on this approximation and reported temperature field calculations which compared more closely with experimental data than previous work. Allen (ref. 15) solved the full Navier-Stokes equations in the steady state for the laminar wake behind a two-dimensional rectangular block. That solution specified a boundary-layer profile under a uniform stream as an inflow condition.

This "patchwork" approach of solving the complete flow field, that is, the matching of separate, specialized solutions for the different areas of the flow field, was noted by Scala and Gordon (ref. 16). As an alternative approach, they presented a solution to the complete time-dependent Navier-Stokes equations for the transient supersonic flow around a right circular cylinder. Kitchens extended that approach to obtain the steady-state solution to the same problem (ref. 17).

It should be noted here that a patchwork approach for obtaining the complete flow field is a useful technique. In fact, these specialized techniques almost always lead to a more efficient, faster running numerical solution because fewer computational points are needed to define the flow field and many terms can be omitted from the Navier-Stokes equations by using an order of magnitude type approach (as is done in deriving the boundary-layer equations) in certain areas of the flow field. However, the major disadvantage of the patchwork approach is that it is often difficult to determine where and how the various specialized solutions are to be matched.

Existing solutions to the Navier-Stokes equations for the entire flow field have been obtained for simple body shapes. (See ref. 18.) An accurate description of the flow field over complex body shapes is facilitated by the choice of an appropriate coordinate system. Gnoffo (ref. 19) outlined many of the advantages and disadvantages that are associated with the use of various coordinate systems which can be used as the basis for the numerical differencing of the Navier-Stokes equations over complex axisymmetric or two-dimensional body shapes. Some important considerations are the ability of the coordinate system to concentrate mesh points near the body for resolving the boundary layer and near regions of sharp curvature to treat rapid expansions. Orthogonality of coordinate lines to the body simplifies the boundary-condition specification.

A generalized orthogonal natural coordinate system was presented in reference 19 which gives close analytic approximations to various complex body shapes. The body shape approximations avoid the problems of discontinuous slope or curvature which occur in many aerodynamic configurations and yet are able to closely approximate these shapes. The purpose of this study is to show that this coordinate system can in fact be used to obtain the complete flow field over complex body shapes.

A computational technique has been developed which uses this coordinate system for obtaining the solution of the Navier-Stokes equations for the entire flow field. A computer program has been written to describe flow over two-dimensional body shapes or axisymmetric body shapes. Comparisons with experimental data have been made to verify the technique and to ascertain where problems due to the nature of the flow or due to numerical instabilities can occur. Flow fields around the Viking aeroshell and a candidate configuration for a Jupiter probe are calculated and presented. The analysis has been restricted to supersonic flow of a perfect gas with free-stream Mach number less than 4.2

and Reynolds numbers of the order of 100 to 1000, for reasons that will be discussed subsequently.

SYMBOLS

A_n, B, C	transformation constants, nondimensionalized by R_N^*
a	speed of sound, nondimensionalized by V_∞^*
C_D	drag coefficient defined in appendix F
C_p	pressure coefficient, $\equiv \dfrac{p_b^* - p_\infty^*}{\frac{1}{2} \rho_\infty^* V_\infty^{*2}}$
c_p^*	specific heat at constant pressure, J/kg-K
e	error term defined in equation (22); also exponential
h	metric coefficient, nondimensionalized by R_N^*
h_c^*	heat-transfer coefficient, W/m^2-K
I	total enthalpy, nondimensionalized by V_∞^{*2}
i	static enthalpy, nondimensionalized by V_∞^{*2}
k^*	thermal conductivity, W/m-K
L	body length, nondimensionalized by R_N^*
L_1	intermediate body length, nondimensionalized by R_N^*
M_∞	free-stream Mach number, $\equiv V_\infty^*/a^*$
N	integer in transformation equation
N_{Kn}	Knudsen number, $\equiv \lambda_\infty^*/R_N^*$
N_{Pr}	Prandtl number, $\equiv \mu^* c_p^*/k^*$
$N_{Re,\infty}$	Reynolds number based on nose radius of curvature, $\equiv \rho_\infty^* V_\infty^* R_N^*/\mu^*$
NI	total number of mesh points in θ-direction
NJ	total number of mesh points in η-direction
n	integer in transformation equation

n^*	distance normal to body, m
p	pressure, nondimensionalized by $\rho_\infty^* V_\infty^{*2}$
q_c^*	convective heat transfer, W/m^2
R	radius of curvature, nondimensionalized by R_N^*
R^*	gas constant, J/kg-K
r,θ,ϕ	coordinates in transformed space
S^*	maximum cross-sectional area, m^2
s	arc length, nondimensionalized by R_N^*
T	temperature, nondimensionalized by T_∞^*
T_∞^*	free-stream temperature, K
t	time, nondimensionalized by R_N^*/V_∞^*
U	component of velocity in x-direction, nondimensionalized by V_∞^*
u	component of velocity in θ-direction, nondimensionalized by V_∞^*
V	component of velocity in y-direction, nondimensionalized by V_∞^*
V_∞^*	free-stream velocity, m/s
v	component of velocity in r-direction, nondimensionalized by V_∞^*
x,y,z	Cartesian coordinates, nondimensionalized by R_N^*
Y	metric coefficient, nondimensionalized by R_N^*
Y_{max}	maximum body radius, nondimensionalized by R_N^*
α_t	thermal accommodation coefficient
β	coordinate stretching parameter in equation (17)
γ	ratio of specific heats
Δ_s^*	shock-layer thickness, m
ε	smoothing parameter in equations (23)
η	stretched coordinate in computational plane defined in equation (17)

λ^*	mean free path, m
μ	viscosity, nondimensionalized by μ_∞^*
μ_∞^*	free-stream viscosity
ρ	density, nondimensionalized by ρ_∞^*
ρ_∞^*	free-stream density, kg/m^3
τ	shear stress
ψ	angle defining velocity vectors

Superscripts:

n	time step index
*	signifies dimensional quantity (MKS system)

Subscripts:

aw	adiabatic wall
B	base
b	body
calc	calculated
exp	experimental
i	index on mesh point in θ-direction
j	index on mesh point in η-direction
N	nose
n	index on transformation constants
o	refers to slip boundary condition
r	refers to conditions along constant θ and ϕ
s	shock
stag	stagnation
θ	refers to conditions along constant r and ϕ

ϕ	refers to conditions along constant r and θ
∞	free stream

Bars over symbols generally denote average values; however, in appendix B the bars denote variables at a predicted time step. (See step 1 of appendix B.) Arrows over a symbol denote vectors.

COORDINATE SYSTEM

Coordinate Transformation

A generalized curvilinear orthogonal coordinate system which can be used for approximating various axisymmetric and two-dimensional body shapes is presented in reference 19. The body shapes include spheres, ellipses, spherically capped cones, flat-faced cylinders with rounded corners, circular disks, and planetary probe vehicles. The transformation from the (θ,r,ϕ) domain to the (x,y,z) domain for an axisymmetric coordinate system is written as

$$\left.\begin{aligned} x(\theta,r,\phi) &= (-B \sinh r + C \cosh r) \cos\theta - \sum_{n=2}^{N} A_n e^{nr} \cos n\theta \\ y(\theta,r,\phi) &= \left[(B \cosh r - C \sinh r) \sin\theta + \sum_{n=2}^{N} A_n e^{nr} \sin n\theta\right] \cos\phi \\ z(\theta,r,\phi) &= \left[(B \cosh r - C \sinh r) \sin\theta + \sum_{n=2}^{N} A_n e^{nr} \sin n\theta\right] \sin\phi \end{aligned}\right\} \tag{1}$$

where N is a positive integer greater than two and A_n, B, and C are arbitrary constants. A two-dimensional transformation to the x,y plane is obtained by setting $\phi = 0$.

Lines of constant r are transformed to circles in the x,y plane as r increases without limit in the negative direction. Because terms involving e^{nr} vanish and $-\sinh r$ approaches $\cosh r$ as r increases without limit in the negative direction, equations (1) can be written approximately as

$$\left.\begin{aligned} x(\theta,r) &\approx \left[(B + C) \cosh r\right] \cos\theta \qquad (r \ll 0) \\ y(\theta,r) &\approx \left[(B + C) \cosh r\right] \sin\theta \qquad (r \ll 0) \end{aligned}\right\} \tag{2}$$

The line segment $r = 0$, $0 \leqq \theta \leqq 2\pi$ is transformed into a two-dimensional body in the x,y plane and becomes one boundary of the computational space in the θ,r plane. An axisymmetric body is defined by mapping the line segment $r = 0$, $0 \leqq \theta \leqq \pi$ to the x,y plane and rotating the image around the x-axis 2π radians. Thus,

Two dimensions, $0 \leqq \theta \leqq 2\pi$

$$\left.\begin{aligned} x_b &= C \cos \theta - \sum_{n=2}^{N} A_n \cos n\theta \\ y_b &= B \sin \theta + \sum_{n=2}^{N} A_n \sin n\theta \end{aligned}\right\} \tag{3}$$

Axisymmetric, $0 \leqq \theta \leqq \pi$ and $0 \leqq \phi \leqq 2\pi$

$$\left.\begin{aligned} x_b &= C \cos \theta - \sum_{n=2}^{N} A_n \cos n\theta \\ y_b &= \left(B \sin \theta + \sum_{n=2}^{N} A_n \sin n\theta\right) \cos \phi \\ z_b &= \left(B \sin \theta + \sum_{n=2}^{N} A_n \sin n\theta\right) \sin \phi \end{aligned}\right\} \tag{4}$$

The lines $\theta = 0$ and $\theta = 2\pi$ will therefore form two boundaries of the computational space for two-dimensional problems. The $\theta = 0$ plane, $\theta = \pi$ plane, $\phi = 0$ plane, and $\phi = 2\pi$ plane are the boundaries in computational space for axisymmetric bodies.

The final boundary of the computational space is chosen as $r = r_\infty$. It will be shown in a later section that r_∞ can be mapped to negative infinity with one additional transformation. Such a transformation will cause the inflow-outflow boundary to be mapped to a circle of infinite radius as seen from equations (2). This transformation will simplify the problem of specifying inflow and outflow boundary conditions. An example of a typical transformed body shape is shown in figure 1 with the associated coordinate system.

It should also be noted that the transformation can be written as a conformal mapping for two dimensions. By setting

$w = x(\theta,r) + iy(\theta,r)$

$D = (B + C)/2$

$A_1 = (B - C)/2$

and simplifying, the following equation is obtained:

$$w = De^{iz} - \sum_{n=1}^{N} A_n e^{-inz}$$

where $z = \theta + ir$ and $i = \sqrt{-1}$

The definition and orientation of the velocity components are determined by the coordinate system. The u component of velocity is directed along a line of constant r in the direction of increasing θ. The v component of velocity is directed along a line of constant θ in the direction of increasing r. Thus, from figure 1, it can be seen that the direction of positive u is counterclockwise around the body and the direction of positive v is toward the body.

The detailed derivation of the metric coefficients for this coordinate system appears in appendix A. It is important to note that the metric coefficient h_θ is equal to the metric coefficient h_r. This equality greatly reduces the number of calculations that will have to be made when solving the governing flow equations.

Determination of Body Shape

Methods for determining a large variety of body shapes are discussed in detail in reference 19. For the sake of completeness, the methods for determining the body shapes used herein are presented.

For all $A_n = 0$, the transformation from the θ,r plane to the x,y plane results in families of ellipses. For $B = C$, the transformation produces a circle of radius B. For $B \neq C$, the transformation results in an ellipse of eccentricity e_c where

$$e_c = \left(\frac{1 - B^2}{C^2}\right)^{1/2}$$

Calculations have been made for configurations approximating planetary probe vehicles as shown in figures 2 and 3. The true body shape in figure 3 is taken from reference 20. These approximations were obtained by considering the following parametric equations for a body shape

$$\left.\begin{aligned} x_b &= C\cos\theta - \sum_{n=2}^{4} A_n \cos n\theta \\ y_b &= B\sin\theta + \sum_{n=2}^{4} A_n \sin n\theta \end{aligned}\right\} \qquad (5)$$

which correspond to equations (3) and (4) with $N = 4$ and $\phi = 0$.

In figure 4 some basic geometric parameters of a planetary probe are presented. The radius of curvature of any point on the body can be expressed as

$$R(\theta) = \left| \frac{\left[1 + (dy/dx)^2\right]^{3/2}}{d^2y/dx^2} \right| = \left| \frac{\left[(\partial x/\partial\theta)^2 + (\partial y/\partial\theta)^2\right]^{3/2}}{(\partial x/\partial\theta)(\partial^2 y/\partial\theta^2) - (\partial y/\partial\theta)(\partial^2 x/\partial\theta^2)} \right| \tag{6}$$

By defining a nose radius of curvature R_N, a base radius of curvature R_B, a vehicle length L, a maximum body radius Y_{max}, and the length from the nose to the location of the maximum body radius on the symmetry line L_1, it is possible to solve for A_2, A_3, A_4, B, and C. To specify Y_{max}, it is also necessary to determine θ_{max} so that $y_b(\theta_{max}) = Y_{max}$ and $dy_b/d\theta(\theta_{max}) = 0$. These specifications result in the following equations:

$$-\frac{(B + 4A_4 + 3A_3 + 2A_2)^2}{-C + 16A_4 + 9A_3 + 4A_2} = R(0) = R_B \tag{7}$$

$$\frac{(-B + 4A_4 - 3A_3 + 2A_2)^2}{C + 16A_4 - 9A_3 + 4A_2} = R(\pi) = R_N \tag{8}$$

$$2C - 2A_3 = L \tag{9}$$

$$A_4 \sin 4\theta_{max} + A_3 \sin 3\theta_{max} + A_2 \sin 2\theta_{max} + B \sin \theta_{max} = Y_{max} \tag{10}$$

$$4A_4 \cos 4\theta_{max} + 3A_3 \cos 3\theta_{max} + 2A_2 \cos 2\theta_{max} + B \cos (\theta_{max}) = 0 \tag{11}$$

$$\begin{aligned} &-A_4 \cos 4\theta_{max} - A_3 \cos 3\theta_{max} - A_2 \cos 2\theta_{max} + C \cos \theta_{max} \\ &+ A_4 - A_3 + A_2 + C = L_1 \end{aligned} \tag{12}$$

Equations (7) to (12) can be solved by use of Newton's method to obtain A_4, A_3, A_2, B, C, and θ_{max}. When choosing the values of R_N, R_B, and L_1, it may prove necessary to pick adjusted values which will give a better overall approximation to the desired body shape. As pointed out in reference 19, it is not possible to accurately model all body shapes with equations (3). Therefore, once the constants are obtained, the analytic approximation has to be compared with the desired body shape to determine whether agreement is satisfactory. A trial-and-error approach was established whereby values for R_N, R_B, and L_1 were varied over a narrow range of values which were close to the measured values for the desired body shape and then the resulting analytic approximation was compared with the true body shape. The analytic approximations shown in figures 2 and 3 were obtained in this manner. The parameters which were specified and the resulting values for B, C, A_2, A_3, and A_4 that correspond to these figures are presented in table I.

ANALYTIC DEVELOPMENT

In order to test the usefulness of the coordinate system just described, a solution to the supersonic flow at an angle of attack of 0° over blunt, axisymmetric, or two-dimensional bodies is obtained. The analysis is simplified by making the following assumptions:

N_{Pr} = Constant

$\mu_B = 0$

$\mu = \mu(T)$ (using Sutherland's law)

Perfect gas

No radiative heat transfer

The quantity μ_B is the bulk viscosity coefficient which is set equal to zero in keeping with general practices.

Strictly speaking, the Navier-Stokes equations refer only to the momentum equations. By following Vincenti and Kruger (ref. 21), the term Navier-Stokes equations is used herein to refer to the complete set of partial differential equations that describe the motion of a viscous heat conducting fluid. These equations, expressed in a generalized orthogonal coordinate system, are nondimensionalized as follows:

$$h = h^*/R_N^* \qquad Y = Y^*/R_N^* \qquad t = R_N^*/V_\infty^* t^*$$

$$\rho = \rho^*/\rho_\infty^* \qquad u = u^*/V_\infty^* \qquad v = v^*/V_\infty^*$$

$$I = I^*/V_\infty^{*2} \qquad p = p^*/\rho_\infty^* V_\infty^{*2} \qquad \mu = \mu^*/\mu_\infty^*$$

The Navier-Stokes equations written in the transformed coordinate system may be obtained from references 22 and 23. Since only the steady-state solution to the governing equations is desired, a term involving the time rate of change of pressure has been omitted from the energy equation in order to simplify the numerical procedure. The other time derivative terms must be kept in order to retain the hyperbolic nature of the governing equations in time. The omission of the transient pressure term prohibits an accurate modeling of the transient flow situation. However, as noted by Crocco (ref. 24), the unsteady equations are used strictly as a guide in choosing an iteration procedure. Allen (ref. 15) notes that the difference scheme can be modified to approximate a different unsteady equation as long as the steady-state difference equations and boundary conditions are correct.

The convective terms in the governing equations are written in conservation form as recommended in reference 25 for shock capturing whereas the dissipative terms are expanded so that they no longer retain conservation form.

In preliminary numerical calculations it was found that finite-difference approximations of terms involving products of metric coefficients with the conservation flow variables (that is, $\partial(h\rho u)/\partial\theta$, $\partial\left[h^2(p + \rho u^2)\right]/\partial\theta$, and $\partial(h^2\rho uv)/\partial\theta$) caused large errors in the numerical solution. This problem was most obvious in the free-stream flow ahead of the shock. Values for free-stream density along the stagnation streamline were in error by as much as 4 percent. The corresponding Mach numbers differed from the free-stream condition by as much as 10 percent for $M_\infty = 2$ and $\gamma = 1.4$. The governing equations were rewritten in a form which separated derivatives of metric coefficients from derivatives of conservation flow variables. The derivatives of the metric coefficients are analytic functions of θ and r which are easily obtained from equations (A4). The derivatives of the conservation flow variables are approximated by finite-difference formulas. The governing partial differential equations expanded in this manner become for:

Continuity:

$$\frac{\partial\rho}{\partial t} = \frac{-1}{h}\left[\frac{\partial(\rho u)}{\partial\theta} + \frac{\partial(\rho v)}{\partial r} + \rho u\left(\frac{1}{Y}\frac{\partial Y}{\partial\theta} + \frac{1}{h}\frac{\partial h}{\partial\theta}\right) + \rho v\left(\frac{1}{Y}\frac{\partial Y}{\partial r} + \frac{1}{h}\frac{\partial h}{\partial r}\right)\right] \tag{13}$$

θ-momentum:

$$\begin{aligned}
\frac{\partial(\rho u)}{\partial t} = {} & \frac{-1}{h}\left[\frac{\partial(p + \rho u^2)}{\partial\theta} + \frac{\partial(\rho uv)}{\partial r} + \rho u^2\left(\frac{1}{Y}\frac{\partial Y}{\partial\theta} + \frac{1}{h}\frac{\partial h}{\partial\theta}\right) + \rho uv\left(\frac{1}{Y}\frac{\partial Y}{\partial r} + \frac{2}{h}\frac{\partial h}{\partial r}\right) - \rho v^2\frac{1}{h}\frac{\partial h}{\partial\theta}\right] + \frac{1}{h^2 N_{Re,\infty}}\left\{\frac{4}{3}\mu\frac{\partial^2 u}{\partial\theta^2}\right. \\
& + \frac{1}{3}\mu\frac{\partial^2 v}{\partial\theta\,\partial r} + \mu\frac{\partial^2 u}{\partial r^2} + \frac{4}{3}\left(\frac{\partial\mu}{\partial\theta} + \mu\frac{1}{Y}\frac{\partial Y}{\partial\theta}\right)\frac{\partial u}{\partial\theta} + \left(\frac{\partial\mu}{\partial r} + \mu\frac{1}{Y}\frac{\partial Y}{\partial r}\right)\frac{\partial u}{\partial r} + \left(\frac{1}{3}\mu\frac{1}{Y}\frac{\partial Y}{\partial r} + \frac{7}{3}\mu\frac{1}{h}\frac{\partial h}{\partial r} + \frac{\partial\mu}{\partial r}\right)\frac{\partial v}{\partial\theta} \\
& - \left(\frac{7}{3}\mu\frac{1}{h}\frac{\partial h}{\partial\theta} + \frac{2}{3}\frac{\partial\mu}{\partial\theta}\right)\frac{\partial v}{\partial r} + \left[\frac{-2}{3}\mu\frac{1}{h}\frac{\partial^2 h}{\partial\theta^2} - \frac{2}{3}\mu\left(\frac{1}{h}\frac{\partial h}{\partial\theta}\right)^2 - \frac{4}{3}\mu\left(\frac{1}{Y}\frac{\partial Y}{\partial\theta}\right)^2 - \frac{2}{3}\mu\frac{1}{Y}\frac{\partial^2 Y}{\partial\theta^2} - \mu\frac{1}{h}\frac{\partial^2 h}{\partial r^2}\right. \\
& \left. + \frac{2}{3}\mu\frac{1}{h}\frac{\partial h}{\partial\theta}\frac{1}{Y}\frac{\partial Y}{\partial\theta} - \mu\frac{1}{h}\frac{\partial h}{\partial r}\frac{1}{Y}\frac{\partial Y}{\partial r} - \frac{2}{3}\frac{\partial\mu}{\partial\theta}\frac{1}{Y}\frac{\partial Y}{\partial\theta} - \frac{2}{3}\frac{\partial\mu}{\partial\theta}\frac{1}{h}\frac{\partial h}{\partial\theta} - \frac{\partial\mu}{\partial r}\frac{1}{h}\frac{\partial h}{\partial r}\right]u + \left[\frac{1}{3}\mu\frac{1}{h}\frac{\partial^2 h}{\partial\theta\,\partial r}\right. \\
& - \frac{2}{3}\mu\frac{1}{Y}\frac{\partial^2 Y}{\partial\theta\,\partial r} - \frac{4}{3}\mu\frac{1}{Y}\frac{\partial Y}{\partial\theta}\frac{1}{Y}\frac{\partial Y}{\partial r} - \frac{1}{3}\mu\frac{1}{h}\frac{\partial h}{\partial\theta}\frac{1}{Y}\frac{\partial Y}{\partial r} - \frac{2}{3}\mu\frac{1}{h}\frac{\partial h}{\partial\theta}\frac{1}{h}\frac{\partial h}{\partial r} + 2\mu\frac{1}{h}\frac{\partial h}{\partial r}\frac{1}{Y}\frac{\partial Y}{\theta} \\
& \left.\left. - \frac{2}{3}\frac{\partial\mu}{\partial\theta}\frac{1}{Y}\frac{\partial Y}{\partial r} + \frac{4}{3}\frac{\partial\mu}{\partial\theta}\frac{1}{h}\frac{\partial h}{\partial r} - \frac{\partial\mu}{\partial r}\frac{1}{h}\frac{\partial h}{\partial\theta}\right]v\right\}
\end{aligned} \tag{14}$$

r-momentum:

$$
\begin{aligned}
\frac{\partial(\rho v)}{\partial t} = \frac{-1}{h}\bigg[&\frac{\partial(\rho uv)}{\partial\theta} + \frac{\partial(p + \rho v^2)}{\partial r} + \rho uv\left(\frac{1}{Y}\frac{\partial Y}{\partial\theta} + \frac{2}{h}\frac{\partial h}{\partial\theta}\right) + \rho v^2\left(\frac{1}{Y}\frac{\partial Y}{\partial r} + \frac{1}{h}\frac{\partial h}{\partial r}\right) - \rho u^2\frac{1}{h}\frac{\partial h}{\partial r}\bigg] \\
&+ \frac{1}{h^2 N_{Re,\infty}}\Bigg\{\frac{4}{3}\mu\frac{\partial^2 v}{\partial r^2} + \frac{1}{3}\mu\frac{\partial^2 u}{\partial\theta\,\partial r} + \mu\frac{\partial^2 v}{\partial\theta^2} - \left(\frac{2}{3}\frac{\partial\mu}{\partial r} + \frac{7}{3}\mu\frac{1}{h}\frac{\partial h}{\partial r}\right)\frac{\partial u}{\partial\theta} \\
&+ \left(\frac{1}{3}\mu\frac{1}{Y}\frac{\partial Y}{\partial\theta} + \frac{7}{3}\mu\frac{1}{h}\frac{\partial h}{\partial\theta} + \frac{\partial\mu}{\partial\theta}\right)\frac{\partial u}{\partial r} + \left(\frac{\partial\mu}{\partial\theta} + \mu\frac{1}{Y}\frac{\partial Y}{\partial\theta}\right)\frac{\partial v}{\partial\theta} + \frac{4}{3}\left(\mu\frac{1}{Y}\frac{\partial Y}{\partial r} + \frac{\partial\mu}{\partial r}\right)\frac{\partial v}{\partial r} \\
&+ \bigg[\frac{1}{3}\mu\frac{1}{h}\frac{\partial^2 h}{\partial\theta\,\partial r} - \frac{2}{3}\mu\frac{1}{Y}\frac{\partial^2 Y}{\partial\theta\,\partial r} - \frac{4}{3}\mu\frac{1}{Y}\frac{\partial Y}{\partial\theta}\frac{1}{Y}\frac{\partial Y}{\partial r} - \frac{1}{3}\mu\frac{1}{Y}\frac{\partial Y}{\partial\theta}\frac{1}{h}\frac{\partial h}{\partial r} \\
&- \frac{2}{3}\mu\frac{1}{h}\frac{\partial h}{\partial\theta}\frac{1}{h}\frac{\partial h}{\partial r} + 2\mu\frac{1}{h}\frac{\partial h}{\partial\theta}\frac{1}{Y}\frac{\partial Y}{\partial r} - \frac{2}{3}\frac{\partial\mu}{\partial r}\frac{1}{Y}\frac{\partial Y}{\partial\theta} + \frac{4}{3}\frac{\partial\mu}{\partial r}\frac{1}{h}\frac{\partial h}{\partial\theta} - \frac{\partial\mu}{\partial\theta}\frac{1}{h}\frac{\partial h}{\partial r}\bigg]u \\
&+ \bigg[\frac{-2}{3}\mu\frac{1}{h}\frac{\partial^2 h}{\partial r^2} - \mu\frac{1}{h}\frac{\partial^2 h}{\partial\theta^2} - \frac{2}{3}\mu\frac{1}{Y}\frac{\partial^2 Y}{\partial r^2} - \frac{4}{3}\mu\left(\frac{1}{Y}\frac{\partial Y}{\partial r}\right)^2 - \frac{2}{3}\mu\left(\frac{1}{h}\frac{\partial h}{\partial r}\right)^2 \\
&+ \frac{2}{3}\mu\frac{1}{h}\frac{\partial h}{\partial r}\frac{1}{Y}\frac{\partial Y}{\partial r} - \mu\frac{1}{h}\frac{\partial h}{\partial\theta}\frac{1}{Y}\frac{\partial Y}{\partial\theta} - \frac{2}{3}\frac{\partial\mu}{\partial r}\frac{1}{Y}\frac{\partial Y}{\partial r} - \frac{2}{3}\frac{\partial\mu}{\partial r}\frac{1}{h}\frac{\partial h}{\partial r} - \frac{\partial\mu}{\partial\theta}\frac{1}{h}\frac{\partial h}{\partial\theta}\bigg]v\Bigg\}
\end{aligned}
\tag{15}
$$

Energy:

$$
\begin{aligned}
\frac{\partial\rho I}{\partial t} = \frac{-1}{h}\bigg[&\frac{\partial\rho uI}{\partial\theta} + \frac{\partial\rho vI}{\partial r} + \rho uI\left(\frac{1}{Y}\frac{\partial Y}{\partial\theta} + \frac{1}{h}\frac{\partial h}{\partial\theta}\right) + \rho vI\left(\frac{1}{Y}\frac{\partial Y}{\partial r} + \frac{1}{h}\frac{\partial h}{\partial r}\right)\bigg] + \frac{1}{h^2 N_{Re,\infty}}\Bigg(\mu\Bigg\{\frac{-2}{3}\frac{\partial u}{\partial\theta}\frac{\partial v}{\partial r} \\
&- \frac{2}{3}\frac{1}{Y}\frac{\partial Y}{\partial\theta}u\frac{\partial v}{\partial r} + v\frac{\partial^2 v}{\partial\theta^2} - \frac{2}{3}u\frac{\partial^2 v}{\partial\theta\,\partial r} + \left(\frac{\partial v}{\partial\theta}\right)^2 + v\frac{\partial v}{\partial\theta}\left(\frac{1}{Y}\frac{\partial Y}{\partial\theta} - \frac{2}{h}\frac{\partial h}{\partial\theta}\right) + \frac{\partial u}{\partial r}\frac{\partial v}{\partial\theta} \\
&+ u\frac{\partial v}{\partial\theta}\left(-\frac{2}{3}\frac{1}{Y}\frac{\partial Y}{\partial r} + \frac{1}{3}\frac{1}{h}\frac{\partial h}{\partial r}\right) - v^2\left[\frac{1}{h}\frac{\partial h}{\partial\theta}\frac{1}{Y}\frac{\partial Y}{\partial\theta} + \frac{1}{h}\frac{\partial^2 h}{\partial\theta^2} - \left(\frac{1}{h}\frac{\partial h}{\partial\theta}\right)^2\right] + v\frac{\partial u}{\partial r}\frac{1}{Y}\frac{\partial Y}{\partial\theta} \\
&+ v\frac{\partial^2 u}{\partial\theta\,\partial r} - v\frac{\partial u}{\partial\theta}\left(\frac{2}{3}\frac{1}{Y}\frac{\partial Y}{\partial r} - \frac{1}{3}\frac{1}{h}\frac{\partial h}{\partial r}\right) + uv\bigg[-\frac{2}{3}\frac{1}{Y}\frac{\partial^2 Y}{\partial\theta\,\partial r} + \frac{1}{3}\bigg(\frac{1}{h}\frac{\partial h}{\partial r}\frac{1}{Y}\frac{\partial Y}{\partial\theta} \\
&- \frac{1}{h}\frac{\partial h}{\partial\theta}\frac{1}{h}\frac{\partial h}{\partial r} + \frac{1}{h}\frac{\partial^2 h}{\partial\theta\,\partial r}\bigg)\bigg] + \frac{4}{3}\left[u\frac{\partial^2 u}{\partial\theta^2} + \left(\frac{\partial u}{\partial\theta}\right)^2 - \frac{1}{h}\frac{\partial h}{\partial\theta}u\frac{\partial u}{\partial\theta}\right] - \frac{2}{3}u^2\bigg[\frac{1}{Y}\frac{\partial^2 Y}{\partial\theta^2} \\
&+ \frac{1}{h}\frac{\partial h}{\partial\theta}\frac{1}{Y}\frac{\partial Y}{\partial\theta} + \frac{1}{h}\frac{\partial^2 h}{\partial\theta^2} - \left(\frac{1}{h}\frac{\partial h}{\partial\theta}\right)^2\bigg]\Bigg\} + \frac{\partial\mu}{\partial\theta}\bigg[v\frac{\partial v}{\partial\theta} - \frac{2}{3}u\frac{\partial v}{\partial r} - \frac{1}{h}\frac{\partial h}{\partial\theta}v^2 + v\frac{\partial u}{\partial r}
\end{aligned}
\tag{16}
$$

(Equation continued on next page)

$$
\begin{aligned}
&+ uv\frac{1}{h}\frac{\partial h}{\partial r} - \frac{2}{3}uv\bigg(\frac{1}{Y}\frac{\partial Y}{\partial r} + \frac{1}{h}\frac{\partial h}{\partial r}\bigg) + \frac{4}{3}u\frac{\partial u}{\partial \theta} - \frac{2}{3}u^2\bigg(\frac{1}{Y}\frac{\partial Y}{\partial \theta} + \frac{1}{h}\frac{\partial h}{\partial \theta}\bigg)\Bigg]\\
&+ \mu\Bigg\{\frac{4}{3}\bigg[v\frac{\partial^2 v}{\partial r^2} + \bigg(\frac{\partial v}{\partial r}\bigg)^2 - \frac{1}{h}\frac{\partial h}{\partial r}v\frac{\partial v}{\partial r}\bigg] - \frac{2}{3}\bigg(\frac{\partial u}{\partial \theta}\frac{\partial v}{\partial r} + \frac{1}{Y}\frac{\partial Y}{\partial \theta}u\frac{\partial v}{\partial r}\bigg) + \frac{1}{3}\frac{1}{h}\frac{\partial h}{\partial \theta}u\frac{\partial v}{\partial r}\\
&+ u\frac{\partial^2 v}{\partial \theta\,\partial r} + \frac{\partial u}{\partial r}\frac{\partial v}{\partial \theta} + \frac{1}{Y}\frac{\partial Y}{\partial r}u\frac{\partial v}{\partial \theta} - \frac{2}{3}v^2\bigg[\frac{1}{h}\frac{\partial h}{\partial r}\frac{1}{Y}\frac{\partial Y}{\partial r} + \frac{1}{Y}\frac{\partial^2 Y}{\partial r^2} + \frac{1}{h}\frac{\partial^2 h}{\partial r^2} - \bigg(\frac{1}{h}\frac{\partial h}{\partial r}\bigg)^2\bigg]\\
&- \frac{1}{3}v\frac{\partial u}{\partial r}\bigg(\frac{2}{Y}\frac{\partial Y}{\partial \theta} - \frac{1}{h}\frac{\partial h}{\partial \theta}\bigg) - \frac{2}{3}\bigg(v\frac{\partial^2 u}{\partial \theta\,\partial r} + \frac{1}{Y}\frac{\partial Y}{\partial r}v\frac{\partial u}{\partial \theta}\bigg) + \frac{1}{3}uv\bigg(\frac{1}{h}\frac{\partial h}{\partial \theta}\frac{1}{Y}\frac{\partial Y}{\partial r} - \frac{2}{Y}\frac{\partial^2 Y}{\partial \theta\,\partial r}\\
&- \frac{1}{h}\frac{\partial h}{\partial \theta}\frac{1}{h}\frac{\partial h}{\partial r} + \frac{1}{h}\frac{\partial^2 h}{\partial \theta\,\partial r}\bigg) + u\frac{\partial^2 u}{\partial r^2} + \bigg(\frac{\partial u}{\partial r}\bigg)^2 + u\frac{\partial u}{\partial r}\bigg(\frac{1}{Y}\frac{\partial Y}{\partial r} - \frac{2}{h}\frac{\partial h}{\partial r}\bigg) - u^2\bigg[\frac{1}{h}\frac{\partial h}{\partial r}\frac{1}{Y}\frac{\partial Y}{\partial r}\\
&+ \frac{1}{h}\frac{\partial^2 h}{\partial r^2} - \bigg(\frac{1}{h}\frac{\partial h}{\partial r}\bigg)^2\bigg]\Bigg\} + \frac{\partial \mu}{\partial r}\Bigg\{\frac{4}{3}v\frac{\partial v}{\partial r} + u\frac{\partial v}{\partial \theta} - \frac{2}{3}\bigg[v^2\bigg(\frac{1}{Y}\frac{\partial Y}{\partial r} + \frac{1}{h}\frac{\partial h}{\partial r}\bigg) + v\frac{\partial u}{\partial \theta}\bigg]\\
&+ \frac{1}{3}uv\bigg(\frac{1}{h}\frac{\partial h}{\partial \theta} - \frac{2}{Y}\frac{\partial Y}{\partial \theta}\bigg) + u\frac{\partial u}{\partial r} - u^2\frac{1}{h}\frac{\partial h}{\partial r}\Bigg\}\Bigg) + \frac{1}{h^2 N_{Re,\infty}N_{Pr}}\Bigg(\mu\Bigg\{\frac{\partial I}{\partial \theta}\frac{1}{Y}\frac{\partial Y}{\partial \theta} + \frac{\partial^2 I}{\partial \theta^2}\\
&- \bigg[v\frac{\partial^2 v}{\partial \theta^2} + \bigg(\frac{\partial v}{\partial \theta}\bigg)^2 + v\frac{\partial v}{\partial \theta}\frac{1}{Y}\frac{\partial Y}{\partial \theta} + u\frac{\partial^2 u}{\partial \theta^2} + \bigg(\frac{\partial u}{\partial \theta}\bigg)^2 + u\frac{\partial u}{\partial \theta}\frac{1}{Y}\frac{\partial Y}{\partial \theta}\bigg]\Bigg\} + \frac{\partial \mu}{\partial \theta}\bigg[\frac{\partial I}{\partial \theta} - \bigg(v\frac{\partial v}{\partial \theta}\\
&+ u\frac{\partial u}{\partial \theta}\bigg)\bigg] + \mu\Bigg\{\frac{\partial I}{\partial r}\frac{1}{Y}\frac{\partial Y}{\partial r} + \frac{\partial^2 I}{\partial r^2} - \bigg[v\frac{\partial^2 v}{\partial r^2} + \bigg(\frac{\partial v}{\partial r}\bigg)^2 + v\frac{\partial v}{\partial r}\frac{1}{Y}\frac{\partial Y}{\partial r} + u\frac{\partial^2 u}{\partial r^2} + \bigg(\frac{\partial u}{\partial r}\bigg)^2\\
&+ u\frac{\partial u}{\partial r}\frac{1}{Y}\frac{\partial Y}{\partial r}\bigg]\Bigg\} + \frac{\partial \mu}{\partial r}\bigg[\frac{\partial I}{\partial r} - \bigg(v\frac{\partial v}{\partial r} + u\frac{\partial u}{\partial r}\bigg)\bigg]\Bigg) \qquad (16)
\end{aligned}
$$

The numerical solutions obtained by differencing the equations in this manner brought all free-stream properties within 1 percent of an undisturbed field.

It should be noted that equations (13) to (16) are not in strict conservation form in the sense that when they are applied to an undisturbed uniform flow, they do not return a uniform flow after one iteration. An error on the order of $(\Delta\theta)^2 + (\Delta r)^2$ is introduced. For example, a uniform two-dimensional flow written in the coordinate system as expressed by equations (1) with $B = 1$, $C = 1$, $A_n = 0$ has the following properties:

$u = -\sin\theta$

$v = -\cos\theta$

$\rho = 1$

$h = e^{-r}$

$Y = 1$

After one iteration (predictor step) on these conditions, the continuity equation yields

$$\rho^{n+1} = \rho^{n} - \Delta t e^{r}\left\{\left[\frac{-\sin(\theta + \Delta\theta) + \sin(\theta - \Delta\theta)}{2\,\Delta\theta}\right] + \cos\theta\right\}$$

$$\rho^{n+1} \cong \rho^{n} + \Delta t e^{r}\cos\theta\left(\frac{\sin\Delta\theta}{\Delta\theta} - 1\right)$$

$$\rho^{n+1} = \rho^{n} + \Delta t e^{r}\cos\theta\left(\frac{-\Delta\theta^{2}}{3!} + \frac{\Delta\theta^{4}}{5!} + \ldots\right)$$

These errors have shown no sign of seriously disturbing the final solution.

An additional coordinate transformation is utilized which simplifies the treatment of the inflow and outflow boundary conditions and gives some control on the density of mesh points near the body in a direction normal to the body. A new coordinate η is defined so that

$$r = \beta \log_e \eta \qquad (\eta = e^{r/\beta};\quad \beta > 0) \tag{17}$$

where $-\infty < r \leqq 0$ and $0 < \eta \leqq 1$. This coordinate stretching maps the inflow and outflow boundary conditions to infinity. All boundary conditions at infinity are known. This coordinate stretching does not affect the orthogonality of the coordinate system. Such a transformation was used by Kitchens (ref. 17) in order to eliminate rarefaction waves in a wake induced by fixing free-stream boundary conditions at a finite distance downstream of a body. Derivatives with respect to r are written as derivatives with respect to η as follows:

$$\left.\begin{aligned}
&\frac{\partial(\ )}{\partial r} = \frac{\partial(\ )}{\partial\eta}\,\frac{d\eta}{dr} \\
&\frac{\partial^{2}(\ )}{\partial r\,\partial\theta} = \frac{\partial}{\partial\eta}\left[\frac{\partial(\ )}{\partial\theta}\right]\frac{\partial\eta}{\partial r} \\
&\frac{\partial^{2}(\ )}{\partial r^{2}} = \frac{\partial}{\partial\eta}\left[\frac{\partial(\ )}{\partial\eta}\,\frac{d\eta}{dr}\right]\frac{d\eta}{dr} = \frac{\partial^{2}(\ )}{\partial\eta^{2}}\left(\frac{\partial\eta}{\partial r}\right)^{2} + \frac{\partial(\ )}{\partial\eta}\,\frac{1}{\beta}\,\frac{d\eta}{dr} \\
&\frac{d\eta}{dr} = \frac{1}{\beta}\,e^{r/\beta} = \frac{\eta}{\beta}
\end{aligned}\right\} \tag{18}$$

All derivatives of flow properties with respect to r in equations (13) to (16) are now replaced by their counterparts in equations (18).

On the line of symmetry the θ-momentum equation is not solved because $u = 0$. For axisymmetric problems, the limiting forms of the conservation equations for mass, r-momentum, and energy must be obtained because the factor $1/Y$ which appears in many of the terms in those equations increases without limit as θ approaches 0 or π. (Note that $Y = 1$ for two-dimensional problems.) The limiting form of these equations is easily obtained by applying L'Hospitals rule to all terms in these equations which are multiplied by $1/Y$.

NUMERICAL TECHNIQUE

A modification of the Brailovskaya scheme which was introduced by Allen and Cheng (refs. 15 and 26) was applied to equations (13) to (16) to obtain the numerical solutions presented herein. The differencing technique is presented in appendix B. This particular method was chosen because the viscous stability limit in the Navier-Stokes equations is removed in Cartesian coordinates for constant viscosity. Allen and Cheng point out that when there is a large expansion of the flow around a corner or when the density in the near wake is small, the stability limit on the time step based on the diffusion terms can be severely restrictive as compared with the stability limit based on the inviscid terms. The elimination of this stability limit makes their modification to Brailovskaya's scheme very attractive. The stability limit on the time step for the inviscid portion of the governing equations is derived in reference 27. This limit can be written in Cartesian coordinates as

$$\Delta t \leqq \frac{1}{\dfrac{|U|}{\Delta x} + \dfrac{|V|}{\Delta y} + a\sqrt{\left(\dfrac{1}{\Delta x}\right)^2 + \left(\dfrac{1}{\Delta y}\right)^2}} \qquad (19)$$

In the transformed coordinate system, this limit is written as

$$\Delta t \leqq \frac{1}{\dfrac{|u|}{h\ \Delta\theta} + \dfrac{|v|\eta}{h\beta\ \Delta\eta} + \dfrac{a}{h}\sqrt{\left(\dfrac{1}{\Delta\theta}\right)^2 + \left(\dfrac{\eta}{\beta\ \Delta\eta}\right)^2}} \qquad (20)$$

This transformed stability limit was obtained by substituting the terms for velocity and arc length in the transformed plane that correspond to the equivalent terms in the Cartesian plane. The stability limit from equation (20) was used in all calculations without any indication of numerical instability. Also, comparisons were made in regions of severe expansion (around the corner of the Viking aeroshell, for example) and it was found that the actual time increment used exceeded the viscous limit by more than a factor of 20 (see table II), where the viscous stability limit is (ref. 27)

$$\Delta t \leq \frac{0.410 N_{Pr} N_{Re,\infty}}{\frac{\gamma\mu}{\rho}\left(\frac{1}{\Delta x^2} + \frac{1}{\Delta y^2}\right)} \approx \frac{0.410 N_{Pr} N_{Re,\infty}}{\frac{\gamma\mu}{\rho h^2}\left(\frac{1}{\Delta\theta^2} + \frac{\eta^2}{\beta^2 \Delta\eta^2}\right)} \tag{21}$$

Convergence Criteria

The modified form of the Brailovskaya method is used herein to obtain the steady-state solution of the governing equations. Because the solution is approached in an iterative manner, it is necessary to establish some criteria to insure that the results have in fact converged to a steady state. A variable e is defined so that

$$e = \left|\frac{\rho^{n+1} - \rho^{n}}{\rho^{n}}\right|_{\substack{\max \\ i,j}} \tag{22}$$

The variation of e as a function of iteration number is shown in figure 5 for different mesh sizes. The solution is said to be converged when the value of e becomes less than some small number $\bar{e}$. Care must be exercised in choosing the value of $\bar{e}$ as can be seen in figure 5. The value of $\bar{e}$ should be chosen as some small number which is below the level where the e variation begins to level out. For example, in the case of the e variation for a grid of 51 × 50 with the stretching parameter $\beta = 1$, it can be seen that e starts to level out after 2000 iterations at 0.0002. When it was finally established that the variation of e had leveled and was starting a much slower decrease, a value of $\bar{e}$ equal to 0.0001 was chosen as the convergence criteria. A comparison of results for $\left.\frac{\partial i}{\partial \eta}\right|_{b}$ is given in table III at various iteration levels to show the effect that various values of $\bar{e}$ have on the static enthalpy derivative at the wall. The enthalpy derivative should be very sensitive to any changes occurring in the flow field. The results from table III indicate that for a mesh size of 51 × 100, there is less than a 2-percent difference between the solution after 6000 iterations and the solution after 4000 iterations.

Fourth-Order Smoothing

Preliminary calculations indicated that some kind of damping or smoothing routine was necessary to eliminate numerical instabilities, especially in the vicinity of the shock. A nonphysical damping function was used to eliminate these instabilities. (See ref. 1.) Terms of fourth order in the spatial grid are used to smooth results after every iteration as indicated in the following equations.

$$\left.\begin{aligned}
\rho^{n+1}_{i,j} &= \tilde{\rho}^{n+1}_{i,j} - \varepsilon\left[(\Delta\theta)^4 \frac{\partial^4(\rho^n)}{\partial\theta^4} + (\Delta\eta)^4 \frac{\partial^4(\rho^n)}{\partial\eta^4}\right]_{i,j} \\
U^{n+1}_{i,j} &= \left\{(\tilde{\rho}\tilde{u})^{n+1}_{i,j} - \varepsilon\left[(\Delta\theta)^4 \frac{\partial^4(\rho u^n)}{\partial\theta^4} + (\Delta\eta)^4 \frac{\partial^4(\rho u^n)}{\partial\eta^4}\right]_{i,j}\right\} \Bigg/ \rho^{n+1}_{i,j} \\
v^{n+1}_{i,j} &= \left\{(\tilde{\rho}\tilde{v})^{n+1}_{i,j} - \varepsilon\left[(\Delta\theta)^4 \frac{\partial^4(\rho v^n)}{\partial\theta^4} + (\Delta\eta)^4 \frac{\partial^4(\rho v^n)}{\partial\eta^4}\right]_{i,j}\right\} \Bigg/ \rho^{n+1}_{i,j} \\
I^{n+1}_{i,j} &= \left\{(\tilde{\rho}\tilde{I})^{n+1}_{i,j} - \varepsilon\left[(\Delta\theta)^4 \frac{\partial^4(\rho I^n)}{\partial\theta^4} + (\Delta\eta)^4 \frac{\partial^4(\rho I^n)}{\partial\eta^4}\right]_{i,j}\right\} \Bigg/ \rho^{n+1}_{i,j}
\end{aligned}\right\} \qquad (23)$$

The tilde symbol over the flow variables indicates the undamped results from the second step of the difference scheme.

The five-point formulas for the fourth-order derivatives have the form

$$(\Delta\theta)^4 \frac{\partial^4(\rho^n)}{\partial\theta} = \rho^n_{i+2,j} + \rho^n_{i-2,j} - 4\left(\rho^n_{i+1,j} + \rho^n_{i-1,j}\right) + 6\rho^n_{i,j} \qquad (24)$$

When the five-point formula for the fourth-order derivative involves property values across a line of symmetry, then the appropriate symmetric or antisymmetric value of the property must be substituted into equation (24); otherwise, nonzero values for $\partial p/\partial\theta$ and $\partial\rho/\partial\theta$ on the symmetry line will result.

For $j = 1$ or $j = NJ$, no damping is used in the η-direction. For $j \leqq 2$ or $j \geqq NJ - 1$, the five-point formula for $(\Delta\eta)^4 \frac{\partial^4(\;)}{\partial\eta^4}$ cannot be used because it involves points outside of the computational space. Four-point formulas for third-order derivatives in the η-direction are used when $j = 2$ or $j = NJ - 1$. These formulas have the form

$$(\Delta\eta)^3 \frac{\partial^3\rho}{\partial\eta^3} = \rho_{i,j+2} - \rho_{i,j-1} - 3(\rho_{i,j+1} - \rho_{i,j}) \qquad (j = 2) \qquad (25)$$

$$-(\Delta\eta)^3 \frac{\partial^3\rho}{\partial\eta^3} = \rho_{i,j-2} - \rho_{i,j+1} - 3(\rho_{i,j-1} - \rho_{i,j}) \qquad (j = NJ - 1) \qquad (26)$$

When $j = 2$, the expression for $(\Delta\eta)^3 \dfrac{\partial^3(\ )}{\partial\eta^3}$ from equation (25) is substituted for the term $(\Delta\eta)^4 \dfrac{\partial^4(\ )}{\partial\eta^4}$ in equations (23); when $j = NJ - 1$, the expression for $-(\Delta\eta)^3 \dfrac{\partial^3(\ )}{\partial\eta^3}$ from equation (26) is substituted for the term $(\Delta\eta)^4 \dfrac{\partial^4(\ )}{\partial\eta^4}$ in equations (23).

In a stability analysis on the inviscid equations, Barnwell (ref. 1) shows that the damping coefficient must satisfy the inequality

$$0 \leqq \varepsilon \leqq 1/24 \tag{27}$$

Ideally, the smallest value of ε in this range which allows a stable smooth solution should be used. However, because of the large amount of computer time required to run a problem to convergence, no systematic search for an "ideal" value of ε was undertaken. It was found that $\varepsilon = 0.001$ would result in stable solutions for most of the cases considered herein.

Initial Conditions

Transformation of uniform velocity field.- In order to establish realistic initial conditions, it is necessary to resolve a uniform flow in the x,y plane to the equivalent condition in the θ,r plane. This can be accomplished in the following manner. Let a uniform velocity field of magnitude V_∞ approach a body in the x,y plane at 0° angle of attack. All angles are measured from $\theta = 0$ in a counterclockwise direction. Let ψ be defined as the angle of the vector tangent to a line of constant r in the direction of increasing θ. From consideration of figure 6, it may be determined that

$$\left.\begin{aligned} u &= V_\infty \cos\psi \\ v &= -V_\infty \sin\psi \end{aligned}\right\} \tag{28}$$

It is now necessary to determine $\cos\psi$ and $\sin\psi$ as a function of θ and r.

The differentials dx and dy along a line of constant r can be determined from equations (1) as

$$\left.\begin{aligned} dx &= \left[(B \sinh r - C \cosh r)\sin\theta + \sum_{n=2}^{N} nA_n e^{nr} \sin n\theta\right] d\theta \\ dy &= \left[(B \cosh r - C \sinh r)\cos\theta + \sum_{n=2}^{N} nA_n e^{nr} \cos n\theta\right] d\theta \end{aligned}\right\} \tag{29}$$

From figure 6 and equations (29) and (A4), it can be shown that

$$\left.\begin{aligned} \cos\psi &= \frac{dx}{\sqrt{dx^2 + dy^2}} = \frac{(B\sinh r - C\cosh r)\sin\theta + \sum_{n=2}^{N} nA_n e^{nr}\sin n\theta}{h} \\ \sin\psi &= \frac{dy}{\sqrt{dx^2 + dy^2}} = \frac{(B\cosh r - C\sinh r)\cos\theta + \sum_{n=2}^{N} nA_n e^{nr}\cos n\theta}{h} \end{aligned}\right\} \qquad (30)$$

Thus, the initial uniform flow field may be resolved into its components u and v in the transformed system by using equations (28) and (30).

Initialization procedure.- When the first set of calculations were performed on the inviscid equations, the initial conditions were prescribed as a uniform velocity field everywhere except at the body where v was set equal to 0. This situation corresponded to a body suddenly materializing at rest in a supersonic stream at time $t = 0$. Problems developed as the shock started to form near the body. Negative values of static enthalpy occurred between the shock and the forebody; thus, any further calculations are terminated. A probable cause of these negative values was in the way surface boundary conditions are obtained. In most "shock capturing" numerical methods, in which no discrete shocks are assumed but rather are allowed to be smeared over several mesh points, it is common to see a slight overshoot and undershoot of properties on either side of the shock (ref. 25). An extrapolation procedure was used to obtain pressure on the body but this extrapolation was invalid when the properties used in the extrapolation were in the region of the developing shock.

Thus, either the method of obtaining the boundary condition had to be changed or the initial flow conditions had to be altered. Kitchens (ref. 17) took the first approach and allowed the surface velocity components to vary linearly from the uniform flow values to zero after some period of time t_1. This specification corresponds to a porous body with the amount of mass flux through the surface decreasing to zero between times $t = 0$ and $t = t_1$. The no-slip condition is then specified on the surface for times $t \geqq t_1$. However, it was found to be simpler in the present program to alter the initial conditions in such a way that the shock would develop further away from the body. This was accomplished by calculating the transformed velocity components and multiplying the result by $1 - \eta$. Then, the total enthalpy at a point was set equal to the free-stream static enthalpy plus one-half of the velocity squared. Thus,

$$\left.\begin{aligned} u &= (1 - \eta)V_\infty \cos\psi \\ v &= -(1 - \eta)V_\infty \sin\psi \\ I &= \frac{1}{(\gamma - 1)M_\infty^2} + \frac{1}{2}(u^2 + v^2) \end{aligned}\right\} \qquad (31)$$

The variable $\eta = 1$ corresponds to the body so that the no-slip condition is imposed. When $\eta = 0$, the velocities are unchanged from the uniform flow conditions. In the θ,η computational plane the initialized velocities vary linearly from $\eta = 0$ to $\eta = 1$. In the x,y plane this alteration corresponds to an exponential damping of the uniform velocity field as the body is approached from the far field. This specification does not model any physically realistic situation but does allow a steady-state solution to be obtained.

Boundary Conditions and Mesh Positioning

An example of positioning of mesh points in the θ,η computational plane is shown in figure 7. Note that mesh points are positioned on the line segments $\theta = 0$ and $\theta = \pi$ and that mesh points are positioned one-half cell width away from the body, $\eta = 1$, and the inflow and outflow boundary, $\eta = 0$. This is the same technique used by Allen (ref. 15) and some explanation for the reasoning behind the approach will be given. Allen begins the derivation of the numerical approach by writing the conservation laws of mass, momentum, and energy in integral form. He works directly from the integral form of the equations to obtain all the difference approximations. It should be noted that the same set of difference equations presented herein could be obtained from the conservation laws of mass, momentum, and energy written in differential form. However, the integral approach gives an additional insight to the derivation of the difference equations which can be lost if various second-order accurate difference approximations to derivatives that are obtained from Taylor series expansions are routinely substituted into the differential form of the conservation equations.

All values of properties at a mesh point represent the average value of the property in the cell. Flux terms across the sides of a cell are written in terms of the average values. For example,

$$\rho u_{i+\frac{1}{2},j} = \frac{1}{2}\left[(\overline{\rho u})_{i+1,j} + (\overline{\rho u})_{i,j}\right]$$

where $\overline{\rho u}$ represents the average value in the cell and ρu is the mass flux from the i cell to the i + 1 cell.

When these values for fluxes and derivatives at the boundaries of a cell are substituted into the integral form of the conservation laws, the difference formulations of the conservation equations are obtained. For example, when substituting into the integral form of the equation for the conservation of mass in Cartesian coordinates, one finally obtains

$$\frac{\partial \rho}{\partial t} = \frac{-1}{\Delta x}\,\rho U\Bigg|_{i-\frac{1}{2},j}^{i+\frac{1}{2},j} - \frac{1}{\Delta y}\,\rho V\Bigg|_{i,j-\frac{1}{2}}^{i,j+\frac{1}{2}}$$

$$= \frac{-1}{\Delta x}\left[\frac{1}{2}\left(\rho U_{i+1,j} + \rho U_{i,j}\right) - \frac{1}{2}\left(\rho U_{i,j} + \rho U_{i-1,j}\right)\right] - \frac{1}{\Delta y}\left[\frac{1}{2}\left(\rho V_{i,j+1} + \rho V_{i,j}\right)\right.$$

$$\left. - \frac{1}{2}\left(\rho V_{i,j} + \rho V_{i,j-1}\right)\right] = \frac{-1}{2\ \Delta x}\left(\rho U_{i+1,j} - \rho U_{i-1,j}\right) - \frac{1}{2\ \Delta y}\left(\rho V_{i,j+1} - \rho V_{i,j-1}\right)$$

As can be seen, a second-order accurate central difference approximation results for the partial derivatives $\partial \rho U/\partial x$ and $\partial \rho V/\partial y$ which, as stated before, could have been obtained directly from the differential form of the conservation laws. In like manner the second derivative of U with respect to x would be written

$$\left(\frac{\partial^2 U}{\partial x^2}\right)_{i,j} = \frac{1}{\Delta x}\left(\frac{\partial U}{\partial x}\right)\Bigg|_{i-\frac{1}{2},j}^{i+\frac{1}{2},j} = \frac{1}{\Delta x}\left[\frac{U_{i+1,j} - U_{i,j}}{\Delta x} - \frac{U_{i,j} - U_{i-1,j}}{\Delta x}\right]$$

$$= \frac{U_{i+1,j} - 2U_{i,j} + U_{i-1,j}}{\Delta x^2}$$

which is the second-order accurate central difference approximation to that derivative.

In deriving the difference approximations to the derivatives in the governing equations, the values of fluxes and derivatives of velocities on the sides of the computational cell are the basis of the approximation. Thus, Allen (ref. 15) points out "The greatest advantage of the integral formulation is the conceptual aid it gives in applying boundary conditions. It indicates that wall boundaries would be better placed along cell edges rather than through mesh points."

Consequently, in the generalized orthogonal coordinate system used herein all the property derivatives which appear in equations (13) to (16), except for θ derivatives on a line of symmetry, were approximated on the basis of the values of properties on the sides of a cell wall. All derivatives of metric coefficients are evaluated analytically. In most cases, that is, for all the interior points, the values at the cell wall are calculated by using the average values of properties in the cells on either side of the wall. Methods for establishing cell wall values at the boundaries are discussed in appendix C.

Symmetry Conditions

The computational boundaries along the lines $\theta = 0$ and $\theta = \pi$ correspond to a line of symmetry in the flow. The cell centers are placed on these boundaries to facilitate the calculations of the limiting form of the governing equations for axisymmetric flow situations. The symmetry conditions are

$\rho_{1-n,j} = \rho_{1+n,j}$ $\qquad$ $\rho_{NI+n,j} = \rho_{NI-n,j}$

$V_{1-n,j} = V_{1+n,j}$ $\qquad$ $V_{NI+n,j} = V_{NI-n,j}$

$p_{1-n,j} = p_{1+n,j}$ $\qquad$ $p_{NI+n,j} = p_{NI-n,j}$

$I_{1-n,j} = I_{1+n,j}$ $\qquad$ $I_{NI+n,j} = I_{NI-n,j}$

$u_{1-n,j} = -u_{1+n,j}$ $\qquad$ $u_{NI+n,j} = -u_{NI-n,j}$

$u_{1,j} = 0$ $\qquad$ $u_{NI,j} = 0$

In preliminary calculations it was found that a more accurate stagnation line solution with smoother property distributions along the body could be obtained if the derivatives with respect to θ were calculated by using a fourth-order accurate central difference formula. If a second-order accurate central difference formula is used to obtain derivatives with respect to θ across the symmetry line, then $\partial(\rho u)/\partial\theta$, $\partial(\rho uv)/\partial\theta$, and $\partial u/\partial\theta$ are calculated by using information from only one adjacent cell. A fourth-order accurate central difference approximation to the θ derivatives feeds information from two adjacent cells to the symmetry line calculations. At $i = 1$, for example,

$$\frac{\partial(\rho u)}{\partial\theta} = \frac{1}{12\,\Delta\theta}(-\rho u_3 + 8\rho u_2 - 8\rho u_0 + \rho u_{-1}) + O(\Delta\theta^4)$$

$$= \frac{1}{12\,\Delta\theta}(-2\rho u_3 + 16\rho u_2) + O(\Delta\theta^4)$$

This differencing scheme does not follow the integral approach explained in the earlier sections. However, it was felt that the improved solutions obtained in this manner justified the special treatment of the symmetry line.

RESULTS AND DISCUSSION

A computational technique based on the numerical method described in the previous section has been programmed for use in the transformed coordinate system. The program has been written to describe supersonic flow over two-dimensional or axisymmetric body shapes. Comparisons with experimental data are presented which verify the technique. Flow fields around the Viking aeroshell and a candidate configuration for a Jupiter probe are also calculated and presented. A discussion of the program's range of applicability along with the presentation of some computational results follows.

Range of Applicability

Practical limitations on storage space and execution time on the computer restrict the number of mesh points which can be used to define a flow field. The program requires 75 000 octal words of central memory for a mesh size of 51 × 50 and 121 000 octal words of central memory for a mesh size of 51 × 100. Execution time on the Cyber 175 with an optimization for fast execution is approximately 0.9 sec per iteration per 1000 grid points.

The stretching parameter β makes it possible to concentrate many grid points near the body at the expense of producing a sparse distribution of mesh points far away from the body. Some examples of the effects of the stretching parameter on mesh positioning are presented in table IV. For a fixed number of mesh points in the η-direction, it can be seen that as β is decreased, the outermost mesh points are drawn closer to the body. Consequently, a lower limit on β must be imposed in order that the shock may be captured and the flow in the wake computed.

By using a Blasius type solution for cases where boundary-layer theory applies, it can be shown that the nondimensional laminar boundary-layer thickness over an axisymmetric or two-dimensional blunt body is on the order of $M_\infty \Big/ \sqrt{N_{Re,\infty,R_N}{}^*}$. An adequate resolution of the boundary layer requires the placement of several mesh points across the actual boundary-layer thickness. Therefore, a large number of mesh points in the η-direction and a small value of the stretching parameter β are needed to position enough grid points in the boundary layer for very large Reynolds number flows. As indicated earlier in table IV, the use of coordinate stretching alone may pull all the mesh points too close to the body and prevent an adequate description of the bow shock shape and flow in the wake. For example, some typical flow field results indicate that the bow shock is stretched over three to four grid points. Morduchow and Libby (ref. 28) show that if one assumes that continuum assumptions apply in a shock that is no less than seven mean free paths thick, then the Mach number of the flow must be less than 1.3. They express the mean free path of a molecule ahead of the shock as

$$\lambda_\infty{}^* = \frac{1}{0.35} \frac{\mu_\infty{}^*}{\rho_\infty{}^*} \sqrt{\frac{\pi}{8R^*T_\infty{}^*}} \tag{32}$$

By expressing

$$\frac{\mu_\infty^*}{\rho_\infty^*} = \frac{M_\infty\sqrt{\gamma R^* T_\infty^*} R_N^*}{N_{Re,\infty}}$$

the Knudsen number N_{Kn} is obtained as

$$N_{Kn} = \frac{\lambda_\infty^*}{R_N^*} = \frac{1}{0.35}\sqrt{\frac{\gamma\pi}{8}}\,\frac{M_\infty}{N_{Re,\infty}} \tag{33}$$

Since the nondimensional shock thickness is on the order of the Knudsen number, this relationship enables one to make an approximation of the size of the region over which the shock is smeared. Admittedly, the governing equations used herein are not sufficient to resolve the flow through the shock. However, resolution of the bow shock is needed to avoid smearing the shock throughout a large portion of the shock layer. Therefore, for the purposes of resolving the flow details with the tools of this analysis, computations are restricted to low Reynolds number flows.

The free-stream Reynolds number, however, cannot be allowed to become too small or continuum theory, upon which the Navier-Stokes equations are based, is not valid. Probstein defines a Knudsen number in terms of a mean free path in the shock layer divided by the shock-layer thickness,

$$N_{Kn} = \frac{\lambda_s^*}{\Delta_s^*} \approx \frac{\lambda_\infty^*}{R_N^*} \approx \frac{M_\infty}{N_{Re,\infty}}$$

and uses this parameter to roughly delimit various flow regimes (refs. 29 and 30). In particular, he defines two flow regimes which are within the capabilities of this analysis and place a lower limit on the Reynolds number range. In the viscous layer regime "the shock layer is a fully viscous continuum amenable to treatment with the complete Navier-Stokes equations, and the shock wave may be treated as a discontinuity across which the Hugoniot (shock) relations apply" (ref. 30). This regime is delimited by

$$\frac{M_\infty}{N_{Re,\infty}} \approx \frac{\lambda_s^*}{\Delta_s^*} << \sqrt{\frac{\rho_\infty^*}{\rho_s^*}} \lesssim 0(1) < 1$$

In the incipient merged layer regime, the shock layer is still treated as a continuum but the shock can no longer be considered a discontinuity satisfying the classical Rankine-Hugoniot relations. This regime is delimited by

$$\frac{M_\infty}{N_{Re,\infty}} \approx \frac{\lambda_s^*}{\Delta_s^*} << 1$$

On the other hand, when

$$\frac{M_\infty}{N_{Re,\infty}} \approx \frac{\lambda_s^*}{\Delta_s^*} \approx 1$$

the fully merged layer regime is entered and it is incorrect to assume a continuum state although Probstein cites several papers which indicate that the Navier-Stokes equations can be used to obtain estimates for skin friction and heat transfer, and to obtain mean density and velocity distributions.

It should be noted that as the flow expands around the body into the wake, the mean free path can increase by approximately a factor of 20; this increase corresponds to the change of $\mu^*/\rho^*\sqrt{T^*}$ from the forebody stagnation region to the wake. Thus, one could be in the viscous layer or incipient merged layer regime in the forebody and enter the equivalent of a fully merged layer regime in the wake.

In order to keep the present analysis simple, the no-slip wall boundary conditions on velocity and temperature have been applied. In fact, the condition for zero velocity slip has been used to establish the specialized form of the normal velocity derivatives in the vicinity of the wall. Probstein (ref. 30) derives a condition for negligible slip as

$$\frac{\lambda_s^*}{\Delta_s^*} << \sqrt{\frac{T_s^*}{T_b^*}}$$

In all the cases considered herein, $T_s^*/T_b^* \geqq 1$. However, it is emphasized that this relationship does not mean that slip does not exist as an identifiable phenomenon but only that its effect on mean aerodynamic quantities is not large. Schaaf and Chambré (ref. 31) roughly bound a slip flow regime on the basis of experimental evidence by

$$0.01 < \frac{M_\infty}{\sqrt{N_{Re,\infty}}} < 0.1 \qquad (N_{Re,\infty} > 1)$$

Some of the experimental data used as a basis of comparison in the next section fall within this range and modifications to the solution technique are discussed in that section. A more detailed examination of the effects of slip in this Mach number and Reynolds number range will be presented with the results of that comparison.

A Reynolds number range may therefore be summarized as follows:

$$0(100) \leqq N_{Re,\infty} \leqq 0(1000)$$

where the upper limit is imposed because of an inability to resolve a thin boundary layer and the lower limit is imposed so that continuum theory is applicable. A correction for velocity and temperature slip may be required at the lower Reynolds number limit, depending on other properties of the flow field.

The process of capturing a strong shock and spreading the discontinuity over several mesh points can result in a small overshoot and undershoot of properties on either side of the shock. The magnitude of the overshoot decreases with increasing damping factor and increases with increasing mesh point separation. The bow shock is closest to the body, in a region of relatively dense mesh spacing, in the stagnation region; as the bow shock wraps around the body and approaches the Mach angle, it moves away from the body into an area of relatively sparse concentration of mesh points. It has been observed that as the bow shock forms in high Mach number flow, negative static enthalpies are calculated in the vicinity of the shock. These negative static enthalpies are a consequence of the velocity overshoot on the inflow side of the shock.

The static enthalpy is computed by subtracting $(u^2 + v^2)/2$ from the total enthalpy I. The total enthalpy is approximately constant across the shock and is equal to

$$I_\infty = \frac{1}{(\gamma - 1)M_\infty^2} + \frac{1}{2}$$

By defining V_1 as the calculated velocity ahead of the shock, the percent overshoot of the velocity O_p is defined as

$$O_p = 100\,\frac{(V_1{*} - V_\infty{*})}{V_\infty{*}} = 100(V_1 - 1)$$

The calculated static enthalpy ahead of the shock is then expressed as

$$i_1 = I_1 - \frac{1}{2}V_1^2 \approx \frac{1}{(\gamma - 1)M_\infty^2} + \frac{1}{2} - \frac{1}{2}\left(\frac{O_p}{100} + 1\right)^2 \approx \frac{1}{(\gamma - 1)M_\infty^2} - \frac{O_p}{100} - \frac{(O_p)^2}{20\ 000}$$

Consequently, if

$$O_p > \frac{100}{(\gamma - 1)M_\infty^2}$$

a negative static enthalpy is calculated and the program execution is terminated.

As can be seen in these relationships, the allowable percent overshoot decreases as M_∞ increases. It has been found that with a grid size of 51 × 50, the onset of the problem of calculating negative static enthalpies ahead of a bow shock occurs at $M_\infty \approx 4$ for a sphere and $M_\infty \approx 3.5$ for a cylinder with $\gamma = 1.4$. The Mach number limit is slightly higher for a sphere because the bow shock stands closer to the body in an area with a relatively large concentration of mesh points.

It should be noted that improvements to the numerical approach can be made to extend the Mach number and Reynolds number range and to reduce the execution time on the computer. The technique can be reprogrammed to run on the STAR 100 computer with a potential execution time reduction of an order of magnitude (ref. 32). The numerical approach can also be altered so that the stability limit on Δt is increased by using an alternating direction implicit method or partial implicitization (refs. 33 and 34). A shock fitting technique can be applied so that the bow shock is treated as a discontinuity which floats between grid points (ref. 35). This modification will extend the Mach number range and will remove the requirement of a large number of mesh points in the vicinity of the shock. Consequently, a more efficient coordinate stretching routine (ref. 36) can be used to include more points near the body and to compute higher Reynolds number flows.

Experimental Comparisons

Experimental pressure coefficient and convective heat-transfer coefficient distributions were obtained over a circular cylinder normal to a supersonic rarefied airstream in the Mach number range 1.3 to 5.9, the Reynolds number range 19 to 2050, and at two cylinder wall average temperature levels of 90 K and 210 K in the low-density wind-tunnel facility of the University of California at Berkeley by Tewfik and Giedt (ref. 37). Detailed comparison cases were run with the program described herein for a Mach number of 1.90 and a Reynolds number of 105.

Pressure coefficient comparisons for the case of an adiabatic wall are presented in figure 8. Close agreement is obtained between the calculated and experimental results over the forebody of the cylinder through a value of $\pi \geqq \theta > \frac{\pi}{3}$. The calculated pressure coefficients on the base for the range $0 \leqq \theta \leqq \frac{\pi}{3}$ fall slightly below the experimental results but the comparisons are still generally good here. The pressure coefficient over the cylinder for a cold wall case ($T_b \approx 90$ K) follows much the same trend as the adiabatic comparison (fig. 9). The densities near the wall in the wake for this case, and consequently the molecular mean free path, have changed by approximately a factor of 10 from the stagnation region to the base.

A recirculation region is formed in the rear stagnation area of the cylinder. The u component of velocity at the mesh point closest to the body changed sign at $I = 10$ $\left(\theta_b = \frac{9\pi}{50}\right)$. The recirculation region is roughly bounded by two stagnation points along the axis of symmetry in the wake, one at the body ($x = 1$, $y = 0$) and the other approximately one body diameter downstream at $x \approx 2.2$, $y = 0$. A study of the onset of separation from the body in the base region is presented in appendix D.

Convective heat-transfer coefficients are compared in figure 10 for an average wall temperature of 90 K and for a linearly varying wall temperature which more closely approximates the actual experimental temperature variation. These heat-transfer coefficients were evaluated as follows:

$$q_c^* = k^* \frac{\partial T^*}{\partial n^*}$$

$$T^* = \frac{V_\infty^{*2} i}{c_p^*}$$

$$\Delta n^* = -R_N^* h \ \Delta r = - \frac{R_N^* h\beta \ \Delta\eta}{\eta}$$

$$h_c^* = \frac{q_c^*}{T_{aw}^* - T_b^*} = \frac{(-k^*/c_p^*)(\mu^*/\mu^*)(1/R_N^* h\beta) \ \partial i/\partial\eta\big|_b}{(1/c_p^*)(i_{aw} - i_b)} = \frac{-c_p^*\mu^*}{N_{Pr} R_N^* h\beta} \, \frac{1}{i_{aw} - i_b} \, \frac{\partial i}{\partial\eta}\bigg|_b$$

As indicated in the figure, the results are approximately 25 percent greater than experimental results in the forebody. Calculations were performed with twice the number of mesh points in the normal direction, and with a stretching parameter of 0.5 to bring the mesh points even closer to the body. Changes in heat transfer were insignificant with the finer mesh (less than 4 percent of the coarser mesh solution). The results of figure 10 were used to compute convective heat transfer so that the actual heat-transfer errors could be measured. The convective heat-transfer results are presented in figures 11 and 12 where

$$q_{c,exp}^* = h_{c,exp}^*(T_{aw,exp}^* - T_{b,exp}^*)$$

$$q_{c,calc}^* = h_{c,calc}^*(T_{aw,calc}^* - T_{b,calc}^*)$$

However, comparisons in the stagnation region are still in error by approximately 25 percent and remain at about that level over most of the body. For low temperatures ($\approx$100 K) and at 1 atmosphere pressure, the National Bureau of Standards tables (ref. 38) show the Prandtl number at approximately 0.77 for air. The convective heat transfer for a linear temperature variation with $N_{Pr} = 0.77$ was then computed and the results appear in figure 12. Errors in the stagnation region have been reduced to approximately 18 percent but the overall comparison is still poor. The viscosities computed by Sutherland's equation were found to be within 5 percent of the experimental data (ref. 39) at the wall temperature range $80 \text{ K} < T^* < 110 \text{ K}$ and the effects of ε on the enthalpy derivatives were found to be small (see appendix E); therefore, these factors could not account for the errors of 18 percent in the stagnation region. Consequently, it was decided that slip conditions must be important in this Mach number and Reynolds number range.

A condition for temperature slip as a boundary condition was incorporated into the program as follows. The condition for temperature slip (ref. 31), velocity slip being ignored, can be expressed as

$$T_o^* - T_b^* = \frac{2 - \alpha_t}{\alpha_t} \frac{2\gamma}{\gamma + 1} \frac{\bar{\ell}^*}{N_{Pr}} \left.\frac{\partial T^*}{\partial n^*}\right|_o \tag{34}$$

$$\bar{\ell}^* = 1.26\sqrt{\gamma} \frac{\mu_o^*}{\rho_o^* a_o^*} \tag{35}$$

In equation (34), α_t is the thermal accommodation coefficient and T_o is the slip temperature. A value for $\alpha_t = 0.9$ has been found to be representative of values for thermal accommodation coefficients as presented in reference 31. Equation (34) can be simplified by using equation (35), Sutherland's law, and the equation of state to obtain

$$i_o = i_b - \left[\frac{M_\infty}{N_{Re,\infty}} \frac{2 - \alpha_t}{\alpha_t} \frac{2}{\gamma + 1}\sqrt{\gamma(\gamma - 1)}\frac{1.26}{N_{Pr}} \frac{\mu_o}{p_o}\sqrt{i_o}\right]\frac{1}{h\beta} \left.\frac{\partial i}{\partial \eta}\right|_o \tag{36}$$

For zero velocity slip the static enthalpies in equation (36) can be replaced by the total enthalpies. By substituting the finite-difference formulation for $\left.\frac{\partial I}{\partial \eta}\right|_o$ from equation (C4), the slip value of wall enthalpy may be obtained implicitly from

$$I_o^n = \frac{I_b - \frac{1}{h\beta}\left[\frac{M_\infty}{N_{Re,\infty}} \frac{2 - \alpha_t}{\alpha_t} \frac{2}{\gamma + 1}\sqrt{\gamma(\gamma - 1)}\frac{1.26}{N_{Pr}} \frac{\mu_o^{n-1}}{p_o^n}\sqrt{I_o^{n-1}}\right]\left(\frac{I_{NJ-1}^{n-1} - 9I_{NJ}^{n-1}}{3\ \Delta\eta}\right)}{1 + \frac{8}{h\beta 3\ \Delta\eta}\left[\frac{M_\infty}{N_{Re,\infty}} \frac{2 - \alpha_t}{\alpha_t} \frac{2}{\gamma + 1}\sqrt{\gamma(\gamma - 1)}\frac{1.26}{N_{Pr}} \frac{\mu_o^{n-1}}{p_o^n}\sqrt{I_o^{n-1}}\right]} \tag{37}$$

Convective heat transfer was calculated by use of this temperature jump condition and good comparisons were observed with the experimental data in figures 11 and 12. For this Mach number and Reynolds number combination, it is clear that the proper slip boundary conditions are necessary for calculating heat transfer.

Berezkin, et al. (ref. 40) applied holographic interferometry to the supersonic low density gas flow about a spherical body at a Reynolds number of approximately 1750. Shadow and interference images of the density field were obtained in the shock layer of a spherical projectile at Mach 1.93 using a Mach-Zehnder interferometer. Density distributions are presented along two vertical lines corresponding to $x = -1$, $0 < y < y_s$ and $x = 0$, $1 < y < y_s$. Experimental values for shock standoff distance were not presented and all the distributions are nondimensionalized by the distance, $y_s - y_b$. The analytic value of shock standoff distance has been computed from the midpoint of the captured shock. Experimental and analytical results for the density variation are presented in figures 13 and 14. Agreement is good across most of the shock layer. Discrepancies near the wall occur because the wall temperature in the experimental case is not at a steady state. (An adiabatic wall was assumed for the purpose of making these calculations.) By imposing a constant wall temperature corresponding to $i_b = I_b = 0.6I_\infty$, the density agreed well near the wall at $x = 0$ but was too high near the stagnation point at $x = -1$. No further attempts were made to approximate the unsteady nature of the wall temperature.

The characteristics of the solution in the vicinity of a shock are well demonstrated in figures 13 and 14. The locations of the mesh points used to calculate these distributions are marked with crosses. These solutions were obtained with two different damping constants, $\varepsilon = 0.005$ and $\varepsilon = 0.04$. The results for the smaller value of ε (fig. 14) show a sharper shock profile with more of a density undershoot as compared with the $\varepsilon = 0.04$ results. Because of the nature of the coordinate system, the density profile along the line $x = -1$ had to be obtained by linearly interpolating between mesh points in the η-direction. The cross marks which appear on the shock in figure 13 refer to interpolated mesh points and consequently distort the effect of ε in that figure.

An attempt has been made to verify a shock standoff distance calculation by comparing it with the experimental data for supersonic flow over a sphere with $M_\infty = 4.2$, $N_{Re,\infty} = 200$, $T_b^* = T_{stag}^* = 300$ K in nitrogen. An electron beam X-ray technique was used to obtain measurements of the density along the stagnation streamline of a spherical model (ref. 41). This Mach number is on the border of conditions for which the occurrence of a velocity overshoot can cause the calculation of a negative static enthalpy. In this particular case, for a mesh size of 51 × 50 and $\beta = 0.5$, it was determined on the basis of experimental evidence that there were approximately four mesh points across the shock on the stagnation line. Consequently, there were no problems in evaluating static enthalpies ahead of the shock in the stagnation region. However, as the shock started to form around the body, it entered a region where mesh points became separated by larger distances. After approximately 350 iterations, a negative static enthalpy was calculated for this case at a value of $\theta \approx \frac{2\pi}{3}$. A modification was made in the program logic which set the static enthalpy equal to the free-stream static enthalpy whenever a negative value was computed. The density profile across the shock, after 2000 iterations with this modification, is presented in figure 15. Comparisons here show good agreement with experimental data.

Flow Fields Over Planetary Probes

The analytic approximations which correspond to the Viking aeroshell and to a Jupiter probe as shown in figures 2 and 3 and defined in table I were used to compute the flow fields over typical entry bodies at $M_\infty = 2$ and $N_{Re,\infty} = 100$. There are no experimental data currently available for these vehicles at this Mach number and Reynolds number range. The previous comparisons of calculated and experimental density distributions, heat-transfer distributions, and shock predictions indicate that the calculated flow field for the planetary probes should be representative of the actual fields. Flow fields were computed over the Viking aeroshell with a cold wall boundary condition, $I_b = 0.6I_\infty$, and an adiabatic wall boundary condition using $\gamma = 1.285$, $N_{Pr} \square 0.685$, and $T_\infty{}^* = 222$ K. A flow field over the Jupiter probe was computed with an adiabatic wall condition and $\gamma = 1.667$, $N_{Pr} = 0.675$, and $T_\infty{}^* = 277$ K. The grid size for all the cases was 51×50 with $\beta = 1$ and $\varepsilon = 0.04$.

A contour plot of density over the Viking aeroshell is shown in figure 16 for the adiabatic case and in figure 17 for the cold wall case. Contour lines were obtained by using the program CONTOUR (ref. 42). CONTOUR prepares a Cartesian grid system based on interpolated values from the transformed coordinate system. Contour lines are then plotted based on interpolation from the Cartesian grid. Consequently, there is some distortion in the density contours due to the double interpolation and due to differences in the concentrations of mesh points between the Cartesian grid (which gives a uniform concentration of mesh points through the field) and the transformed coordinate system (which concentrates mesh points close to the body). Irregularities in contour lines are caused by these distortions.

The bow shock is shown clearly in both figures with the Mach angle approaching 60° as would be expected for $M_\infty \square 2$. Based on an argument that the nondimensional shock thickness is on the order of the Knudsen number, it appears that the calculated shock thickness is approximately 10 times the actual value. The shock in the stagnation region is smeared over three mesh points which is consistent with results obtained in the experimental comparison section. Because of the computational costs, no attempt was made to improve shock resolution by including more mesh points. The thermal boundary layer for the cold wall case (no temperature slip) is evident in the forebody in figure 17. There are approximately five mesh points through the thermal boundary layer in this case. The Mach number and Reynolds number range for this case closely corresponds to the first comparison case in which good agreement with heat-transfer data was obtained by using the temperature slip condition. So, except for the effect of temperature slip, the thermal boundary layer should be accurately predicted.

Velocity vectors over the Viking aeroshell are presented in figure 18 for the adiabatic case. The recirculation region is clearly visible in the wake. Here again, the effect of velocity slip on the recirculation region is subject to future verification. Pressure coefficients and heat-transfer distributions are presented in figures 19 and 20 for the cold wall case. The method used to integrate pressure coefficients and skin friction to obtain drag coefficients is presented in appendix F. The breakdown of the drag coefficient into the forebody and afterbody pressure drag coefficient and the forebody and afterbody skin-friction drag coefficient is presented in table VI for the adiabatic case.

Similar presentations are made for flow fields obtained, an adiabatic wall being assumed, around a Jupiter probe. Density contours are presented in figure 21. Here again, the calculated shock thickness is probably on the order of 10 times the true value. Velocity vectors are presented in figure 22. A magnification of this vector field with more velocity vectors included shows a distinct velocity gradient near the body from which a boundary-layer growth can be observed (fig. 22). Such a clear, boundary-layer type phenomena will certainly become less obvious with the inclusion of velocity slip. A pressure coefficient distribution is presented in figure 23 and a drag coefficient breakdown is presented in table VI.

When calculating the flow field over the Jupiter probe with stretching parameter $\beta = 0.5$, it was found that there were not enough points to define the wake flow far from the body. The last computational points in the wake before the outflow boundary were still in a region of subsonic flow. The technique of mapping the outflow boundary to infinity when these last computational points were still in a subsonic region initiated large oscillations in the flow variables. The problem was eliminated with $\beta = 1$.

CONCLUDING REMARKS

The coordinate transformation procedure and solution technique described herein has been shown to be well suited for the calculation of the complete flow field surrounding various two-dimensional and axisymmetric bodies. This conclusion is supported by the good comparisons obtained between predicted values and experimental data for pressure coefficient distribution and heat-transfer distribution on a cylinder and for density distributions and shock standoff distance on spheres. The solutions for the flow over the Viking aeroshell and a Jupiter probe were obtained by simply adjusting five transformation constants without having to perform any adjustment on boundary conditions. The versatility of the technique in being able to model many different axisymmetric blunt body shapes and its ability to calculate both the forebody and wake flow over these shapes represent a significant advance in aerothermodynamic technology.

Improvements to the numerical approach can be made to greatly extend the Mach number and Reynolds number range and to reduce the execution time on the computer. The technique can be reprogrammed to run on the STAR 100 computer with a potential execution time reduction of a factor on the order of 30. The numerical approach can also be altered so that the stability limit on Δt is increased by using an alternating direction implicit method or partial implicitization.

An upper limit on Reynolds number on the order of 1000 is imposed because of an inability to resolve a thin boundary layer with a reasonable number of computational mesh points. A lower limit on Reynolds number on the order of 100 is imposed so that continuum theory is applicable. An upper limit on Mach number approximately equal to 4.0 is imposed because of a tendency to calculate negative static enthalpies in the process of capturing the bow shock with a reasonable number of mesh points for large Mach numbers. These limitations are a consequence of the numerical method used and not of the coordinate system itself.

Langley Research Center
National Aeronautics and Space Administration
Hampton, VA 23665
October 26, 1977

APPENDIX A

METRIC COEFFICIENTS

The metric coefficients of an orthogonal curvilinear coordinate system are of the nature of scale factors which give the ratios of differential distances to the differentials of the coordinate parameters (ref. 43). The equations which are used to define the metric coefficients can be derived in the following manner.

Consider the orthogonal transformation as defined in equations (1) for axisymmetric bodies. Let a θ curve be defined in space as a line of constant r and ϕ in equations (1). If $\vec{r}$ is the position vector of a point in space, then a tangent vector to the θ curve is given by

$$\vec{\theta} = \frac{\partial \vec{r}}{\partial \theta} = \frac{\partial \vec{r}}{\partial s_\theta} \frac{\partial s_\theta}{\partial \theta} \tag{A1}$$

where s_θ is arc length along the θ curve. The vector $\partial \vec{r}/\partial s_\theta$ is a unit vector tangent to the θ curve which is redefined as $\vec{u}_\theta$ (fig. 24). Equation (A1) can now be rewritten as

$$\vec{\theta} = h_\theta \vec{u}_\theta \tag{A2}$$

where $h_\theta = \dfrac{ds_\theta}{d\theta}$ is the length of $\vec{\theta}$. Therefore, the relation for h_θ can be written

$$h_\theta = \frac{ds_\theta}{d\theta} = \left| \frac{\partial \vec{r}}{\partial \theta} \right| = \left| \frac{\partial x}{\partial \theta} \vec{i} + \frac{\partial y}{\partial \theta} \vec{j} + \frac{\partial z}{\partial \theta} \vec{k} \right| \tag{A3}$$

The final expression for h_θ, along with h_r and h_ϕ, which can be obtained in a similar manner, becomes

$$\left.\begin{aligned} h_r^2 = \left(\frac{\partial x}{\partial r}\right)^2 + \left(\frac{\partial y}{\partial r}\right)^2 + \left(\frac{\partial z}{\partial r}\right)^2 = \Bigg[&(-B \cosh r + C \sinh r) \cos \theta \\ &- \sum_{n=2}^{N} n A_n e^{nr} \cos n\theta \Bigg]^2 + \Bigg[(B \sinh r - C \cosh r) \sin \theta \\ &+ \sum_{n=2}^{N} n A_n e^{nr} \sin n\theta \Bigg]^2 \end{aligned}\right\} \tag{A4}$$

(Equations continued on next page)

$$\left.\begin{aligned}
h_\theta^2 &= \left(\frac{\partial x}{\partial \theta}\right)^2 + \left(\frac{\partial y}{\partial \theta}\right)^2 + \left(\frac{\partial z}{\partial \theta}\right)^2 = \Bigg[(B \sinh r - C \cosh r) \sin \theta \\
&\quad + \sum_{n=2}^{N} nA_n e^{nr} \sin n\theta\Bigg]^2 + \Bigg[(B \cosh r - C \sinh r) \cos \theta \\
&\quad + \sum_{n=2}^{N} nA_n e^{nr} \cos n\theta\Bigg]^2 \\
h_\phi^2 &= \left(\frac{\partial x}{\partial \phi}\right)^2 + \left(\frac{\partial y}{\partial \phi}\right)^2 + \left(\frac{\partial z}{\partial \phi}\right)^2 = \Bigg[(B \cosh r - C \sinh r) \sin \theta \\
&\quad + \sum_{n=2}^{N} A_n e^{nr} \sin n\theta\Bigg]^2
\end{aligned}\right\} \tag{A4}$$

Note that $h_\theta^2 = h_r^2$ in equations (A4). The metric coefficients are all positive as long as $\vec{u}_\theta$ is in the same direction as $\vec{\theta}$ and $\vec{u}_r$ is in the same direction as $\vec{R}$ in a right-hand coordinate system. Therefore, the metric coefficients may be written as

$$h_\theta = h_r = h \tag{A5}$$

$$h_\phi = |y(\theta,r,0)| = Y \tag{A6}$$

APPENDIX B

MODIFIED BRAILOVSKAYA SCHEME IN TRANSFORMED COORDINATE SYSTEM

The differencing procedure presented in reference (15) was applied to the governing equations in the transformed coordinate system. The subscripts θ and r in this section refer to derivatives with respect to θ and r, respectively. Derivatives with respect to r are approximated by difference formulas in η as defined in equations (18). The difference approximations to the various derivatives and details of the iteration procedure follow:

$$u_\theta(u^n) = \left(u^n_{i+1,j} - u^n_{i-1,j}\right)\Big/D_1$$

$$v_\theta(v^n) = \left(v^n_{i+1,j} - v^n_{i-1,j}\right)\Big/D_1$$

$$I_\theta(I^n) = \left(I^n_{i+1,j} - I^n_{i-1,j}\right)\Big/D_1$$

$$\mu_\theta(I^n,u^n,v^n) = \left(\mu^n_{i+1,j} - \mu^n_{i-1,j}\right)\Big/D_1$$

$$u_r(u^n) = \left(u^n_{i,j+1} - u^n_{i,j-1}\right)\Big/D_2$$

$$v_r(v^n) = \left(v^n_{i,j+1} - v^n_{i,j-1}\right)\Big/D_2$$

$$I_r(I^n) = \left(I^n_{i,j+1} - I^n_{i,j-1}\right)\Big/D_2$$

$$\mu_r(I^n,u^n,v^n) = \left(\mu^n_{i,j+1} - \mu^n_{i,j-1}\right)\Big/D_2$$

$$u_{\theta\theta}\left(u^n,\bar{u}^{n+1}_{i,j}\right) = \left(u^n_{i+1,j} - 2\bar{u}^{n+1}_{i,j} + u^n_{i-1,j}\right)\Big/D_3$$

$$v_{\theta\theta}\left(v^n,\bar{v}^{n+1}_{i,j}\right) = \left(v^n_{i+1,j} - 2\bar{v}^{n+1}_{i,j} + v^n_{i-1,j}\right)\Big/D_3$$

APPENDIX B

$$I_{\theta\theta}\left(I^n, \bar{I}^{n+1}_{i,j}\right) = \left(I^n_{i+1,j} - 2\bar{I}^{n+1}_{i,j} + I^n_{i-1,j}\right)\Big/D_3$$

$$u_{rr}\left(u_n, \bar{u}^{n+1}_{i,j}\right) = \left(u^n_{i,j+1} - 2\bar{u}^{n+1}_{i,j} + u^n_{i,j-1}\right)\Big/D_4 + u_r/\beta$$

$$v_{rr}\left(v_n, \bar{v}^{n+1}_{i,j}\right) = \left(v^n_{i,j+1} - 2\bar{v}^{n+1}_{i,j} + v^n_{i,j-1}\right)\Big/D_4 + v_r/\beta$$

$$I_{rr}\left(I_n, \bar{I}^{n+1}_{i,j}\right) = \left(I^n_{i,j+1} - 2\bar{I}^{n+1}_{i,j} + I^n_{i,j-1}\right)\Big/D_4 + I_r/\beta$$

$$u_{\theta r}(u^n) = \left(u^n_{i+1,j+1} - u^n_{i-1,j+1} - u^n_{i+1,j-1} + u^n_{i-1,j-1}\right)\Big/D_5$$

$$v_{\theta r}(v^n) = \left(v^n_{i+1,j+1} - v^n_{i-1,j+1} - v^n_{i+1,j-1} + v^n_{i-1,j-1}\right)\Big/D_5$$

$$(\rho u)_\theta(\rho^n, u^n) = \left[(\rho u)^n_{i+1,j} - (\rho u)^n_{i-1,j}\right]\Big/D_1$$

$$(\rho uv)_\theta(\rho^n, u^n, v^n) = \left[(\rho uv)^n_{i+1,j} - (\rho uv)^n_{i-1,j}\right]\Big/D_1$$

$$(p + \rho u^2)_\theta(\rho^n, u^n, v^n, I^n) = \left[(p + \rho u^2)^n_{i+1,j} - (p + \rho u^2)^n_{i-1,j}\right]\Big/D_1$$

$$(\rho uI)_\theta(\rho^n, u^n, I^n) = \left[(\rho uI)^n_{i+1,j} - (\rho uI)^n_{i-1,j}\right]\Big/D_1$$

$$(\rho v)_r(\rho^n, v^n) = \left[(\rho v)^n_{i,j+1} - (\rho v)^n_{i,j-1}\right]\Big/D_2$$

$$(\rho uv)_r(\rho^n, u^n, v^n) = \left[(\rho uv)^n_{i,j+1} - (\rho uv)^n_{i,j-1}\right]\Big/D_2$$

$$(p + \rho v^2)_r(\rho^n, u^n, v^n, I^n) = \left[(p + \rho v^2)^n_{i,j+1} - (p + \rho v^2)^n_{i,j-1}\right]\Big/D_2$$

APPENDIX B

$$(\rho vI)_r(\rho^n,v^n,I^n) = \left[(\rho vI)^n_{i,j+1} - (\rho vI)^n_{i,j-1}\right]\Big/D_2$$

$$\begin{array}{ll}
D_1 = 2\ \Delta\theta & \Delta\theta = \pi/(NI - 1) \\
D_2 = \beta 2\ \Delta\eta/\eta & \Delta\eta = 1/NJ \\
D_3 = \Delta\theta^2 & \eta = \dfrac{\Delta\eta}{2} + (j - 1)\ \Delta\eta \\
D_4 = \beta^2\ \Delta\eta^2/\eta^2 & \theta = (i - 1)\ \Delta\theta \\
D_5 = \beta 4\ \Delta\theta\ \Delta\eta/\eta & r = \beta\ \log_e\ (\eta)
\end{array}$$

$$p^n_{i,j} = \frac{\gamma - 1}{\gamma}\,\rho^n_{i,j}\left[I^n_{i,j} - 0.5\left({u^n_{i,j}}^2 + {v^n_{i,j}}^2\right)\right]$$

$$T^n_{i,j} = \left[I^n_{i,j} - 0.5\left({u^n_{i,j}}^2 + {v^n_{i,j}}^2\right)\right](\gamma - 1)M_\infty^2$$

$$\mu^n_{i,j} = \left(T^n_{i,j}\right)^{1.5}(C_2 + 1)\Big/\left(C_2 + T^n_{i,j}\right)$$

The term C_2 is a constant which depends on the gas and the free-stream temperature. These constants can be found in reference 44. For example,

$C_2 = 100/T_\infty^*$ (For air)

$C_2 = 233/T_\infty^*$ (For carbon dioxide)

$C_2 = 98/T_\infty^*$ (For helium)

The metric coefficients and their derivatives are all analytic functions of θ and r which can be obtained from equations (A4). The right-hand side of each conservation equation is now written as

$$A_{i,j}(\rho^n,u^n,v^n) = -\frac{1}{h}\left[(\rho u)_\theta + (\rho v)_r + \rho u\left(\frac{1}{Y}\,Y_\theta + \frac{1}{h}\,h_\theta\right) + \rho v\left(\frac{1}{Y}\,Y_r + \frac{1}{h}\,h_r\right)\right]_{i,j}$$

APPENDIX B

$$
\begin{aligned}
B_{i,j}\left(\rho^n, u^n, v^n, I^n, \bar{u}^{n+1}_{i,j}\right) = \Biggl(& -\frac{1}{h}\biggl[(p + \rho u^2)_\theta + (\rho uv)_r + \rho u^2\left(\frac{1}{Y} Y_\theta + \frac{1}{h} h_\theta\right) \\
& + \rho uv\left(\frac{1}{Y} Y_r + \frac{2}{h} h_r\right) - \rho v^2 \frac{1}{h} h_\theta\biggr] + \frac{1}{h^2 N_{Re,\infty}}\biggl\{\frac{4}{3} \mu u_{\theta\theta} \\
& + \frac{1}{3} \mu v_{\theta r} + \mu u_{rr} + \frac{4}{3}\left(\mu_\theta + \mu \frac{1}{Y} Y_\theta\right) u_\theta + \left(\mu_r + \mu \frac{1}{Y} Y_r\right) u_r \\
& + \left(\frac{1}{3} \mu \frac{1}{Y} Y_r + \frac{7}{3} \mu \frac{1}{h} h_r + \mu_r\right) v_\theta - \left(\frac{7}{3} \mu \frac{1}{h} h_\theta + \frac{2}{3} \mu_\theta\right) v_r \\
& + \biggl[-\frac{2}{3} \mu \frac{1}{h} h_{\theta\theta} - \frac{2}{3} \mu\left(\frac{1}{h} h_\theta\right)^2 - \frac{4}{3} \mu\left(\frac{1}{Y} Y_\theta\right)^2 - \frac{2}{3} \mu \frac{1}{Y} Y_{\theta\theta} \\
& - \mu \frac{1}{h} h_{rr} + \frac{2}{3} \mu \frac{1}{h} h_\theta \frac{1}{Y} Y_\theta - \mu \frac{1}{h} h_r \frac{1}{Y} Y_r - \frac{2}{3} \mu_\theta \frac{1}{Y} Y_\theta \\
& - \frac{2}{3} \mu_\theta \frac{1}{h} h_\theta - \mu_r \frac{1}{h} h_r\biggr] u + \biggl(\frac{1}{3} \mu \frac{1}{h} h_{\theta r} - \frac{2}{3} \mu \frac{1}{Y} Y_{\theta r} \\
& - \frac{4}{3} \mu \frac{1}{Y} Y_\theta \frac{1}{Y} Y_r - \frac{1}{3} \mu \frac{1}{h} h_\theta \frac{1}{Y} Y_r - \frac{2}{3} \mu \frac{1}{h} h_\theta \frac{1}{h} h_r \\
& + 2 \mu \frac{1}{h} h_r \frac{1}{Y} Y_\theta - \frac{2}{3} \mu_\theta \frac{1}{Y} Y_r + \frac{4}{3} \mu_\theta \frac{1}{h} h_r \\
& - \mu_r \frac{1}{h} h_\theta\biggr) v\biggr\}\Biggr)_{i,j}
\end{aligned}
$$

APPENDIX B

$$
\begin{aligned}
C_{i,j}\left(\rho^n, u^n, v^n, I^n, \bar{v}^{n+1}_{i,j}\right) = \Bigg(& -\frac{1}{h}\Bigg[(\rho uv)_\theta + (p + \rho v^2)_r + \rho uv\,\frac{1}{Y}\left(Y_\theta + \frac{2}{h}\,h_\theta\right) \\
& + \rho v^2\left(\frac{1}{Y}\,Y_r + \frac{1}{h}\,h_r\right) - \rho u^2\,\frac{1}{h}\,h_r\Bigg] + \frac{1}{h^2 N_{Re,\infty}}\Bigg\{\frac{4}{3}\,\mu v_{rr} \\
& + \frac{1}{3}\,\mu u_{\theta r} + \mu v_{\theta\theta} - \left(\frac{2}{3}\,\mu_r + \frac{7}{3}\,\mu\,\frac{1}{h}\,h_r\right)u_\theta + \Bigg(\frac{1}{3}\,\mu\,\frac{1}{Y}\,Y_\theta \\
& + \frac{7}{3}\,\mu\,\frac{1}{h}\,h_\theta + \mu_\theta\Bigg)u_r + \left(\mu_\theta + \mu\,\frac{1}{Y}\,Y_\theta\right)v_\theta + \frac{4}{3}\left(\mu\,\frac{1}{Y}\,Y_r + \mu_r\right)v_r \\
& + \Bigg(\frac{1}{3}\,\mu\,\frac{1}{h}\,h_{\theta r} - \frac{2}{3}\,\mu\,\frac{1}{Y}\,Y_{\theta r} - \frac{4}{3}\,\mu\,\frac{1}{Y}\,Y_\theta\,\frac{1}{Y}\,Y_r \\
& - \frac{1}{3}\,\mu\,\frac{1}{Y}\,Y_\theta\,\frac{1}{h}\,h_r - \frac{2}{3}\,\mu\,\frac{1}{h}\,h_\theta\,\frac{1}{h}\,h_r + 2\mu\,\frac{1}{h}\,h_\theta\,\frac{1}{Y}\,Y_r \\
& - \frac{2}{3}\,\mu_r\,\frac{1}{Y}\,Y_\theta + \frac{4}{3}\,\mu_r\,\frac{1}{h}\,h_\theta - \mu_\theta\,\frac{1}{h}\,h_r\Bigg)u + \Bigg[-\frac{2}{3}\,\mu\,\frac{1}{h}\,h_{rr} \\
& - \mu\,\frac{1}{h}\,h_{\theta\theta} - \frac{2}{3}\,\mu\,\frac{1}{Y}\,Y_{rr} - \frac{4}{3}\,\mu\left(\frac{1}{Y}\,Y_r\right)^2 - \frac{2}{3}\,\mu\left(\frac{1}{h}\,h_r\right)^2 \\
& + \frac{2}{3}\,\mu\,\frac{1}{h}\,h_r\,\frac{1}{Y}\,Y_r - \mu\,\frac{1}{h}\,h_\theta\,\frac{1}{Y}\,Y_\theta - \frac{2}{3}\,\mu_r\,\frac{1}{Y}\,Y_r - \frac{2}{3}\,\mu_r\,\frac{1}{h}\,h_r \\
& - \mu_\theta\,\frac{1}{h}\,h_\theta\Bigg]v\Bigg\}\Bigg)_{i,j}
\end{aligned}
$$

APPENDIX B

$$
\begin{aligned}
D_{i,j}(\rho^n,u^n,v^n,I^n,\bar{I}^{n+1}) = \Bigg[& -\frac{1}{h}\bigg[(\rho u I)_\theta + (\rho v I)_r + \rho u I\left(\frac{1}{Y}Y_\theta + \frac{1}{h}h_\theta\right) + \rho v I\bigg(\frac{1}{Y}Y_r \\
& + \frac{1}{h}h_r\bigg)\bigg] + \frac{1}{h^2 N_{Re,\infty}}\Bigg(\mu\bigg\{-\frac{2}{3}u_\theta v_r - \frac{2}{3}\frac{1}{Y}Y_\theta u v_r + v v_{\theta\theta} \\
& - \frac{2}{3}u v_{\theta r} + v_\theta v_\theta + v v_\theta\left(\frac{1}{Y}Y_\theta - \frac{2}{h}h_\theta\right) + u_r v_\theta \\
& + u v_\theta\left(-\frac{2}{3}\frac{1}{Y}Y_r + \frac{1}{3}\frac{1}{h}h_r\right) - v^2\bigg[\frac{1}{h}h_\theta\frac{1}{Y}Y_\theta + \frac{1}{h}h_{\theta\theta} \\
& - \left(\frac{1}{h}h_\theta\right)^2\bigg] + v u_r\frac{1}{Y}Y_\theta + v u_{\theta r} - v u_\theta\left(\frac{2}{3}\frac{1}{Y}Y_r - \frac{1}{3}\frac{1}{h}h_r\right) \\
& + uv\left[-\frac{2}{3}\frac{1}{Y}Y_{\theta r} + \frac{1}{3}\left(\frac{1}{h}h_r\frac{1}{Y}Y_\theta - \frac{1}{h}h_\theta\frac{1}{h}h_r + \frac{1}{h}h_{\theta r}\right)\right] \\
& + \frac{4}{3}\left(u u_{\theta\theta} + u_\theta u_\theta - \frac{1}{h}h_\theta u u_\theta\right) - \frac{2}{3}u^2\bigg[\frac{1}{Y}Y_{\theta\theta} + \frac{1}{h}h_\theta\frac{1}{Y}Y_\theta \\
& + \frac{1}{h}h_{\theta\theta} - \left(\frac{1}{h}h_\theta\right)^2\bigg]\bigg\} + \mu_\theta\bigg[v v_\theta - \frac{2}{3}u v_r - \frac{1}{h}h_\theta v^2 + v u_r \\
& + uv\frac{1}{h}h_r - \frac{2}{3}uv\left(\frac{1}{Y}Y_r + \frac{1}{h}h_r\right) + \frac{4}{3}u u_\theta - \frac{2}{3}u^2\bigg(\frac{1}{Y}Y_\theta \\
& + \frac{1}{h}h_\theta\bigg)\bigg] + \mu\bigg\{\frac{4}{3}\left(v v_{rr} + v_r v_r - \frac{1}{h}h_r v v_r\right) - \frac{2}{3}\bigg(u_\theta v_r \\
& + \frac{1}{Y}Y_\theta u v_r\bigg) + \frac{1}{3}\frac{1}{h}h_\theta\, u v_r + u v_{\theta r} + u_r v_\theta + \frac{1}{Y}Y_r u v_\theta
\end{aligned}
$$

(Equation continued on next page)

$$- \frac{2}{3} v^2 \left[\frac{1}{h} h_r \frac{1}{Y} Y_r + \frac{1}{Y} Y_{rr} + \frac{1}{h} h_{rr} - \left(\frac{1}{h} h_r \right)^2 \right]$$

$$- \frac{1}{3} v u_r \left(\frac{2}{Y} Y_\theta - \frac{1}{h} h_\theta \right) - \frac{2}{3} \left(v u_{\theta r} + \frac{1}{Y} Y_r v u_\theta \right)$$

$$+ \frac{1}{3} uv \left(\frac{1}{h} h_\theta \frac{1}{Y} Y_r - \frac{2}{Y} Y_{\theta r} - \frac{1}{h} h_\theta \frac{1}{h} h_r + \frac{1}{h} h_{\theta r} \right) + u u_{rr}$$

$$+ u_r u_r + u u_r \left(\frac{1}{Y} Y_r - \frac{2}{h} h_r \right) - u^2 \Bigg[\frac{1}{h} h_r \frac{1}{Y} Y_r + \frac{1}{h} h_{rr}$$

$$- \left(\frac{1}{h} h_r \right)^2 \Bigg] \Bigg\} + \mu_r \Bigg\{ \frac{4}{3} v v_r + u v_\theta - \frac{2}{3} \Bigg[v^2 \left(\frac{1}{Y} Y_r + \frac{1}{h} h_r \right)$$

$$+ v u_\theta \Bigg] + \frac{1}{3} uv \left(\frac{1}{h} h_\theta - \frac{2}{Y} Y_\theta \right) + u u_r - u^2 \frac{1}{h} h_r \Bigg\} \Bigg)$$

$$+ \frac{1}{h^2 N_{Re,\infty} N_{Pr}} \Bigg\{ \mu \Bigg[I_\theta \frac{1}{Y} Y_\theta + I_{\theta\theta} - \Bigg(v v_{\theta\theta} + v_\theta v_\theta + v v_\theta \frac{1}{Y} Y_\theta$$

$$+ u u_{\theta\theta} + u_\theta u_\theta + u u_\theta \frac{1}{Y} Y_\theta \Bigg) \Bigg] + \mu_\theta \left[I_\theta - (v v_\theta + u u_\theta) \right]$$

$$+ \mu \Bigg[I_r \frac{1}{Y} Y_r + I_{rr} - \Bigg(v v_{rr} + v_r v_r + v v_r \frac{1}{Y} Y_r + u u_{rr}$$

$$+ u_r u_r + u u_r \frac{1}{Y} Y_r \Bigg) \Bigg] + \mu_r \left[I_r - (v v_r + u u_r) \right] \Bigg\} \Bigg]_{i,j}$$

APPENDIX B

The modified Brailovskaya scheme can now be written as

$$\left.\begin{aligned}
\bar{\rho}^{n+1}_{i,j} &= \rho^{n}_{i,j} + \Delta t\ A_{i,j} && (\rho^{n},u^{n},v^{n})\\
\bar{u}^{n+1}_{i,j} &= u^{n}_{i,j} + \Delta t\ B_{i,j} && \left(\rho^{n},u^{n},v^{n},I^{n},\bar{u}^{n+1}_{i,j}\right)\\
\bar{v}^{n+1}_{i,j} &= v^{n}_{i,j} + \Delta t\ C_{i,j} && \left(\rho^{n},u^{n},v^{n},I^{n},\bar{v}^{n+1}_{i,j}\right)\\
\bar{I}^{n+1}_{i,j} &= I^{n}_{i,j} + \Delta t\ D_{i,j} && \left(\rho^{n},u^{n},v^{n},I^{n},\bar{I}^{n+1}_{i,j}\right)
\end{aligned}\right\}\quad \text{Step 1}$$

$$\left.\begin{aligned}
\rho^{n+1}_{i,j} &= \rho^{n}_{i,j} + \Delta t\ A_{i,j} && (\bar{\rho}^{n+1},\bar{u}^{n+1},\bar{v}^{n+1})\\
u^{n+1}_{i,j} &= u^{n}_{i,j} + \Delta t\ B_{i,j} && (\bar{\rho}^{n+1},\bar{u}^{n+1},\bar{v}^{n+1},\bar{I}^{n+1},u^{n+1})\\
v^{n+1}_{i,j} &= v^{n}_{i,j} + \Delta t\ C_{i,j} && (\bar{\rho}^{n+1},\bar{u}^{n+1},\bar{v}^{n+1},\bar{I}^{n+1},v^{n+1})\\
I^{n+1}_{i,j} &= I^{n}_{i,j} + \Delta t\ D_{i,j} && (\bar{\rho}^{n+1},\bar{u}^{n+1},\bar{v}^{n+1},\bar{I}^{n+1},I^{n+1})
\end{aligned}\right\}\quad \text{Step 2}$$

APPENDIX C

BOUNDARY CONDITIONS AND DIFFERENCE FORMS AT THE BOUNDARIES

Inflow and Outflow Boundary

As discussed in a previous section, the computational boundary at $\eta = 0$ corresponds to a circle of infinite radius surrounding the body. This one boundary has mass entering from the far field and leaving to the far field; hence, it is both an inflow and outflow boundary. Values for properties on the cell walls at this boundary are

$$u_\infty(\theta) = -\sin\theta \qquad \frac{\partial u_\infty}{\partial\theta}(\theta) = -\cos\theta$$

$$v_\infty(\theta) = -\cos\theta \qquad \frac{\partial v_\infty}{\partial\theta}(\theta) = \sin\theta$$

$$\rho_\infty = 1 \qquad p_\infty = \frac{1}{\gamma M_\infty{}^2}$$

$$I_\infty = \frac{1}{(\gamma - 1)M_\infty{}^2} + 0.5$$

$$\frac{\partial u_\infty}{\partial\eta} = \frac{\partial v_\infty}{\partial\eta} = \frac{\partial\rho}{\partial\eta} = \frac{\partial I}{\partial\eta} = \frac{\partial p}{\partial\eta} = 0$$

Values of derivatives with respect to η at mesh points whose cells lie along this boundary ($j = 1$) are calculated as follows:

$$\left.\frac{\partial(\rho v)}{\partial\eta}\right|_{i,1} = \left.\frac{\rho v}{\Delta\eta}\right|_{i,1-\frac{1}{2}}^{i,1+\frac{1}{2}} = \frac{1}{\Delta\eta}\left\{\frac{1}{2}\left[(\rho v)_{i,2} + (\rho v)_{i,1}\right] - \left[-\cos\theta\right]\right\}$$

$$= \frac{1}{2\,\Delta\eta}\left[(\rho v)_{i,2} + (\rho v)_{i,1} + 2\cos\theta\right]$$

In like manner,

$$\left.\frac{\partial(\rho uv)}{\partial\eta}\right|_{i,1} = \frac{1}{2\,\Delta\eta}\left[(\rho uv)_{i,2} + (\rho uv)_{i,1} - 2\cos\theta\sin\theta\right]$$

APPENDIX C

$$\left.\frac{\partial(p + \rho v^2)}{\partial\eta}\right|_{i,1} = \frac{1}{2\,\Delta\eta}\left[(p + \rho v^2)_{i,2} + (p + \rho v^2)_{i,1} - 2(p_\infty + \cos^2\theta)\right]$$

$$\left.\frac{\partial(\rho vI)}{\partial\eta}\right|_{i,1} = \frac{1}{2\,\Delta\eta}\left[(\rho vI)_{i,2} + (\rho vI)_{i,1} + 2\cos\theta\, I_\infty\right]$$

Examples of second derivative formulas are

$$\left.\frac{\partial^2 v}{\partial\eta^2}\right|_{i,1} = \frac{1}{\Delta\eta}\left.\frac{\partial v}{\partial\eta}\right|_{i,1-\frac{1}{2}}^{i,1+\frac{1}{2}} = \frac{1}{\Delta\eta}\left(\frac{v_{i,2} - v_{i,1}}{\Delta\eta} - 0\right) = \frac{1}{\Delta\eta^2}(v_{i,2} - v_{i,1})$$

$$\left.\frac{\partial^2 u}{\partial\eta\,\partial\theta}\right|_{i,1} = \frac{1}{\Delta\eta}\left.\frac{\partial u}{\partial\theta}\right|_{i,1-\frac{1}{2}}^{i,1+\frac{1}{2}} = \frac{1}{\Delta\eta}\left[\frac{1}{\Delta\theta}\, u\Big|_{i-\frac{1}{2},1+\frac{1}{2}}^{i+\frac{1}{2},1+\frac{1}{2}} - (-\cos\theta)\right]$$

$$= \frac{1}{\Delta\eta}\left[\frac{1}{\Delta\theta}\left(\frac{u_{i+1,1+\frac{1}{2}} + u_{i,1+\frac{1}{2}}}{2} - \frac{u_{i,1+\frac{1}{2}} + u_{i-1,1+\frac{1}{2}}}{2}\right) + \cos\theta\right]$$

$$= \frac{1}{\Delta\eta}\left[\frac{1}{2\,\Delta\theta}\left(u_{i+1,1+\frac{1}{2}} - u_{i-1,1+\frac{1}{2}}\right) + \cos\theta\right]$$

$$= \frac{1}{\Delta\eta}\left[\frac{1}{2\,\Delta\theta}\left(\frac{u_{i+1,2} + u_{i+1,1}}{2} - \frac{u_{i-1,2} + u_{i-1,1}}{2}\right) + \cos\theta\right]$$

$$= \frac{1}{\Delta\eta}\left[\frac{1}{4\,\Delta\theta}(u_{i+1,2} + u_{i+1,1} - u_{i-1,2} - u_{i-1,1}) + \cos\theta\right]$$

where $\theta = (i - 1)\Delta\theta$.

APPENDIX C

Wall Boundary Conditions

The computational boundary at $\eta = 1$ describes the entire body in the (x,y) plane. As a consequence of the no-slip condition $u_b = 0$ on the cell walls that are bounded by $\eta = 1$. Since there can be no mass flux through the body, $v_b = 0$ on the cell walls that are bounded by $\eta = 1$. Values for pressure on the wall are extrapolated from interior points. Thus,

$$p_b = 1.5p_{i,NJ} - 0.5p_{i,NJ-1}$$

When the enthalpy or temperature of the wall is specified, the density at the wall can be calculated directly from the equation of state. For the case of an adiabatic wall, the enthalpy at the side of the cell is calculated from interior points at the previous time step using a backward difference formula for $\left.\frac{\partial I}{\partial \eta}\right|_b$, which must equal zero for the adiabatic case. Thus, for an adiabatic wall,

$$I_b{}^n = \frac{9I_{NJ}^{n-1} - I_{NJ-1}^{n-1}}{8} \tag{C1}$$

Mass, momentum, and enthalpy flux across the cell walls opposite to the wall boundary, corresponding to $NJ - \frac{1}{2}$, are calculated differently than those for other interior cell interfaces. It was observed in reference 15 that very low, and, in some cases, negative densities would occur in cells near the wall above the separation point on the base for small mesh sizes and low Reynolds numbers. Allen and Cheng traced this behavior to the way mass, momentum, and energy flux were calculated along the $NJ - \frac{1}{2}$ line of cell edges. They noted that $v_b \equiv 0$ and that as a consequence of the continuity equation and the no-slip condition, $\left.\frac{\partial v}{\partial \eta}\right|_b = 0$ in the steady state. This condition implies that the variation of v as a function of η near the wall should be quadratic. However, by defining the velocity and fluxes through the cell wall at $NJ - \frac{1}{2}$ as the average of values at NJ and NJ - 1, a linear variation of velocity in that area is implied. It would be more accurate to determine the value of velocities and fluxes at $NJ - \frac{1}{2}$ on the basis of a quadratic variation near the wall by putting a second-degree polynomial through the three points at the two cell centers and at the wall. Consequently,

APPENDIX C

$$(\rho v)_{NJ-\frac{1}{2}} = \frac{-(\rho v)_b + (\rho v)_{NJ-1} + 3(\rho v)_{NJ}}{3} = \frac{(\rho v)_{NJ-1} + 3(\rho v)_{NJ}}{3}$$

$$(\rho uv)_{NJ-\frac{1}{2}} = \frac{(\rho uv)_{NJ-1} + 3(\rho uv)_{NJ}}{3}$$

$$(\rho v^2)_{NJ-\frac{1}{2}} = \frac{(\rho v^2)_{NJ-1} + 3(\rho v^2)_{NJ}}{3}$$

$$(\rho vI)_{NJ-\frac{1}{2}} = \frac{(\rho vI)_{NJ-1} + 3(\rho vI)_{NJ}}{3}$$

$$v_{NJ-\frac{1}{2}} = \frac{v_{NJ-1} + 3v_{NJ}}{3}$$

Values for the derivatives of u, v, and I with respect to η at the wall are obtained from a backward difference formula using interior points. Therefore,

$$\left.\frac{\partial u}{\partial \eta}\right|_b = \frac{8u_b - 9u_{NJ} + u_{NJ-1}}{3\ \Delta\eta} \tag{C2}$$

$$\left.\frac{\partial v}{\partial \eta}\right|_b = \frac{8v_b - 9v_{NJ} + v_{NJ-1}}{3\ \Delta\eta} \tag{C3}$$

$$\left.\frac{\partial I}{\partial \eta}\right|_b = \frac{8I_b - 9I_{NJ} - I_{NJ-1}}{3\ \Delta\eta} \tag{C4}$$

Some examples of the difference approximations to derivatives with respect to η in cells positioned next to the wall (at $j = NJ$) are presented:

$$\left.\frac{\partial(\rho v)}{\partial\eta}\right|_{i,NJ} = \frac{1}{\Delta\eta}\,\rho v\Big|_{i,NJ-\frac{1}{2}}^{i,NJ+\frac{1}{2}} = \frac{1}{\Delta\eta}\left[0 - \frac{(\rho v)_{i,NJ-1} + 3(\rho v)_{i,NJ}}{3}\right]$$

$$= -\frac{(\rho v)_{i,NJ-1} + 3(\rho v)_{i,NJ}}{3\,\Delta\eta}$$

$$\left.\frac{\partial(p + \rho v^2)}{\partial\eta}\right|_{i,NJ} = \frac{1}{\Delta\eta}(p + \rho v^2)\Big|_{i,NJ-\frac{1}{2}}^{i,NJ+\frac{1}{2}}$$

$$= \frac{1}{\Delta\eta}\left\{p_{i,b} - \left[\frac{p_{i,NJ-1} + p_{NJ}}{2} + \frac{(\rho v^2)_{i,NJ-1} + 3(\rho v^2)_{i,NJ}}{3}\right]\right\}$$

$$\left.\frac{\partial^2 v}{\partial\eta^2}\right|_{i,NJ} = \frac{1}{\Delta\eta}\,\frac{\partial v}{\partial\eta}\Big|_{i,NJ-\frac{1}{2}}^{i,NJ+\frac{1}{2}}$$

$$= \frac{1}{\Delta\eta}\left(\frac{-9v_{i,NJ} + v_{i,NJ-1}}{3\,\Delta\eta} - \frac{v_{i,NJ} - v_{i,NJ-1}}{\Delta\eta}\right) = \frac{-12v_{i,NJ} + 4v_{i,NJ-1}}{3\,\Delta\eta^2}$$

$$\left.\frac{\partial^2 u}{\partial\eta\,\partial\theta}\right|_{i,NJ} = \frac{1}{\Delta\eta}\,\frac{\partial u}{\partial\theta}\Big|_{i,NJ-\frac{1}{2}}^{i,NJ+\frac{1}{2}} = \frac{1}{\Delta\eta}\left(0 - \frac{1}{\Delta\theta}\,u\Big|_{i-\frac{1}{2},NJ-\frac{1}{2}}^{i+\frac{1}{2},NJ-\frac{1}{2}}\right)$$

(Equation continued on next page)

$$= \frac{1}{\Delta\eta}\left[\frac{1}{\Delta\theta}\left(\frac{u_{i+1,NJ-\frac{1}{2}} + u_{i,NJ-\frac{1}{2}}}{2} - \frac{u_{i,NJ-\frac{1}{2}} + u_{i-1,NJ-\frac{1}{2}}}{2}\right)\right]$$

$$= \frac{1}{\Delta\eta\ \Delta\theta}\left(\frac{u_{i+1,NJ-\frac{1}{2}} - u_{i-1,NJ-\frac{1}{2}}}{2}\right)$$

$$= \frac{1}{2\ \Delta\eta\ \Delta\theta}\left(\frac{u_{i+1,NJ-1} + u_{i+1,NJ}}{2} - \frac{u_{i-1,NJ-1} - u_{i-1,NJ}}{2}\right)$$

$$= \frac{1}{4\ \Delta\eta\ \Delta\theta}(u_{i+1,NJ-1} + u_{i+1,NJ} - u_{i-1,NJ-1} - u_{i-1,NJ})$$

$$\left.\frac{\partial^2 I}{\partial\eta^2}\right|_{i,NJ} = \frac{1}{\Delta\eta}\left.\frac{\partial I}{\partial\eta}\right|_{NJ-\frac{1}{2}}^{NJ+\frac{1}{2}} = \frac{1}{\Delta\eta}\left(\frac{8I_{i,b} - 9I_{i,NJ} + I_{i,NJ-1}}{3\ \Delta\eta} - \frac{I_{i,NJ} - I_{i,NJ-1}}{\Delta\eta}\right)$$

$$= \frac{1}{3\ \Delta\eta^2}\left(8I_{i,b} - 12I_{i,NJ} + 4I_{i,NJ-1}\right)$$

Because of the redefinition of flux terms through the cell walls at $NJ - \frac{1}{2}$, the derivatives with respect to η at cell centers along the line $NJ - 1$ are defined as follows:

$$\left.\frac{\partial(\rho v)}{\partial\eta}\right|_{i,NJ-1} = \frac{1}{\Delta\eta}\ \rho v\Big|_{i,NJ-\frac{3}{2}}^{i,NJ-\frac{1}{2}}$$

(Equation continued on next page)

$$= \frac{1}{\Delta\eta}\left[\frac{(\rho v)_{i,NJ-1} + 3(\rho v)_{i,NJ}}{3} - \frac{(\rho v)_{i,NJ-1} + (\rho v)_{i,NJ-2}}{2}\right]$$

$$= \frac{1}{6\ \Delta\eta}\left[6(\rho v)_{i,NJ} - (\rho v)_{i,NJ-1} - 3(\rho v)_{i,NJ-2}\right]$$

$$\left.\frac{\partial(p + \rho v^2)}{\partial\eta}\right|_{i,NJ-1} = \frac{1}{\Delta\eta}(p + \rho v^2)\Bigg|_{i,NJ-\frac{3}{2}}^{i,NJ-\frac{1}{2}}$$

$$= \frac{1}{\Delta\eta}\left\{\frac{p_{i,NJ} + p_{i,NJ-1}}{2} + \frac{1}{3}\left[(\rho v^2)_{i,NJ-1} + 3(\rho v^2)_{i,NJ}\right]\right.$$

$$\left. - \frac{p_{i,NJ-1} + p_{i,NJ-2}}{2} - \frac{(\rho v^2)_{i,NJ-1} + (\rho v^2)_{i,NJ-2}}{2}\right\}$$

$$= \frac{1}{\Delta\eta}\left\{\frac{1}{2}(p_{i,NJ} - p_{i,NJ-2}) + \frac{1}{6}\left[6(\rho v^2)_{i,NJ}\right.\right.$$

$$\left.\left. - (\rho v^2)_{i,NJ-1} - 3(\rho v^2)_{i,NJ-2}\right]\right\}$$

Other η derivatives are defined similarly at $J = NJ - 1$.

APPENDIX D

OBSERVATIONS OF SEPARATION IN WAKE

The presence of an inflection point in the pressure distribution curves can usually be used to determine the location of the boundary-layer separation from a cylinder surface (ref. 45). Values for $\frac{\partial^2 p}{\partial \theta^2} = \left(\frac{p_{i+1} - 2p_i + p_{i-1}}{\Delta\theta^2}\right)_b$ were calculated in the vicinity of the separation point of spheres, cylinders, and the planetary probe shapes presented herein with cold wall and adiabatic wall specifications. In all cases it was found that separation occurred within $\pm\Delta\theta$ of the location where $\partial^2 p/\partial\theta^2$ changed sign. It should be noted that this derivative is not equivalent to $\partial^2 p/\partial s^2$ where s is the arc length. Since $ds \equiv h\, d\theta$, it can be shown that

$$\frac{\partial^2 p}{\partial s^2} = \frac{1}{h^2}\left(\frac{\partial^2 p}{\partial \theta^2} - \frac{1}{h}\frac{\partial h}{\partial \theta}\frac{\partial p}{\partial \theta}\right)$$

where $\frac{\partial h}{\partial \theta} = 0$ for a sphere or cylinder but is nonzero for any other body shape.

APPENDIX E

EFFECT OF ε ON ENTHALPY DERIVATIVE

Because the convective heat transfer is so sensitive to the enthalpy derivative at the wall, it was decided to examine the effect of ε on this derivative. Three flow field solutions were obtained for the first experimental comparison case ($M_\infty = 1.90$, $N_{Re,\infty} = 105$, $N_{Pr} = 0.7$, $\gamma = 1.4$, $T_b^* = 90$ K). The first solution was obtained with $\varepsilon = 0.04$, $\beta = 1$, and a mesh size of 51 × 50; the second solution, with $\varepsilon = 0.001$, $\beta = 1$, and a mesh size of 51 × 50; and the third solution, with $\varepsilon = 0.001$, $\beta = 0.5$, and a mesh size of 51 × 100. Results of this investigation are presented in table V. It can be seen that there is only an average of 2-percent difference between the $\varepsilon = 0.04$ solution and the $\varepsilon = 0.001$ solution for the mesh size of 51 × 50. Most of this error is due to differences in the derivatives on the rear stagnation line. However, the magnitude of these differences is small in the base and will not appreciably change heat-transfer levels there. The finer mesh size causes an average of 4-percent increase in the enthalpy derivatives. These derivatives are thus seen to be more sensitive to mesh size near the wall than to the smoothing parameter.

APPENDIX F

DRAG COEFFICIENTS

The drag coefficient around an axisymmetric body in the transformed coordinate system can be expressed as

$$C_D = \frac{1}{\frac{1}{2}\rho_\infty{}^* V_\infty{}^{*2} S^*}\left(\int_0^\pi \left[p_b{}^*(\theta) - p_\infty{}^*\right]\left\{-\sin\left[\psi_b(\theta)\right]\right\} dA^*\right.$$

$$\left. + \int_0^\pi \tau_b{}^*(\theta)\left\{-\cos\left[\psi_b(\theta)\right]\right\} dA^*\right) \tag{F1}$$

where the angle ψ is defined in figure 6 and $\sin\psi$ and $\cos\psi$ are defined in equations (30). Also,

$$dA^* = 2\pi R_N{}^* Y R_N{}^* h\ d\theta = 2\pi R_N{}^{*2} Y h\ d\theta \tag{F2}$$

$$S^* = \pi R_N{}^{*2} Y_{max}^2 \tag{F3}$$

$$\tau^* = -\mu^* \left.\frac{\partial u^*}{\partial n^*}\right|_b = \left.\frac{\mu^*}{R_N{}^* h\beta}\ \frac{\partial u^*}{\partial \eta}\right|_b \tag{F4}$$

Note that $dn^* = -R_N{}^* \frac{h\beta}{\eta}\ d\eta$.

Combining equations (F1) to (F4) yields

$$C_D = \frac{1}{Y_{max}^2}\left\{\int_0^\pi -4\left[p(\theta) - p_\infty\right] \sin\left[\psi(\theta)\right] hY\ d\theta\right.$$

$$\left. + \int_0^\pi \frac{-4}{N_{Re,\infty}}\ \frac{\mu}{\beta}\ \frac{1}{h}\ \frac{\partial u}{\partial \eta} \cos\left[\psi(\theta)\right] hY\ d\theta\right\}_b$$

By substituting the values of h and Y from equations (A4) to (A6) and the value of $\sin\psi$ and $\cos\psi$ from equations (30) and noting that $r = 0$ for the body, one obtains

APPENDIX F

$$
\begin{aligned}
C_D = \frac{1}{Y^2_{\text{max}}} \Bigg[& \int_0^\pi -4\left[p(\theta) - p_\infty\right] \left(B \cos \theta + \sum_{n=2}^{N} nA_n \cos n\theta \right) \Bigg(B \sin \theta \\
& + \sum_{n=2}^{N} A_n \sin n\theta \Bigg) d\theta \\
& + \int_0^\pi \frac{-4}{N_{Re,\infty}} \frac{\mu}{\beta} \frac{\partial u}{\partial \eta} \frac{\left(-C \sin \theta + \sum_{n=2}^{N} nA_n \sin n\theta \right) \left(B \sin \theta + \sum_{n=2}^{N} A_n \sin n\theta \; d\theta \right)}{h(\theta,0)} \Bigg]_b
\end{aligned}
$$

REFERENCES

1. Barnwell, Richard W.: A Time-Dependent Method for Calculating Supersonic Angle-of-Attack Flow About Axisymmetric Blunt Bodies With Sharp Shoulders and Smooth Nonaxisymmetric Blunt Bodies. NASA TN D-6283, 1971.

2. South, Jerry C., Jr.: Calculation of Axisymmetric Supersonic Flow Past Blunt Bodies With Sonic Corners, Including a Program Description and Listing. NASA TN D-4563, 1968.

3. Zoby, Ernest V.; and Graves, Randolph A., Jr.: A Computer Program for Calculating the Perfect Gas Inviscid Flow Field About Blunt Axisymmetric Bodies at an Angle of Attack of 0°. NASA TM X-2843, 1973.

4. Chaussee, D. S.; Holtz, T.; and Kutler, P.: Inviscid Supersonic/Hypersonic Body Flowfields and Aerodynamics From Shock-Capturing Technique Calculations. AIAA Paper No. 75-837, June 1975.

5. Moss, James N.: Reacting Viscous-Shock-Layer Solutions With Multicomponent Diffusion and Mass Injection. NASA TR R-411, 1974.

6. Li, C. P.: Numerical Solution of Viscous Reacting Blunt Body Flows of a Multicomponent Mixture. AIAA Paper No. 73-202, Jan. 1973.

7. Sutton, Kenneth: Characteristics of Coupled Nongray Radiating Gas Flows With Ablation Product Effects About Blunt Bodies During Planetary Entries. Ph. D. Thesis, North Carolina State Univ. at Raleigh, 1973. (Available as NASA TM X-72078.)

8. Moretti, Gino; and Salas, Manuel D.: The Blunt Body Problem for a Viscous Rarefied Gas Flow. AIAA Paper No. 69-139, Jan. 1969.

9. Lykoudis, Paul S.: A Review of Hypersonic Wake Studies. AIAA J., vol. 4, no. 4, Apr. 1966, pp. 577-590.

10. Chapman, Dean R.; Kuehn, Donald M.; and Larson, Howard K.: Investigation of Separated Flows in Supersonic and Subsonic Streams With Emphasis on the Effect of Transition. NACA Rep. 1356, 1958. (Supersedes NACA TN 3869.)

11. Crocco, Luigi; and Lees, Lester: A Mixing Theory for the Interaction Between Dissipative Flows and Nearly Isentropic Streams. J. Aeronaut. Sci., vol. 19, no. 10, Oct. 1952, pp. 649-676.

12. Reeves, Barry L.: and Lees, Lester: Theory of Laminar Near Wake of Blunt Bodies in Hypersonic Flow. AIAA J., vol. 3, no. 11, Nov. 1965, pp. 2061-2074.

13. Grange, Jean-Marie; Klineberg, John M.; and Lees, Lester: Laminar Boundary-Layer Separation and Near-Wake Flow for a Smooth Blunt Body at Supersonic and Hypersonic Speeds. AIAA J., vol. 5, no. 6, June 1967, pp. 1089-1096.

14. Weiss, R. F.: A New Theoretical Solution of the Laminar, Hypersonic Near Wake. AIAA J., vol. 5, no. 12, Dec. 1967, pp. 2142-2149.

15. Allen, John S., Jr.: Numerical Solutions of the Compressible Navier-Stokes Equations for the Laminar Near Wake in Supersonic Flow. Ph. D. Diss., Princeton Univ., June 1968.

16. Scala, Sinclaire M.; and Gordon, Paul: Solution of the Time-Dependent Navier-Stokes Equations for the Flow Around a Circular Cylinder. AIAA J., vol. 6, no. 5, May 1968, pp. 815-822.

17. Kitchens, Clarence W., Jr.: Numerical Experiments With the Compressible Navier-Stokes Equations. Proceedings of the Third International Conference on Numerical Methods in Fluid Mechanics, Volume I. Volume 18 of Lecture Notes in Physics, Henri Cabannes and Roger Teman, eds., Springer-Verlag, 1973, pp. 120-129.

18. Peyret, Roger; and Viviand, Henri: Calculation of the Flow of a Viscous Compressible Fluid Around an Obstacle of Parabolic Shape. NASA TT F-16558, 1975.

19. Gnoffo, Peter A.: A Generalized Orthogonal Coordinate System for Describing Families of Axisymmetric and Two-Dimensional Bodies. NASA TM X-3468, 1977.

20. Bradley, Fred E.; Cowan, Wesley D.; and Vojvodich, Nick S.: 1980 Pioneer Jupiter Orbiter Probe Mission, Part II: Atmospheric Entry Probe Design Considerations. AIAA Paper No. 75-1162, Sept. 1975.

21. Vincenti, Walter G.; and Kruger, Charles H., Jr.: Introduction to Physical Gas Dynamics. John Wiley & Sons, Inc., c.1965.

22. Hughes, William F.; and Gaylord, Eber W.: Basic Equations of Engineering Science. Schaum's Outline Series, McGraw-Hill Book Co., Inc., c.1964.

23. Back, L. H.: Conservation Equations of a Viscous, Heat-Conducting Fluid in Curvilinear Orthogonal Coordinates. Tech. Rep. 32-1332 (Contract No. NAS 7-100), Jet Propul. Lab., California Inst. Technol., Sept. 15, 1968.

24. Crocco, Luigi: A Suggestion for the Numerical Solution of the Steady Navier-Stokes Equations. AIAA J., vol. 3, no. 10, Oct. 1965, pp. 1824-1832.

25. Roache, Patrick J.: Computational Fluid Dynamics. Hermosa Publ., c.1972.

26. Allen, J. S.; and Cheng, S. I.: Numerical Solutions of the Compressible Navier-Stokes Equations for the Laminar Near Wake. Phys. Fluids, vol. 13, no. 1, Jan. 1970, pp. 37-52.

27. Carter, James Edward: Numerical Solutions of the Supersonic, Laminar Flow Over a Two-Dimensional Compression Corner. Ph. D. Thesis, Virginia Polytechnic Institute and State University, Aug. 1971.

28. Morduchow, Morris; and Libby, Paul A.: On a Complete Solution of the One-Dimensional Flow Equations of a Viscous, Heat-Conducting Gas. J. Aeronaut. Sci., vol. 16, no. 11, Nov. 1949, pp. 674-684.

29. Probstein, Ronald F.: Aerodynamics of Rarefied Gases. WADC TN 58-228, U.S. Air Force, July 1958. (Available from DDC as AD 155 819.)

30. Hayes, Wallace D.; and Probstein, Ronald F.: Hypersonic Flow Theory. Academic Press, Inc., 1959.

31. Schaaf, S. A.; and Chambré, P. L.: Flow of Rarefied Gases. Fundamentals of Gas Dynamics, Howard W. Emmons, ed., Princeton Univ. Press, 1958, pp. 687-738.

32. Weilmuenster, K. James; and Howser, Lona M.: Solution of a Large Hydrodynamic Problem Using the STAR 100 Computer. NASA TM X-73904, 1976.

33. Lambiotte, Jules J., Jr.; and Howser, Lona M.: Vectorization on the STAR Computer of Several Numerical Methods for a Fluid Flow Problem. NASA TN D-7545, 1974.

34. Graves, Randolph A., Jr.: Partial Implicitization. J. Comput. Phys., vol. 13, no. 3, Nov. 1973, pp. 439-444.

35. Moretti, Gino: Three-Dimensional, Supersonic, Steady Flows With Any Number of Imbedded Shocks. AIAA Paper No. 74-10, Jan.-Feb. 1974.

36. Blottner, F. G.: Variable Grid Scheme Applied to Turbulent Boundary Layers. Comput. Methods in Appl. Mech. & Eng., vol. 4, no. 2, Sept. 1974, pp. 179-194.

37. Tewfik, O. K.; and Giedt, W. H.: Heat Transfer, Recovery Factor and Pressure Distributions Around a Cylinder Normal to a Supersonic Rarefied Air Stream. Part I. Experimental Data. Rep. HE-150-162, Inst. Eng. Res., Univ. of California, Jan. 30, 1959.

38. Hilsenrath, Joseph; Beckett, Charles W.; Benedict, William S.; Fano, Lilla; Hoge, Harold J.; Masi, Joseph F.; Nuttall, Ralph L.; Touloukian, Yeram S.; and Woolley, Harold W.: Tables of Thermal Properties of Gases. NBS Circ. 564, U.S. Dep. Com., Nov. 1, 1955.

39. Bertram, Mitchel H.: Comment on "Viscosity of Air." J. Spacecraft Rockets, vol. 4, no. 2, Feb. 1967, p. 287.

40. Berezkin, A. N.; Mudrevskaia, N. P.; Mustafina, L. T.; and Razumovskaia, A. I.: The Use of Holographic Wave Front Reconstruction To Obtain Shadow and Interference Images of a Low Density Gas Flow. Zhurnal Tekhnicheskoi Fiziki, vol. 46, Aug. 1976, pp. 1724-1727.

41. Russell, David A.: Density Disturbance Ahead of a Sphere in Rarefied Supersonic Flow. Phys. Fluids, vol. 11, no. 8, Aug. 1968, pp. 1679-1685.

42. Hamm, Roy W.; Kibler, James F.; and Morris, W. Douglas: A Program for Contouring Randomly Spaced Data. NASA TM X-72749, 1975.

43. Hildebrand, Francis B.: Advanced Calculus for Applications. Prentice-Hall, Inc., 1962.

44. Hall, Newman A.: Thermodynamics of Fluid Flow. Prentice-Hall, Inc., c.1951.

45. Tewfik, O. K.; and Giedt, W. H.: Heat Transfer, Recovery Factor, and Pressure Distributions Around a Circular Cylinder Normal to a Supersonic Rarefied-Air Stream. J. Aerosp. Sci., vol. 27, no. 10, Oct. 1960, pp. 721-729.

TABLE I.- PARAMETERS DEFINING PROBE SHAPES

Parameter	Viking aeroshell	Jupiter probe
R_N	1	1
R_B	2.5	3.227272727
L	1.5454545	3.227272727
L_1	.588940466	1.378281288
Y_{max}	1.590909091	2.163636364
B	1.514647678	2.078979297
C	.716078733	1.548980197
A_2	-.059786238	-.042862760
A_3	-.056648540	-.064656167
A_4	.042817883	.062550354

TABLE II.- VISCOUS STABILITY LIMIT CALCULATIONS ON VIKING AEROSHELL

$\left[\Delta t_{inviscid} = 0.01100; \quad \eta = 1\right]$

Index i	Δt_{viscid}	$\dfrac{\Delta t_{inviscid}}{\Delta t_{viscid}}$
1	5.575×10^{-3}	1.973
2	5.530	1.989
23	.604	18.212
24	.494	22.267
25	.462	23.809
26	.506	21.739
29	1.205	9.129
51	35.703	.308

TABLE III.- VARIATION OF ENTHALPY DERIVATIVE WITH INCREASING ITERATIONS

$\left[(51 \times 100), \quad \varepsilon = 0.001\right]$

Index i	θ, deg	$\partial i/\partial \eta$, 6000 iterations, $e = 8.45 \times 10^{-5}$	$\partial i/\partial \eta$, 5000 iterations, $e = 1.61 \times 10^{-4}$	$\partial i/\partial \eta$, 4000 iterations, $e = 3.24 \times 10^{-4}$	$\partial i/\partial \eta$, 3000 iterations, $e = 6.19 \times 10^{-4}$	$\partial i/\partial \eta$, 2000 iterations, $e = 1.40 \times 10^{-3}$	$\partial i/\partial \eta$, 1000 iterations, $e = 4.42 \times 10^{-3}$
1	0	-0.653	-0.660	-0.660	-0.707	-0.900	-1.540
6	18	-.580	-.587	-.587	-.580	-.707	-1.307
11	36	-.773	-.773	-.780	-.787	-.747	-.813
16	54	-1.160	-1.160	-1.167	-1.173	-1.133	-.760
21	72	-2.027	-2.033	-2.033	-1.987	-1.953	-1.467
26	90	-3.533	-3.533	-3.480	-3.493	-3.407	-2.780
31	108	-5.640	-5.640	-5.647	-5.600	-5.513	-4.853
36	126	-8.293	-8.293	-8.300	-8.307	-8.207	-7.547
41	144	-10.993	-10.993	-10.993	-10.987	-11.000	-10.367
46	162	-12.987	-12.980	-13.033	-13.080	-13.073	-12.527
51	180	-13.687	-13.747	-13.733	-13.780	-13.827	-13.273

TABLE IV.- EFFECTS OF β ON DISTANCE d OF MESH POINT FROM ORIGIN OF SPHERE OF RADIUS EQUAL TO ONE

j	β = 1.00 d	β = 0.75 d	β = 0.50 d	β = 0.25 d
1	100.000000000	31.622776602	10.000000000	3.162277660
2	33.333333333	13.872638168	5.773502692	2.402811414
3	20.000000000	9.457416090	4.472135955	2.114742527
4	14.285714286	7.348123891	3.779644730	1.944130842
5	11.111111111	6.085806195	3.333333333	1.825741858
6	9.090909091	5.235467719	3.015113446	1.736408203
7	7.692307692	4.618941755	2.773500981	1.665383133
8	6.666666667	4.148886515	2.581988897	1.606856838
9	5.882352941	3.777141971	2.425356250	1.557355531
10	5.263157895	3.474839897	2.294157339	1.514647596
11	4.761904762	3.223558299	2.182178902	1.477219991
12	4.347826087	3.010954016	2.085144141	1.444002819
13	4.000000000	2.828427125	2.000000000	1.414213562
14	3.703703704	2.669790460	1.924500897	1.387263817
15	3.448275862	2.530471799	1.856953382	1.362700768
16	3.225806452	2.407014628	1.796053020	1.340169027
17	3.030303030	2.296754337	1.740776560	1.319384917
18	2.857142857	2.197601621	1.690308509	1.300118652
19	2.702702703	2.107893705	1.643989873	1.282181685
20	2.564102564	2.026289737	1.601281538	1.265417535
21	2.439024390	1.951695710	1.561737619	1.249695010
22	2.325581395	1.883209595	1.524985703	1.234903115
23	2.222222222	1.820080575	1.490711985	1.220947167
24	2.127659574	1.761678307	1.458649915	1.207745799
25	2.040816327	1.707469442	1.428571429	1.195228609
26	1.960784314	1.656999464	1.400280084	1.183334308
27	1.886792453	1.609878490	1.373605639	1.172009232
28	1.818181818	1.565770054	1.348399725	1.161206151
29	1.754385965	1.524382162	1.324532357	1.150883294
30	1.694915254	1.485460101	1.301889110	1.141003554
31	1.639344262	1.448780606	1.280368799	1.131533826
32	1.587301587	1.414147102	1.259881577	1.122444465
33	1.538461538	1.381385785	1.240347346	1.113708825
34	1.492537313	1.350342380	1.221694444	1.105302874
35	1.449275362	1.320879445	1.203858531	1.097204872
36	1.408450704	1.292874109	1.186781658	1.089395088
37	1.369863014	1.266216169	1.170411472	1.081855569
38	1.333333333	1.240806479	1.154700538	1.074569932
39	1.298701299	1.216555583	1.139605765	1.067523192
40	1.265822785	1.193382546	1.125087901	1.060701608
41	1.234567901	1.171213948	1.111111111	1.054092553
42	1.204819277	1.149983028	1.097642600	1.047684399
43	1.176470588	1.129628929	1.084652289	1.041466413
44	1.149425287	1.110096058	1.072112535	1.035428672
45	1.123595506	1.091333521	1.059997880	1.029561985
46	1.098901099	1.073294628	1.048284837	1.023857821
47	1.075268817	1.055936467	1.036951695	1.018308251
48	1.052631579	1.039219521	1.025978352	1.012905895
49	1.030927835	1.023107337	1.015346165	1.007643868
50	1.010101010	1.007566232	1.005037815	1.002515743

TABLE V.- EFFECT OF β AND MESH SIZE ON ENTHALPY DERIVATIVE

Index i	① ε = 0.04 (51 × 50) $\left.\frac{\partial i}{\partial \eta}\right\|_b$	② ε = 0.001 (51 × 50) $\left.\frac{\partial i}{\partial \eta}\right\|_b$	③ ε = 0.001 (51 × 100) $\left.\frac{\partial i}{\partial \eta}\right\|_b$	Percent differences		
				(① - ③)/③ 100	(② - ③)/③ 100	(① - ②)/② 100
1	-0.598	-0.688	-0.653	-8.42	5.36	-13.08
6	-.544	-.566	-.580	-6.21	-2.41	-3.89
11	-.774	-.783	-.773	.13	1.29	-1.15
16	-1.139	-1.134	-1.160	-1.81	-2.24	.44
21	-1.954	-1.936	-2.027	-3.60	-4.49	.93
26	-3.324	-3.283	-3.533	-5.92	-7.08	1.25
31	-5.301	-5.259	-5.640	-6.01	-6.76	.80
36	-7.809	-7.799	-8.293	-5.84	-5.96	.13
41	-10.434	-10.444	-10.993	-5.09	-4.99	-.10
46	-12.453	-12.499	-12.987	-4.11	-3.76	-.37
51	-13.213	-13.216	-13.687	-3.46	-3.44	-.02
Average, percent				4.60	4.34	2.015

TABLE VI.- DRAG COEFFICIENTS

	Pressure drag coefficient		Skin-friction drag coefficient		Total pressure drag coefficient	Total skin-friction drag coefficient	C_D (No slip)
	Forward	Aft	Forward	Aft			
Jupiter probe	1.051	0.1975	0.1685	0.06267	1.243	0.2285	1.477
Viking adiabatic wall	1.296	0.2610	0.1121	0.03650	1.557	0.1486	1.705

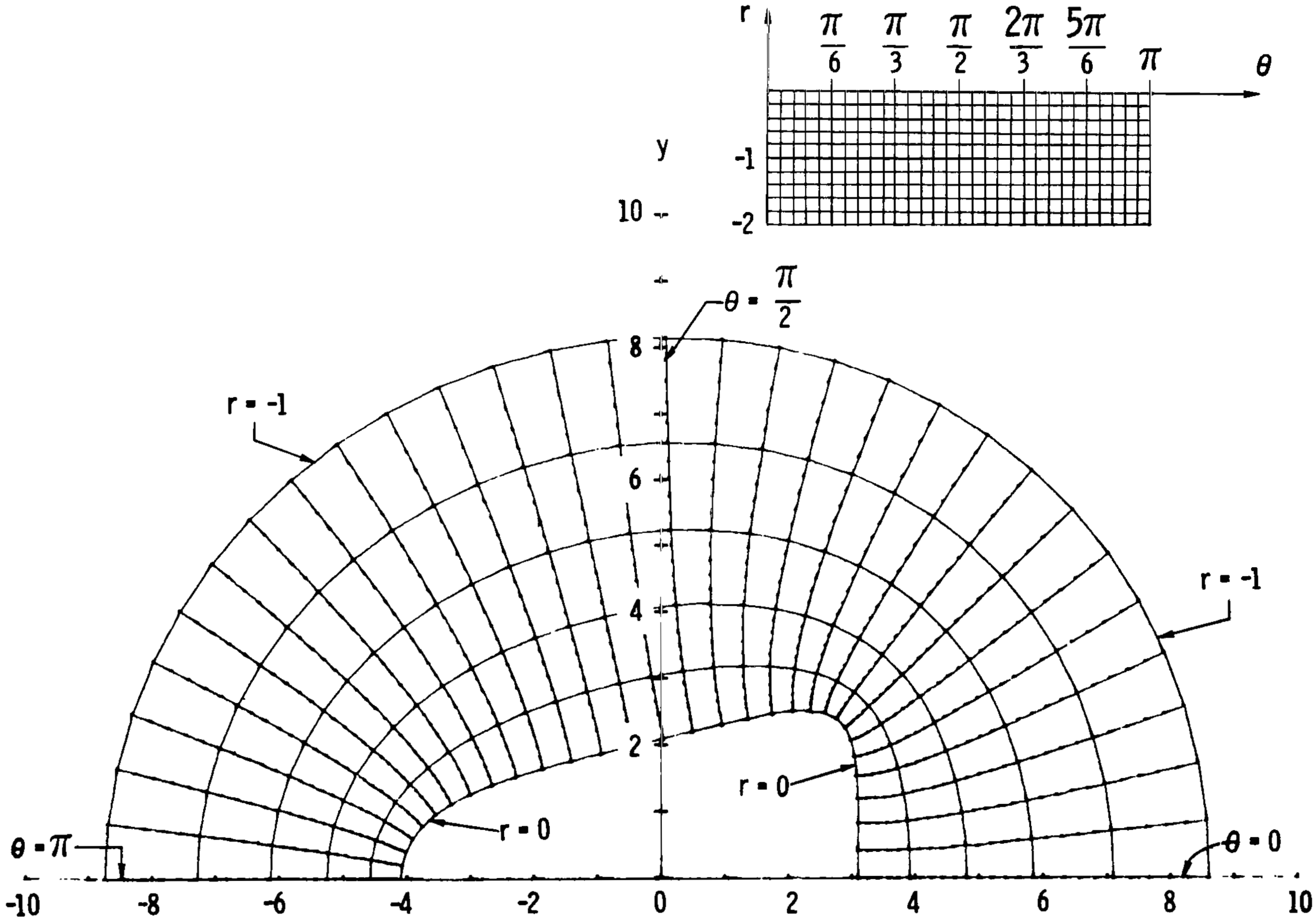

Figure 1.- Generalized natural coordinate system.

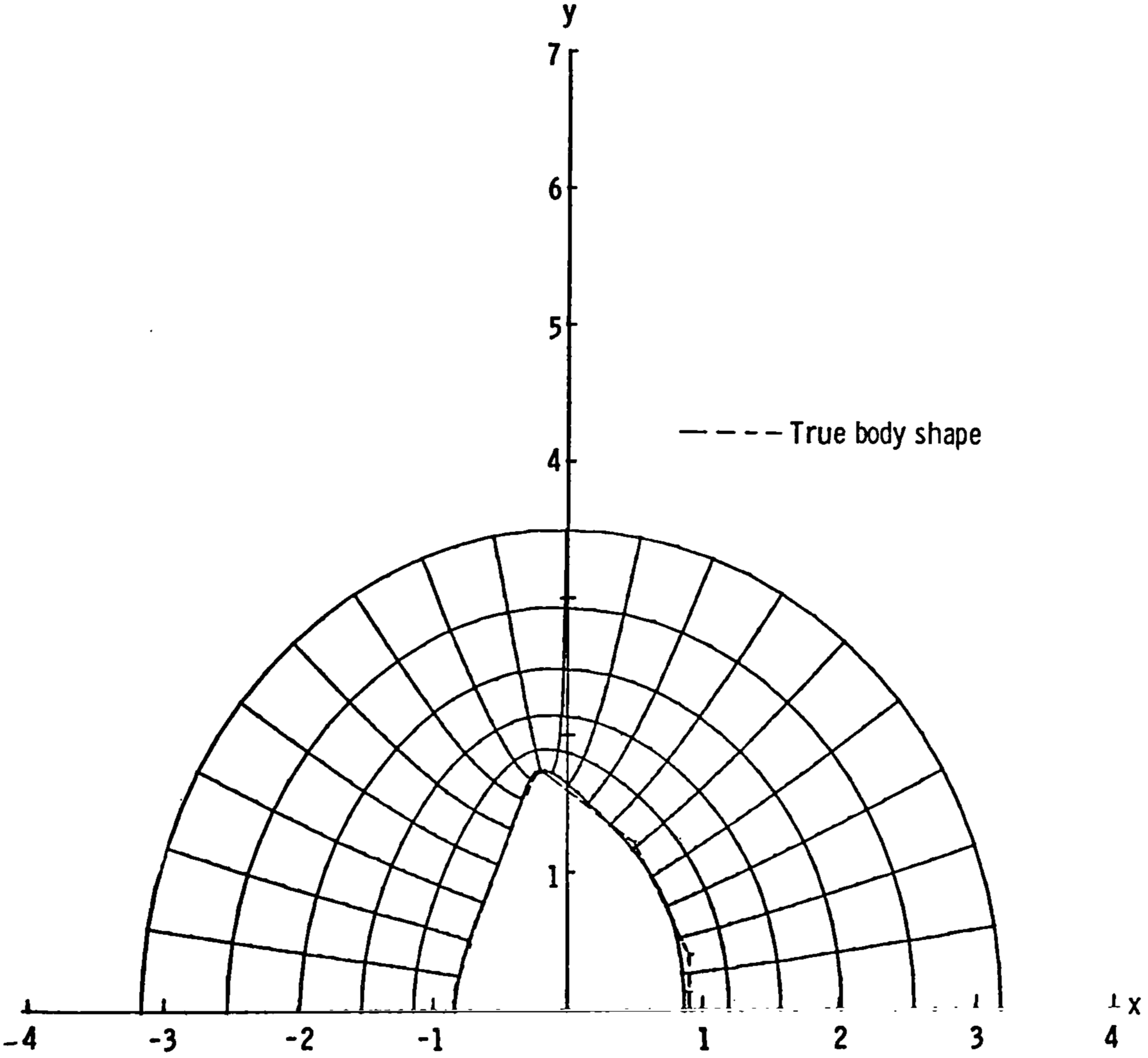

Figure 2.- Analytic approximation to Viking aeroshell with associated coordinate lines.

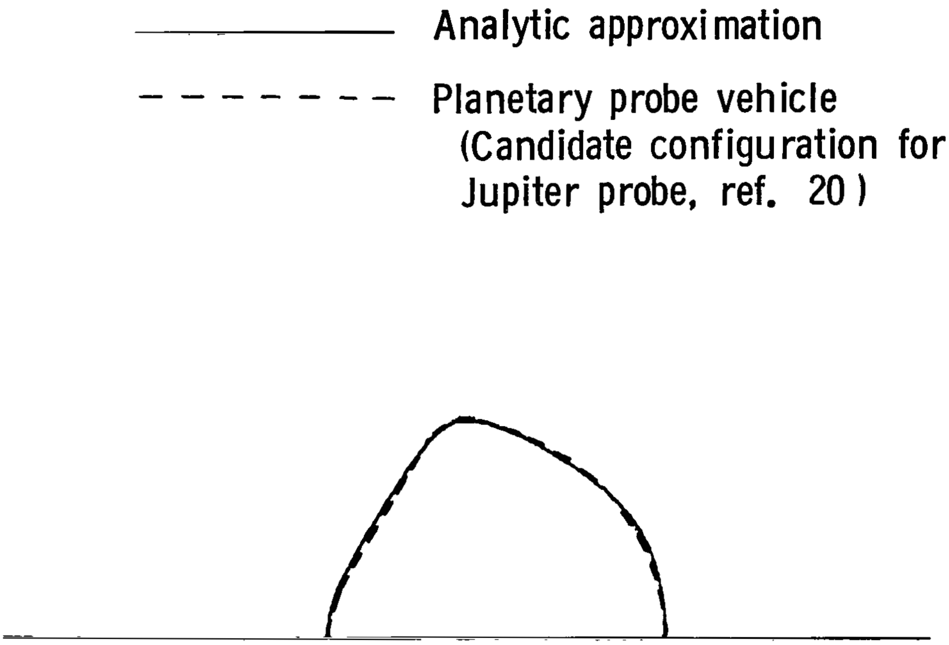

Figure 3.- Analytic approximation to Jupiter probe.

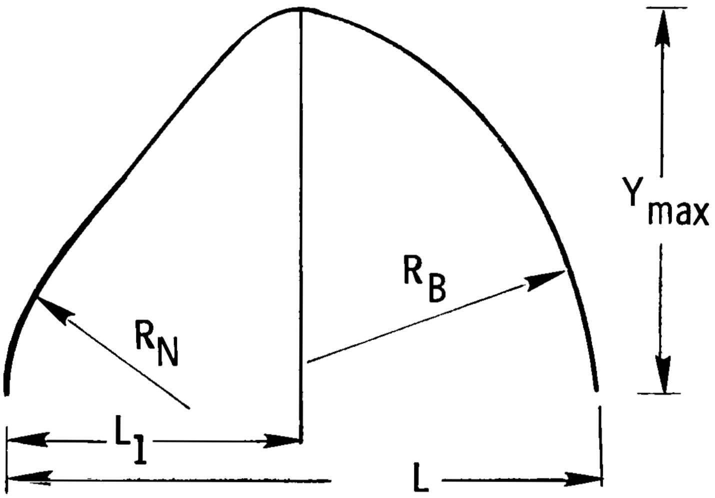

Figure 4.- Basic geometric parameters of planetary probe.

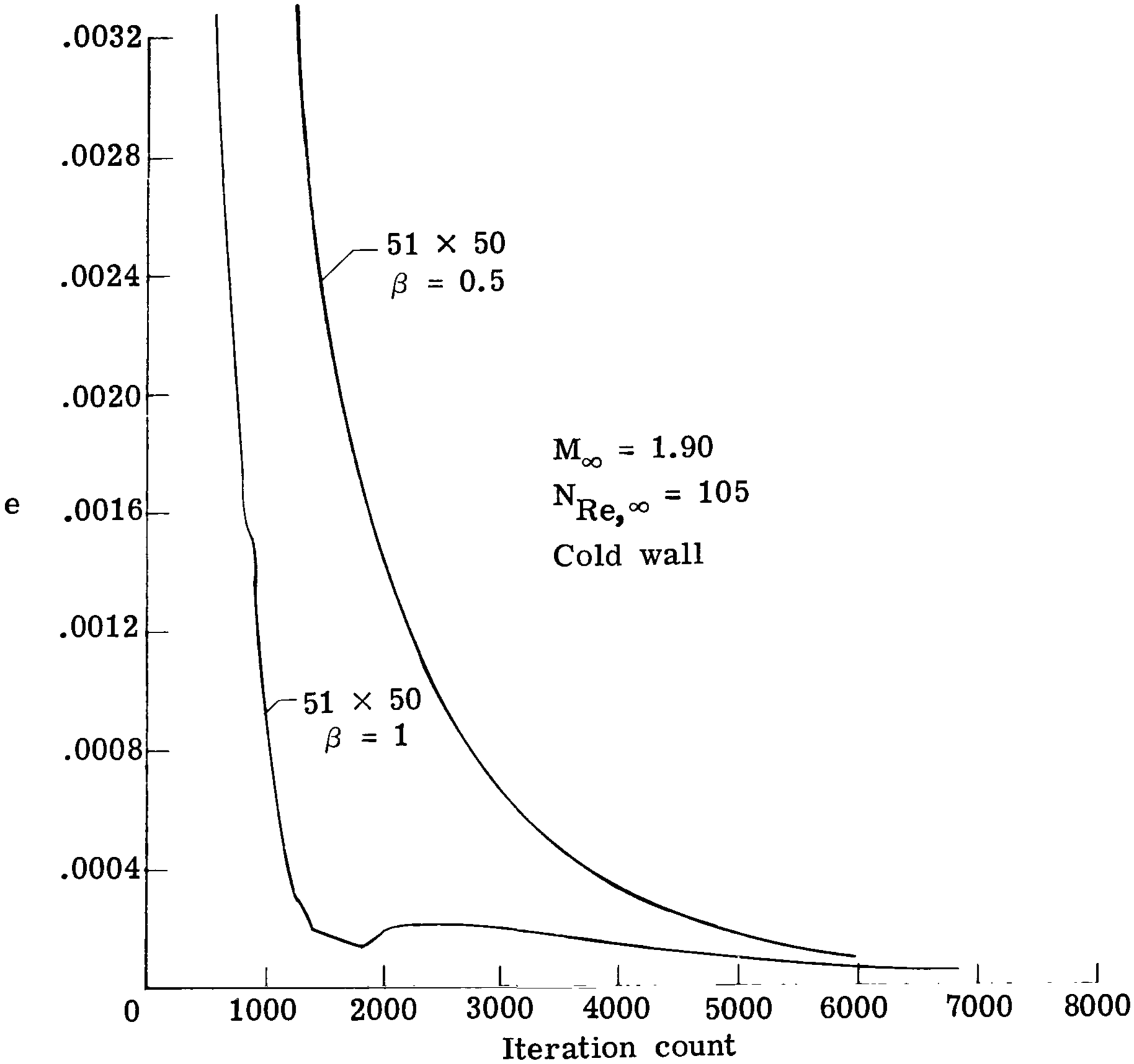

Figure 5.- Convergence test results for various mesh sizes.

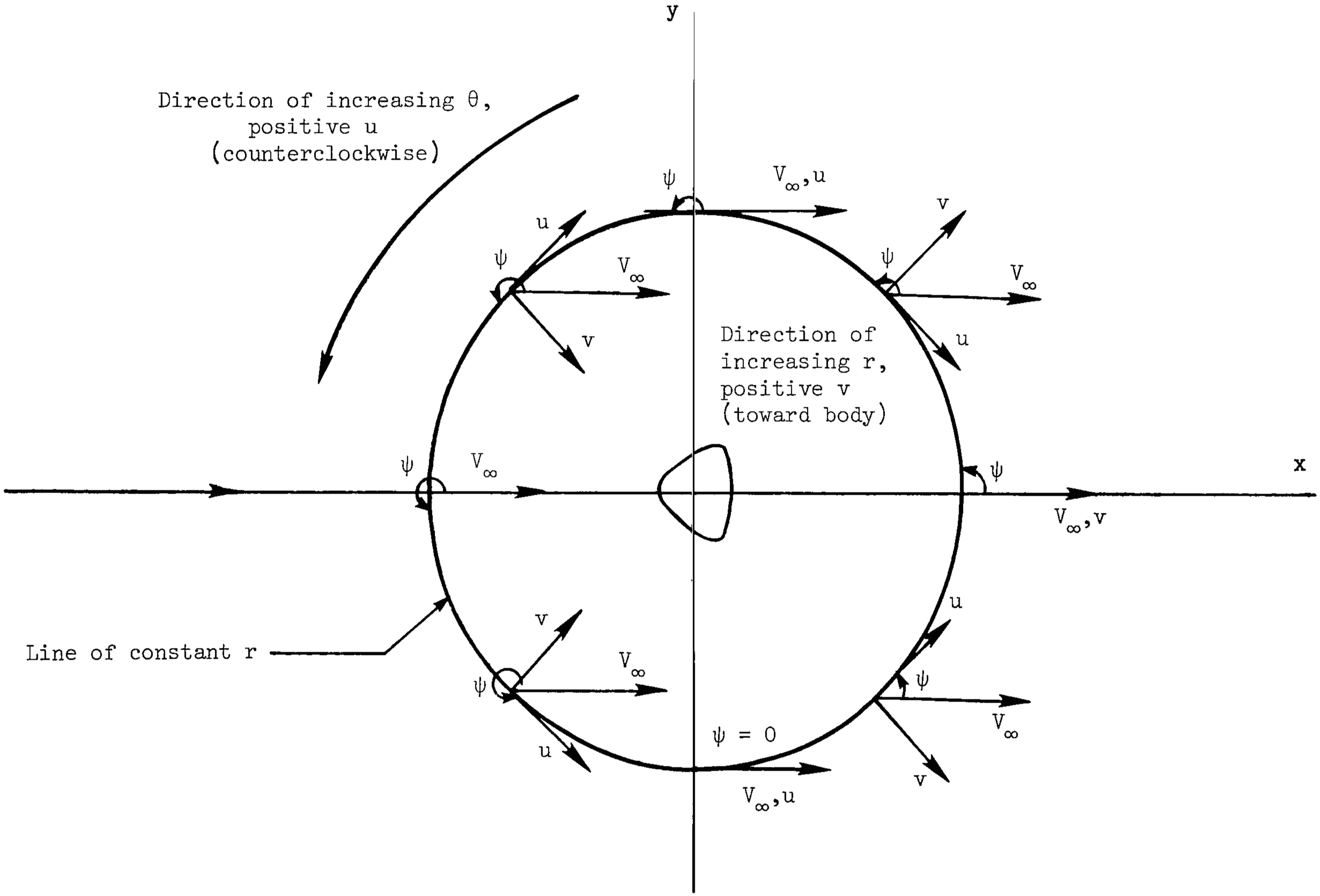

Figure 6.- Orientation of velocity vectors in transformed coordinate system.

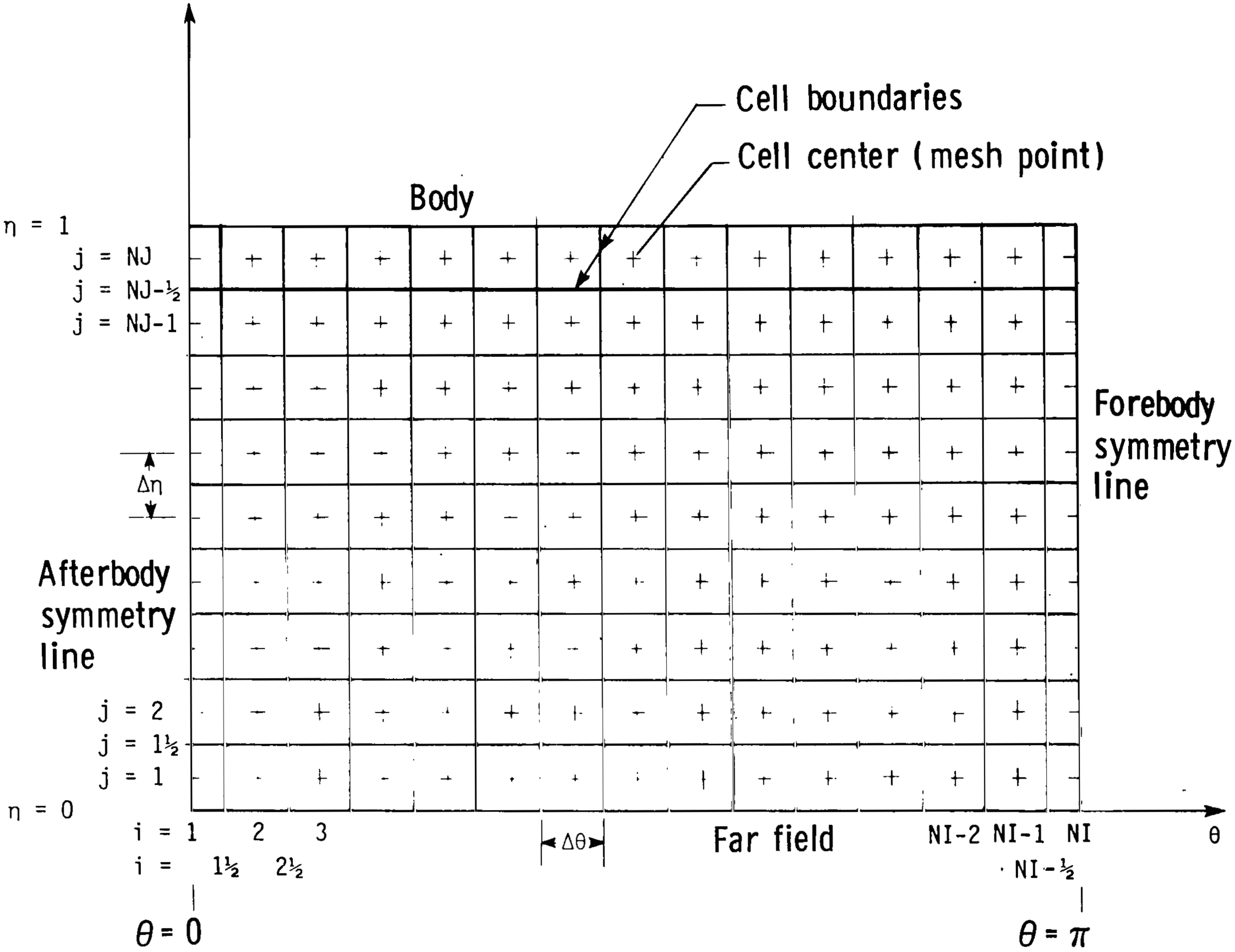

Figure 7.- Details of the (θ,η) computational plane.

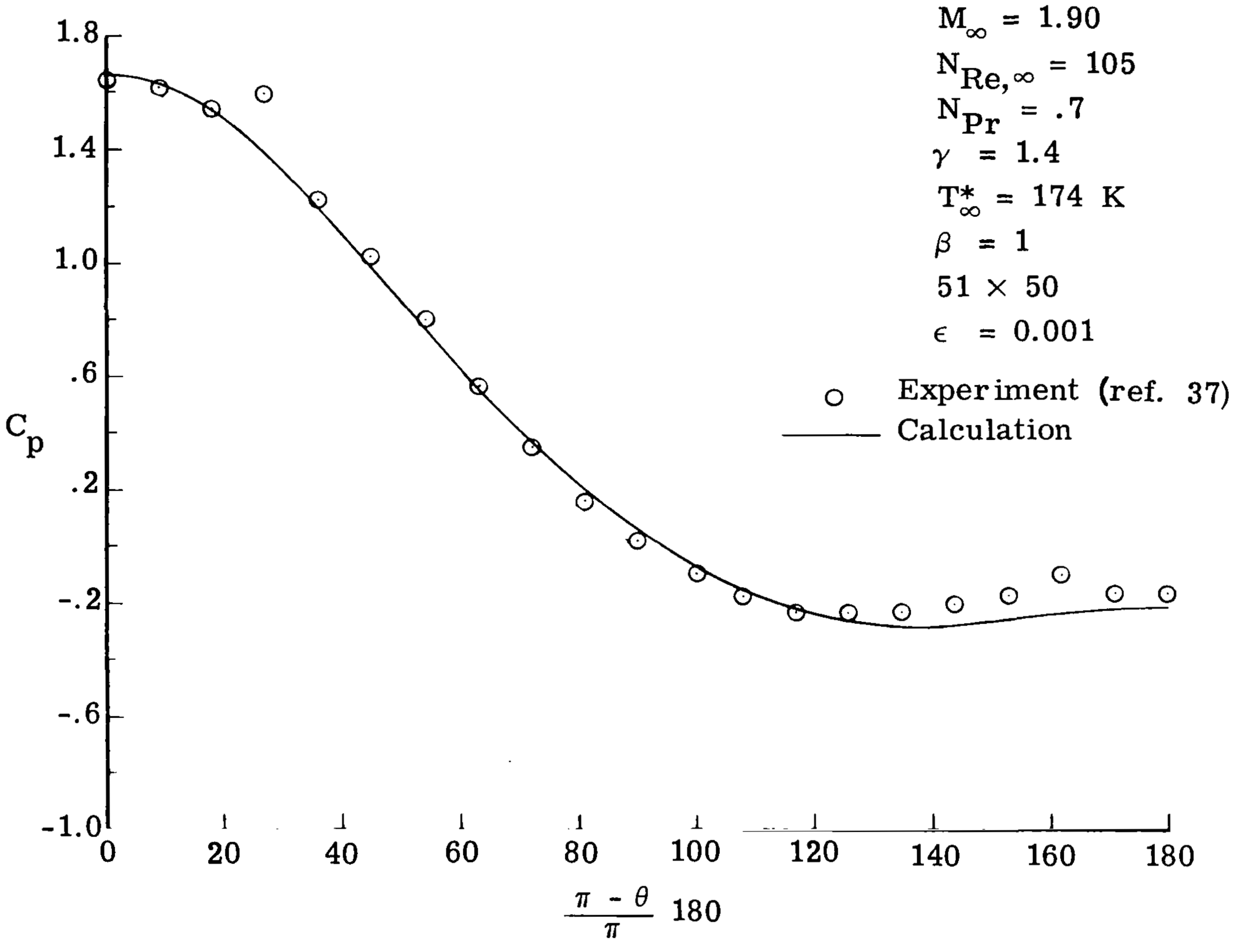

Figure 8.- Pressure coefficient distribution on cylinder with adiabatic wall.

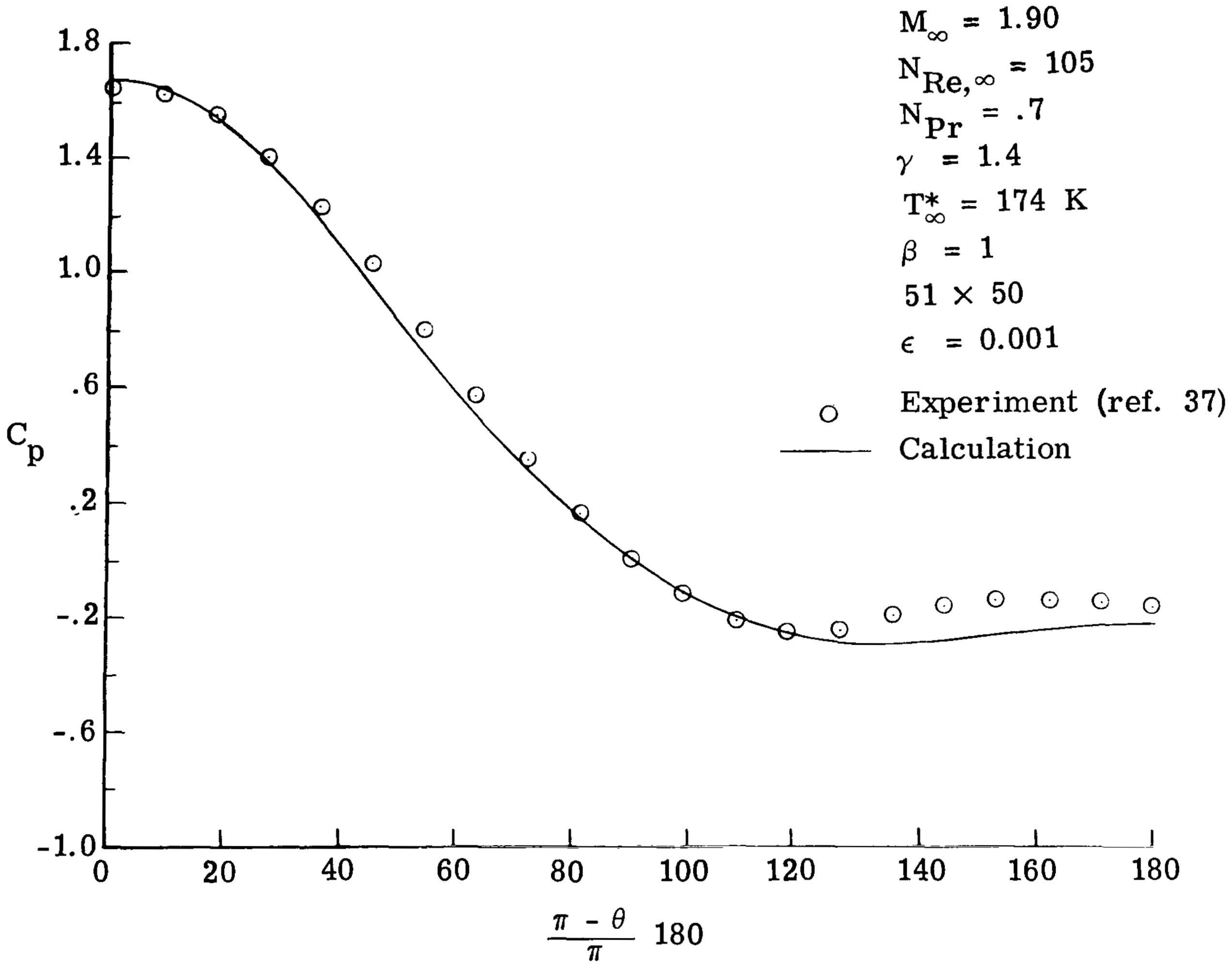

Figure 9.- Pressure coefficient distribution on cylinder with cold wall.

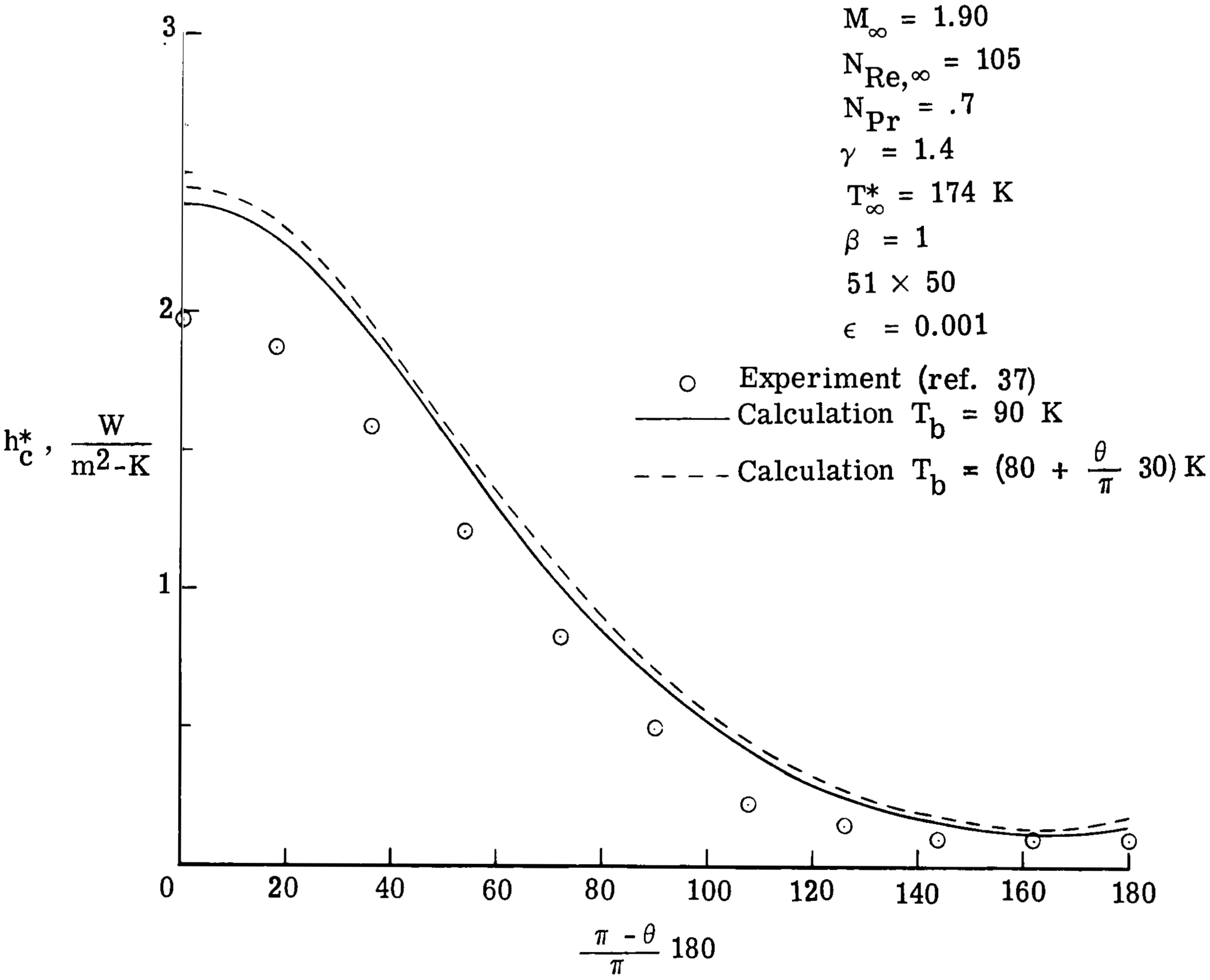

Figure 10.- Convective heat-transfer coefficient distribution on cylinder.

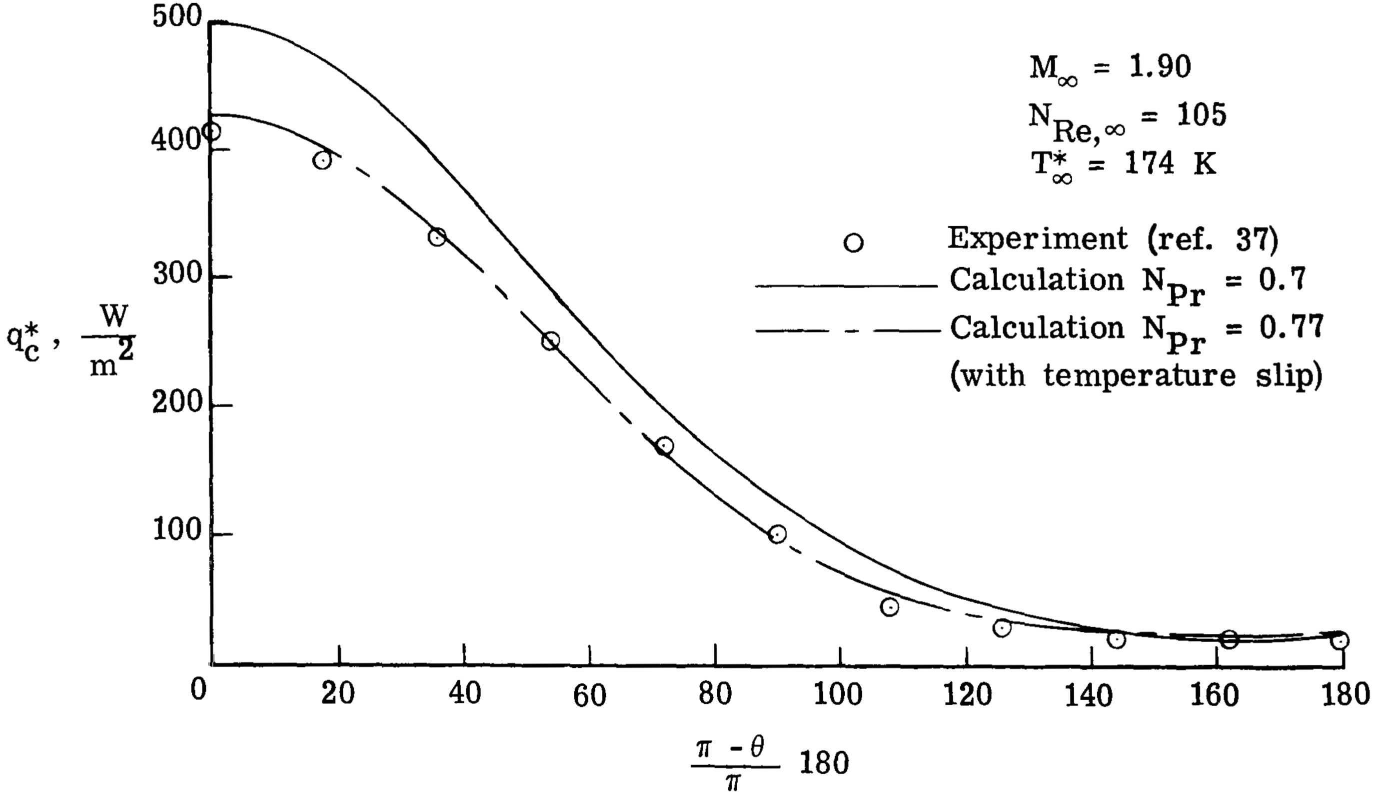

Figure 11.- Convective heat-transfer distribution on cylinder with constant wall temperature.

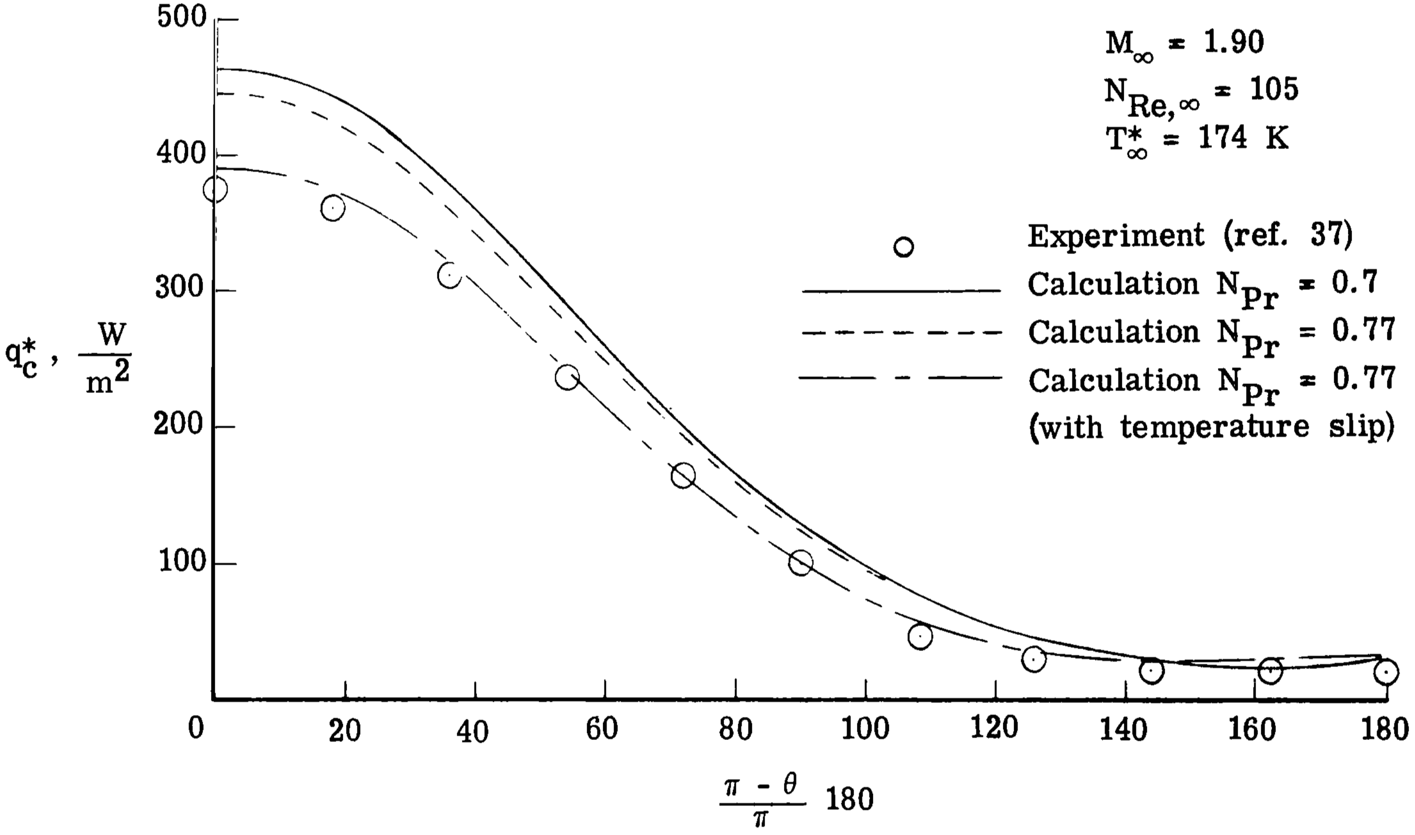

Figure 12.- Convective heat-transfer distribution on cylinder with linear wall temperature variation.

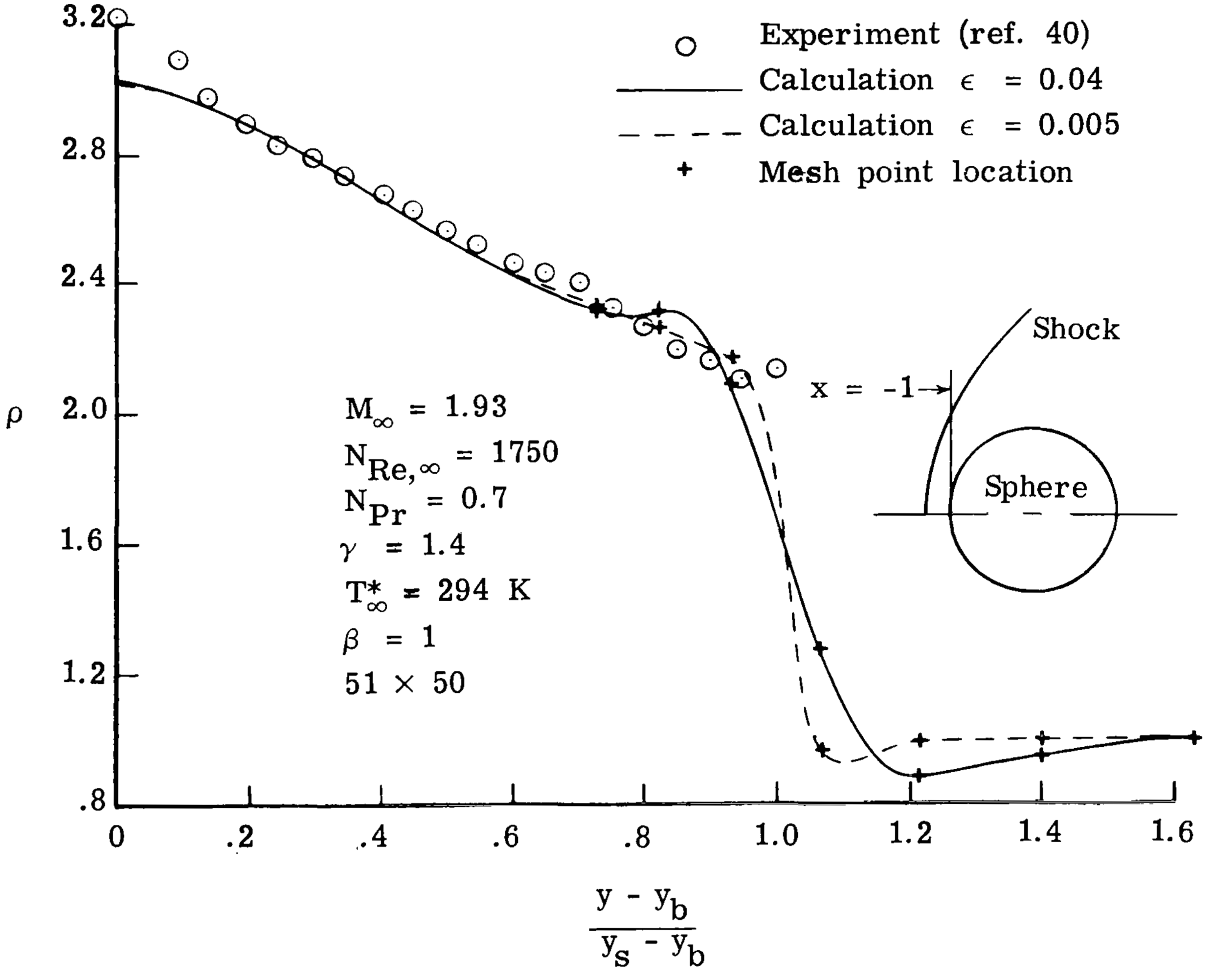

Figure 13.- Density distribution across shock layer of sphere at x = -1.

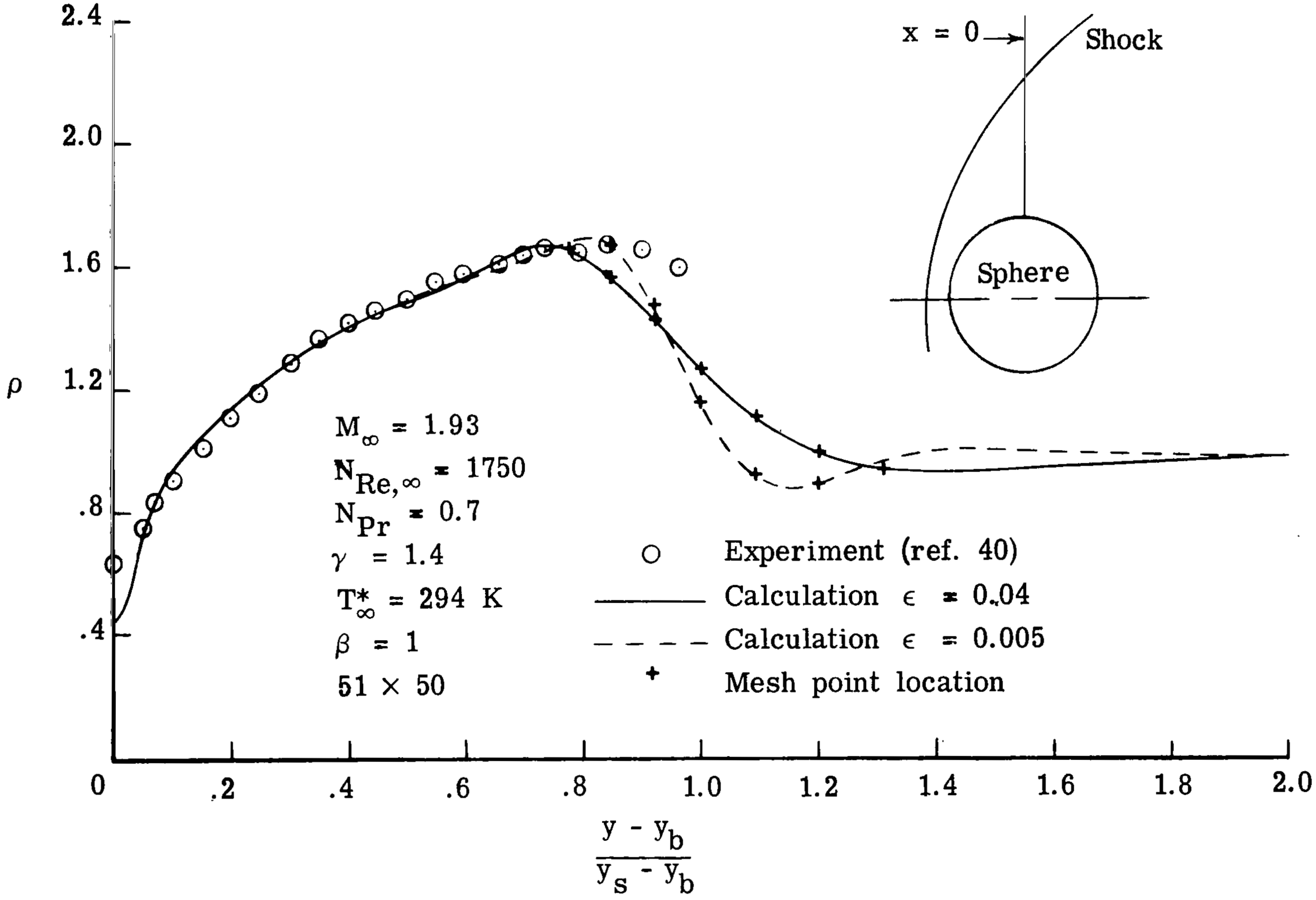

Figure 14.- Density distribution across shock layer of sphere at x = 0.

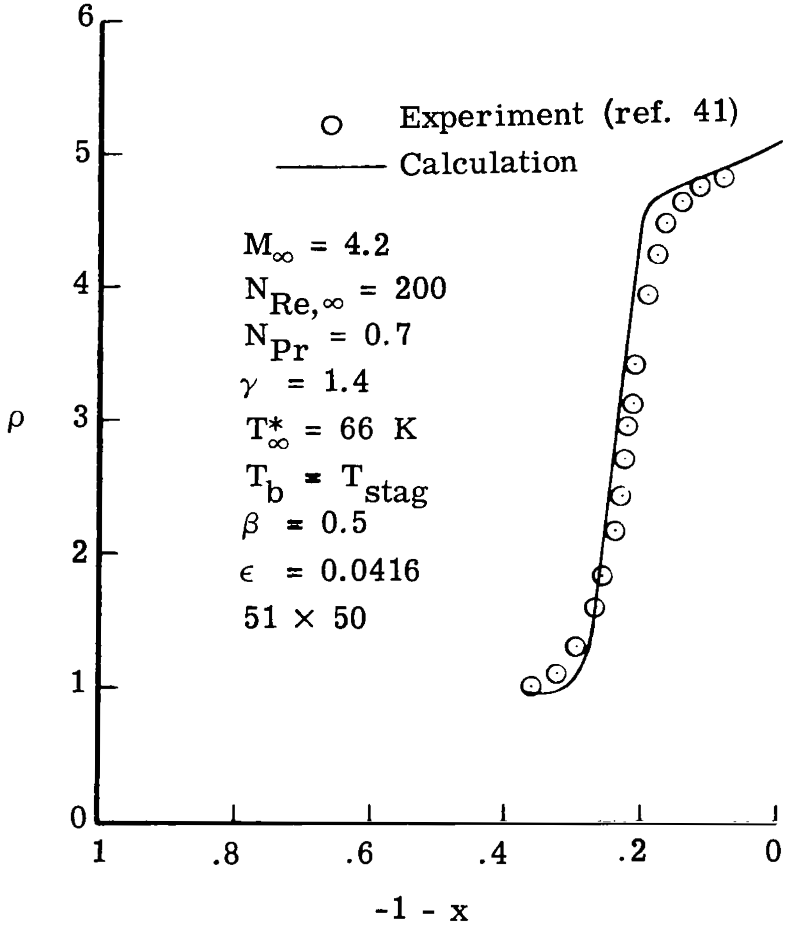

Figure 15.- Density distribution across shock layer on stagnation line with check for shock standoff distance.

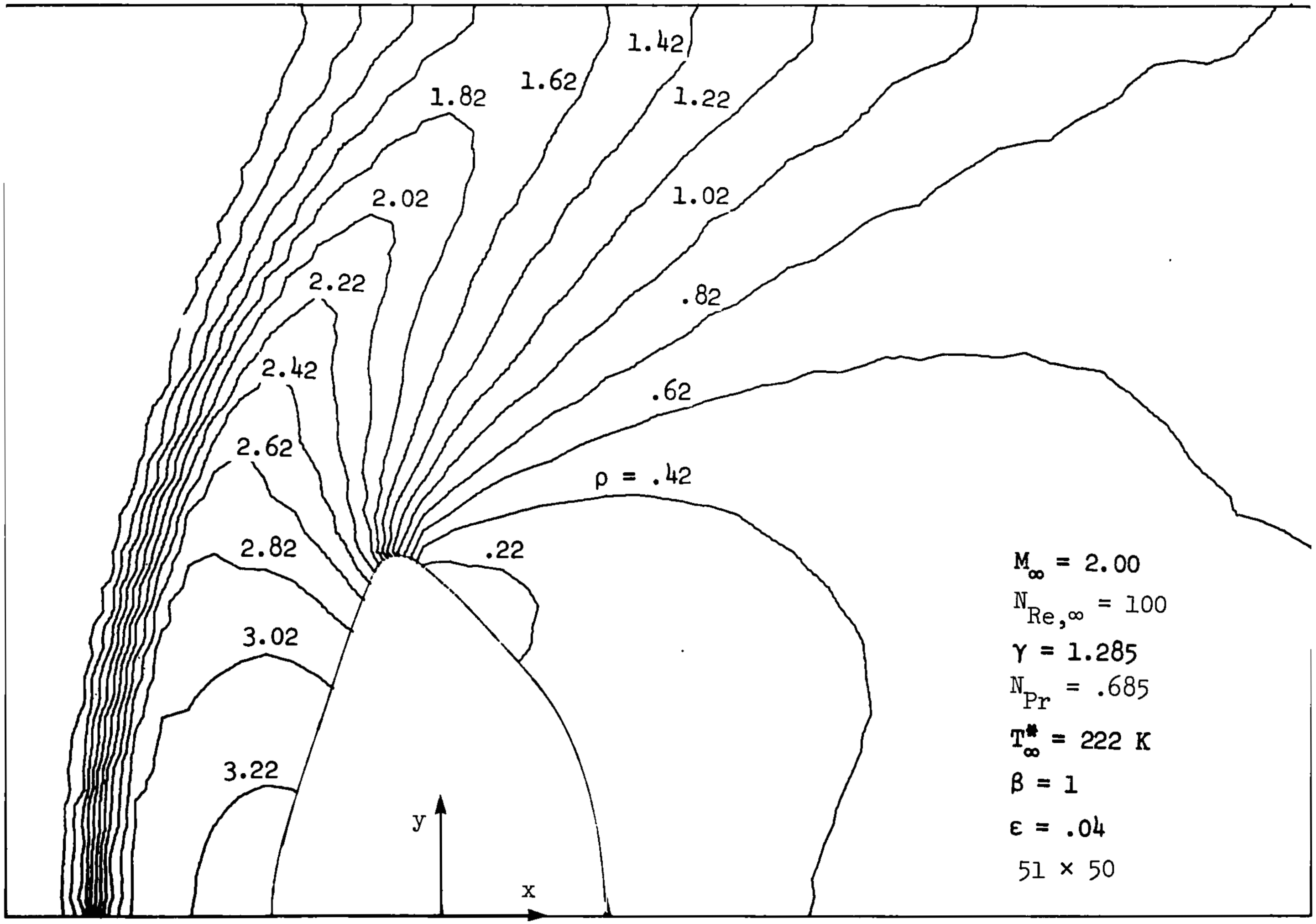

Figure 16.- Density contours over Viking aeroshell, adiabatic wall.

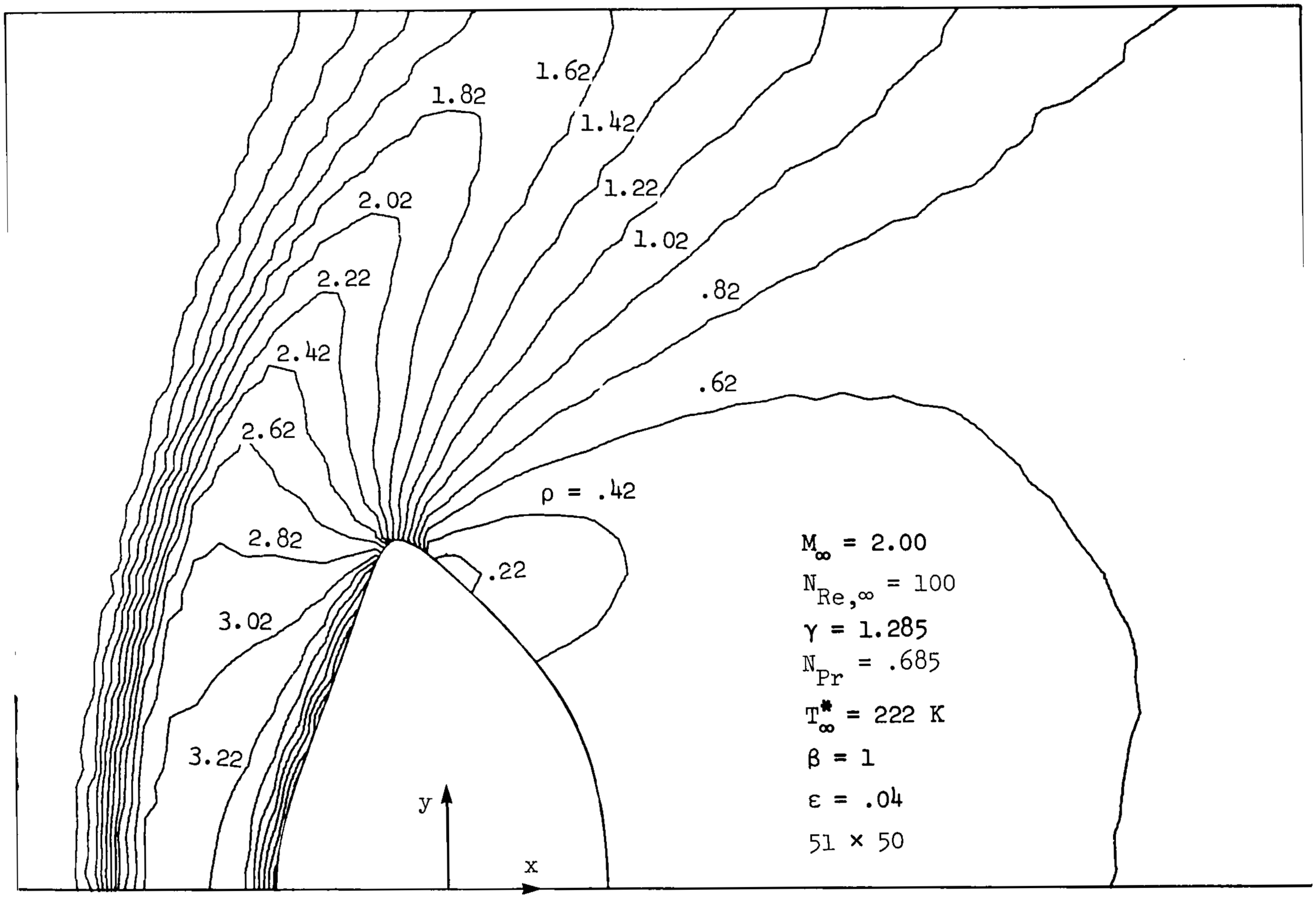

Figure 17.- Density contours over Viking aeroshell $T_w = 0.6T_{stag}$.

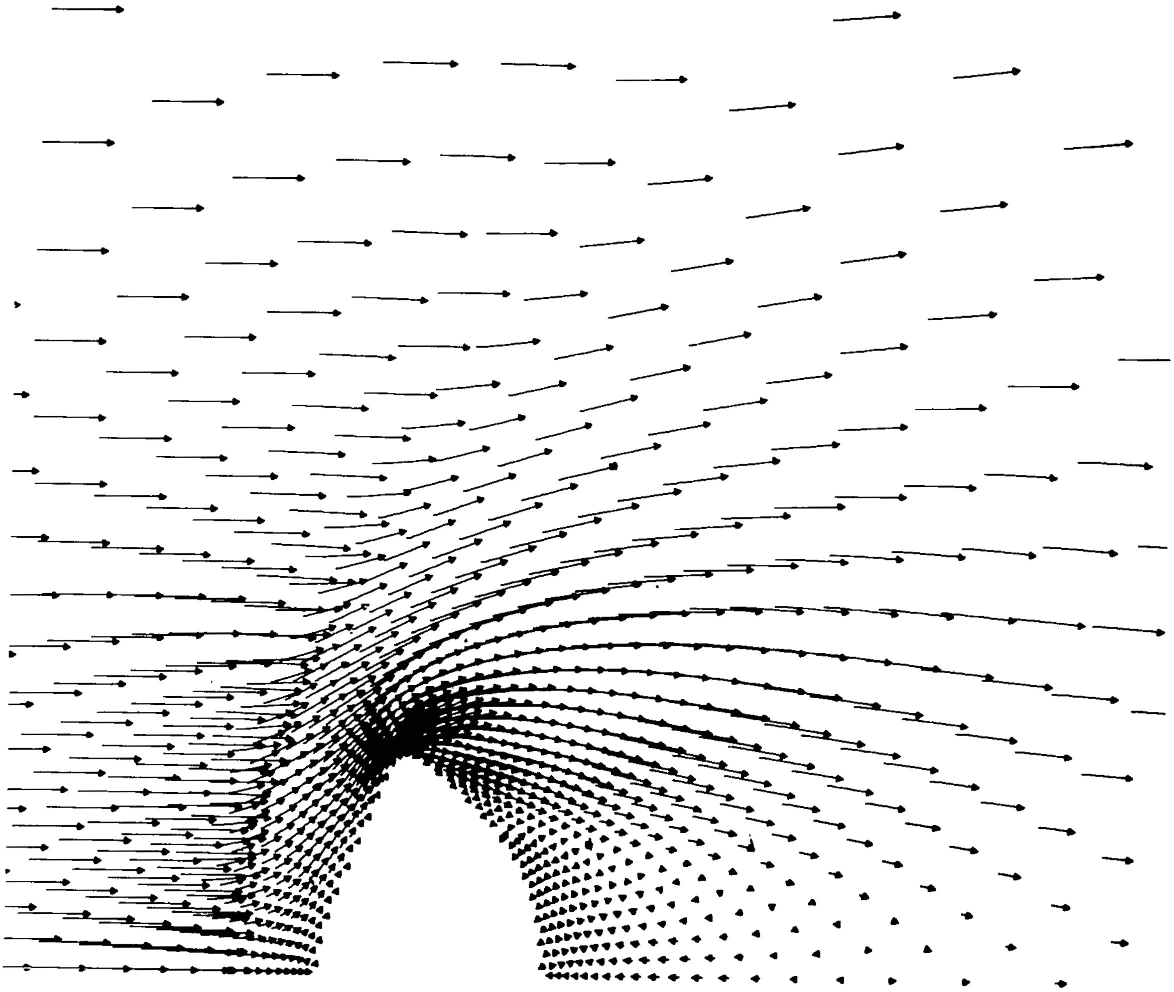

Figure 18.- Velocity vectors over Viking aeroshell.

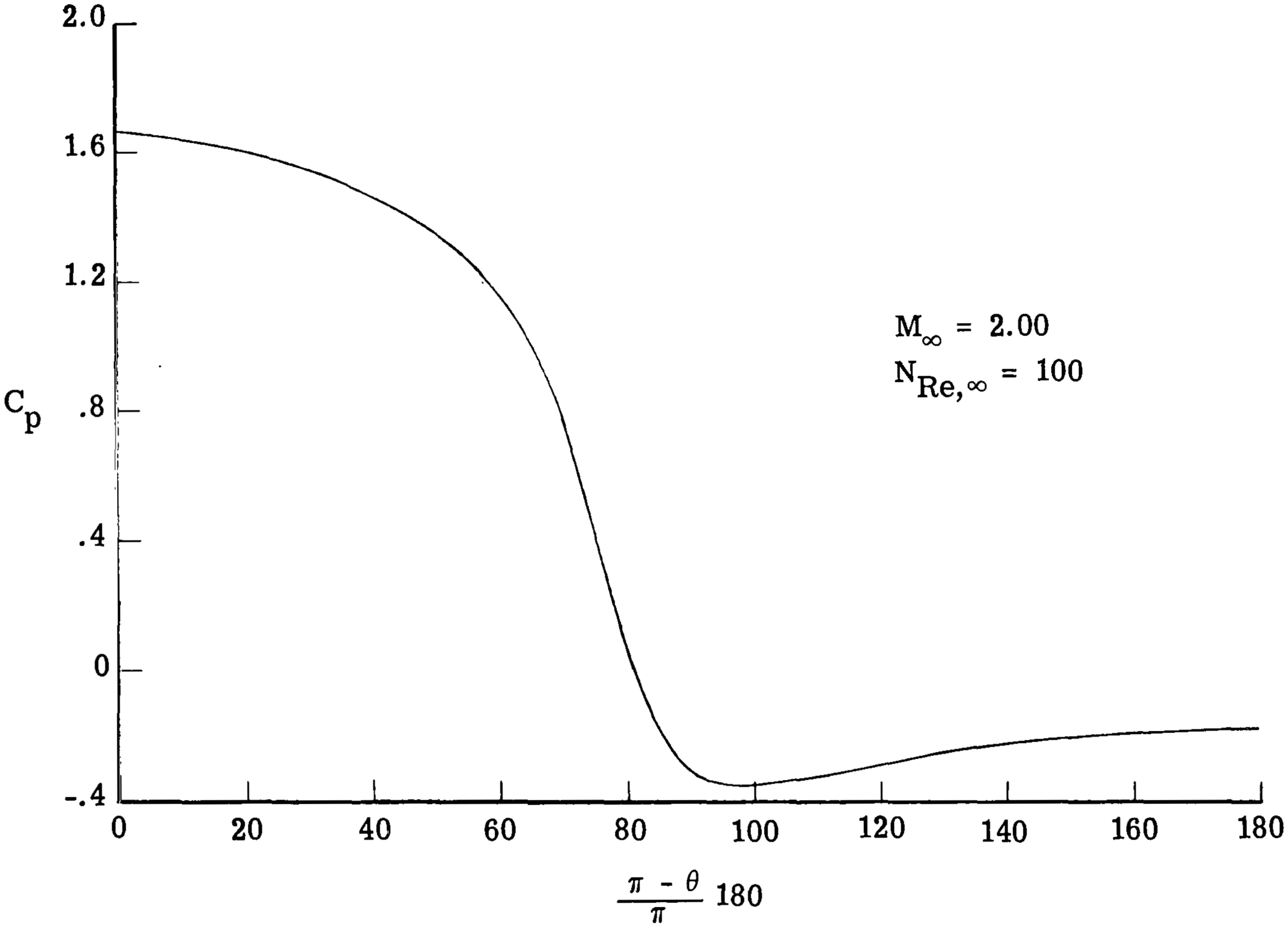

Figure 19.- Pressure coefficient distribution over Viking aeroshell (cold wall).

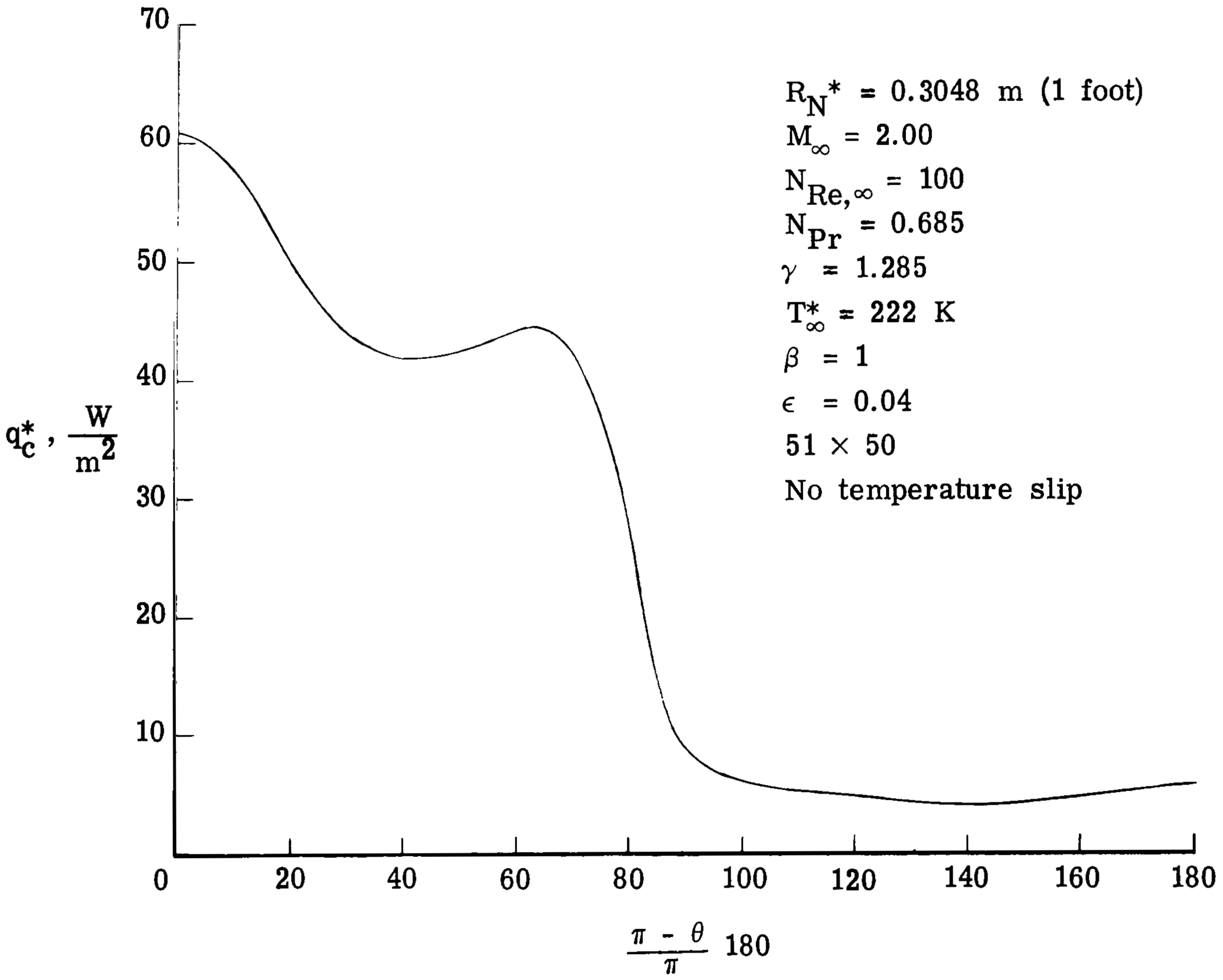

Figure 20.- Convective heat-transfer distribution over Viking aeroshell with $T_w = 0.6T_{stag}$.

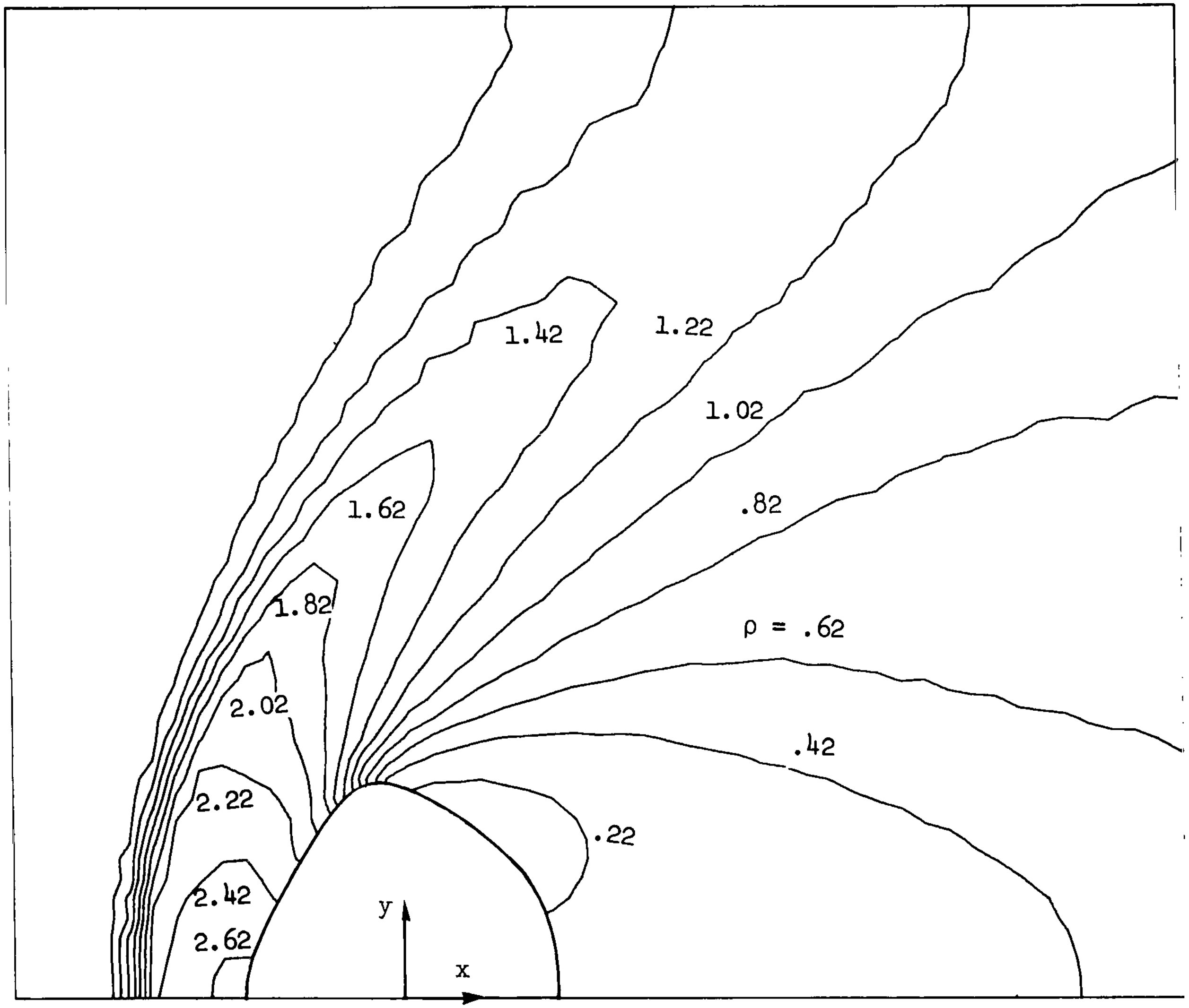

Figure 21.- Density contours over candidate configuration for Jupiter probe.

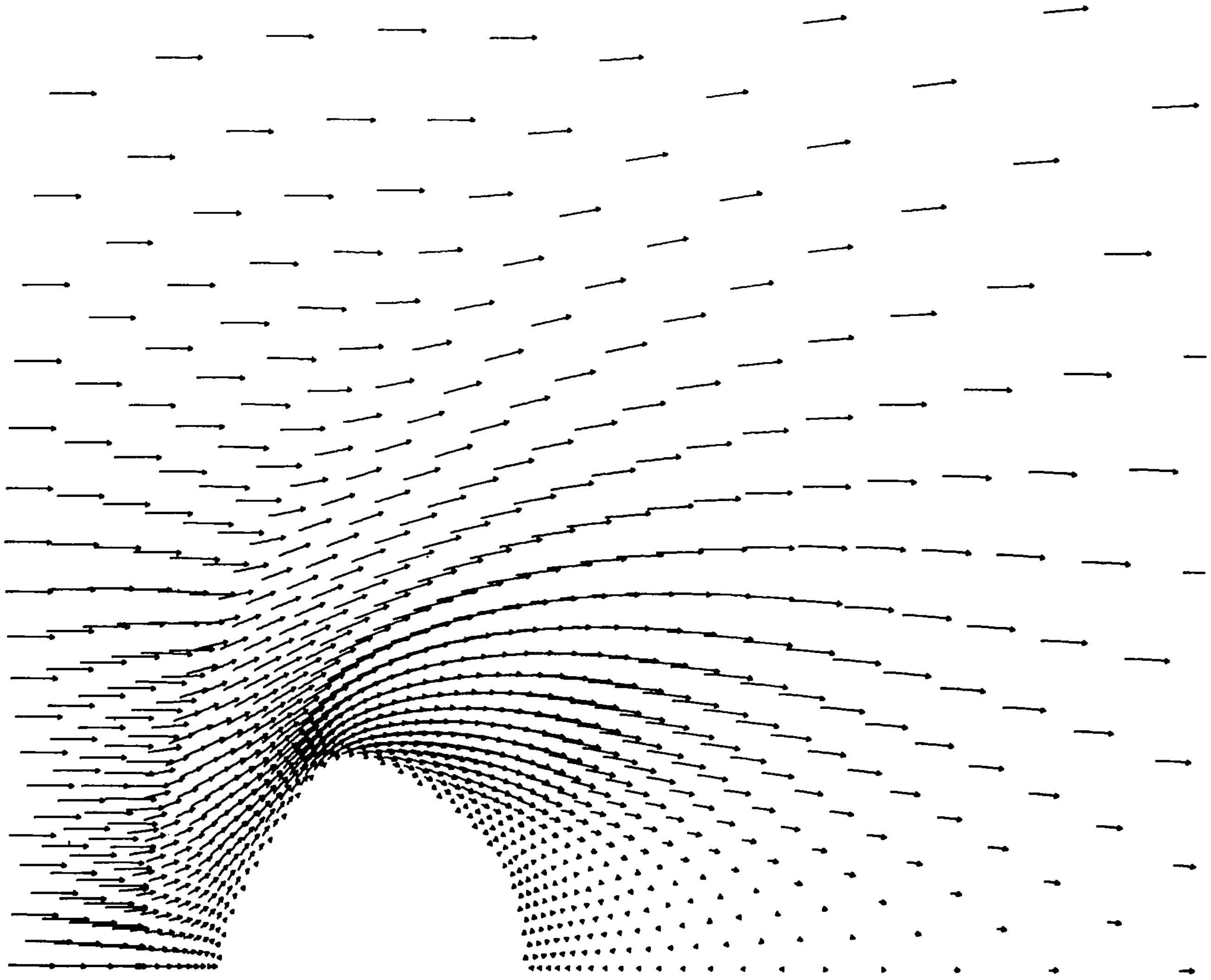

(a) Large scale view of velocity field.

Figure 22.- Velocity vectors over candidate configuration for Jupiter probe.

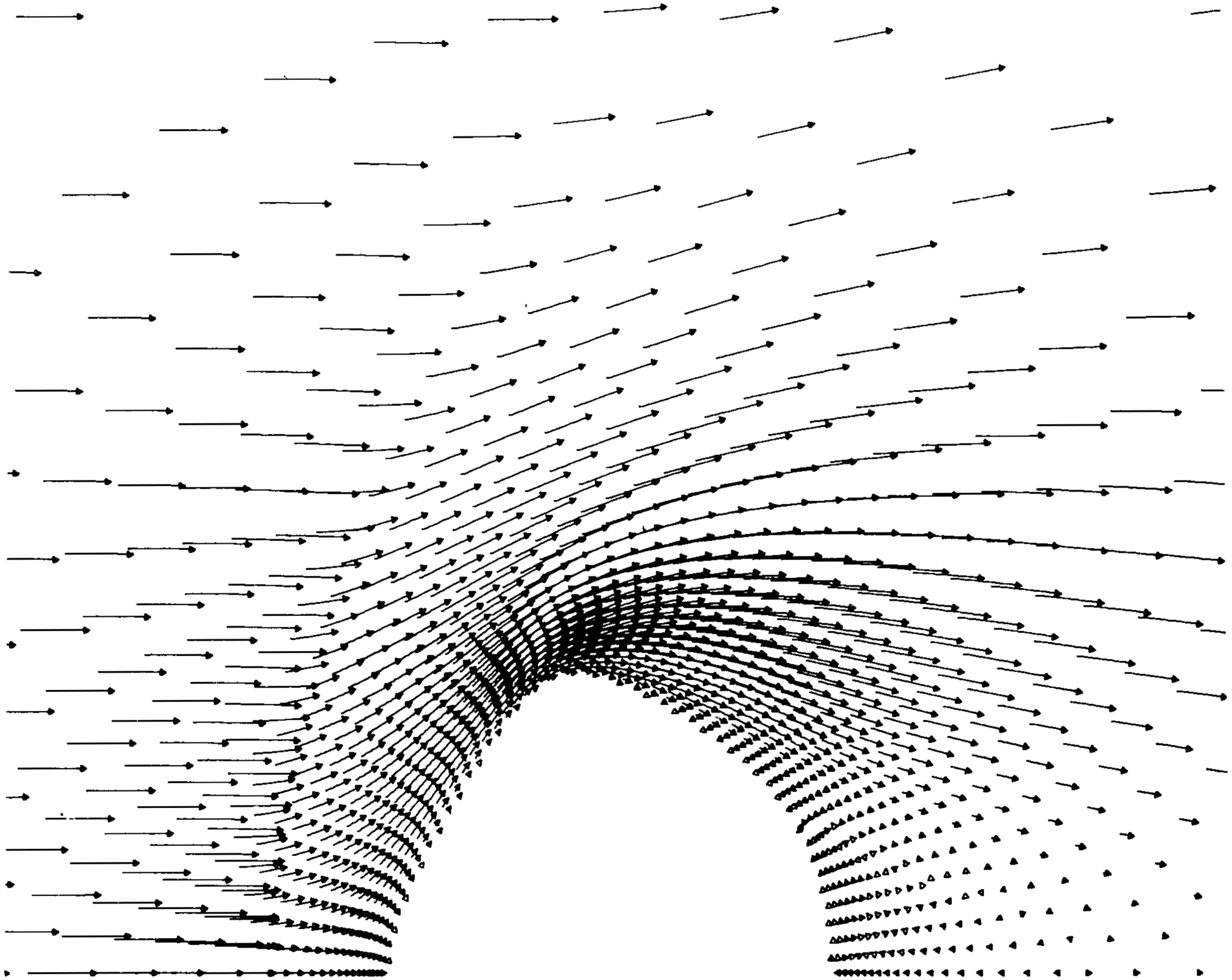

(b) Boundary-layer formation over probe.

Figure 22.- Concluded.

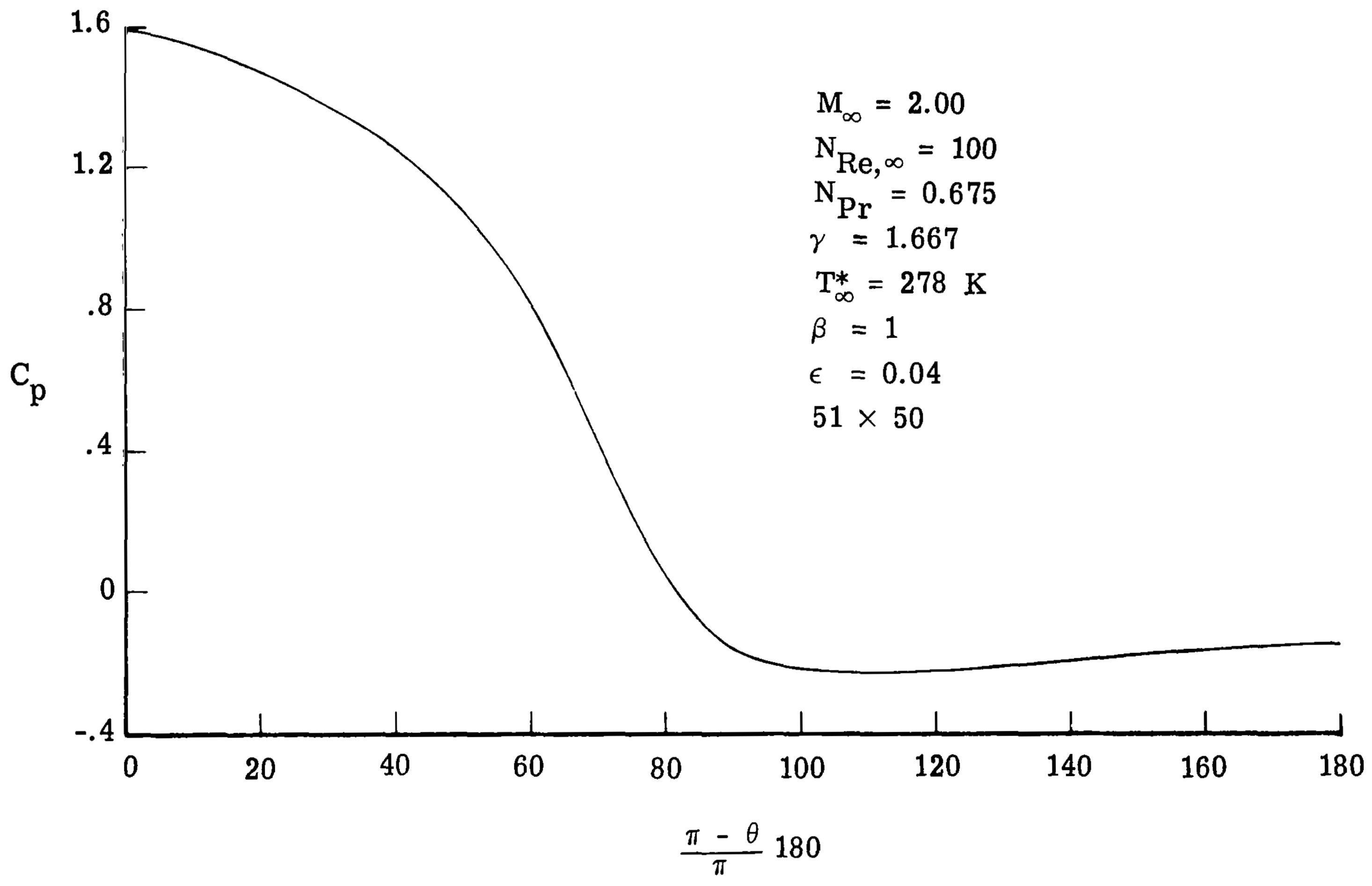

Figure 23.- Pressure coefficient distribution over candidate configuration for Jupiter probe.

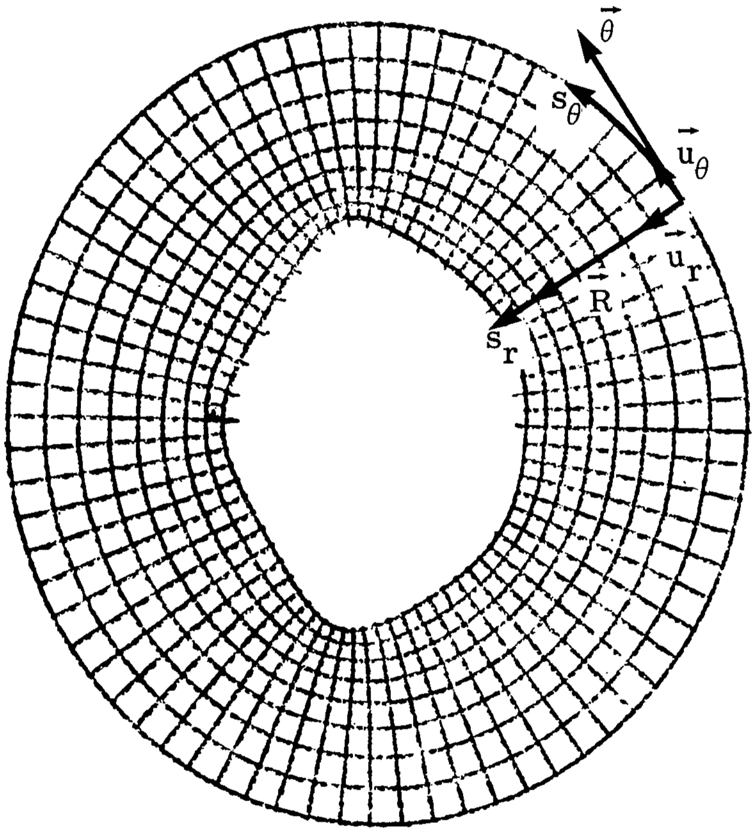

$\vec{\theta} = h_\theta \; \vec{u}_\theta$

$\vec{R} = h_r \; \vec{u}_r$

s_θ Arc length increases in counterclockwise direction

s_r Arc length increases toward body

Figure 24.- Schematic of vectors which determine metric coefficients.

1. Report No.
NASA TP-1075

2. Government Accession No.

3. Recipient's Catalog No.

4. Title and Subtitle
FOREBODY AND AFTERBODY SOLUTIONS OF THE NAVIER-STOKES EQUATIONS FOR SUPERSONIC FLOW OVER BLUNT BODIES IN A GENERALIZED ORTHOGONAL COORDINATE SYSTEM

5. Report Date
February 1978

6. Performing Organization Code

7. Author(s)
Peter A. Gnoffo

8. Performing Organization Report No.
L-11770

9. Performing Organization Name and Address
NASA Langley Research Center
Hampton, VA 23665

10. Work Unit No.
506-26-20-01

11. Contract or Grant No.

12. Sponsoring Agency Name and Address
National Aeronautics and Space Administration
Washington, DC 20546

13. Type of Report and Period Covered
Technical Paper

14. Sponsoring Agency Code

15. Supplementary Notes
Material presented herein is revision of a thesis entitled "Solutions to the Navier-Stokes Equations for Supersonic Flow Over Blunt Bodies in a Generalized Orthogonal Coordinate System" submitted in partial fulfillment of the requirements for the degree of Master of Science, George Washington University, April 1977.

16. Abstract

A coordinate transformation developed in NASA TM X-3468, which can approximate many different two-dimensional and axisymmetric body shapes with an analytic function, is used as a basis for solving the Navier-Stokes equations for the purpose of predicting 0° angle-of-attack supersonic flow fields. The transformation defines a curvilinear, orthogonal coordinate system in which coordinate lines are perpendicular to the body and the body is defined by one coordinate line. This system is mapped into a rectangular computational domain in which the governing flow-field equations are solved numerically. Advantages of this technique are that the specification of boundary conditions are simplified and, most importantly, the entire flow field can be obtained, including flow in the wake. Good agreement has been obtained with experimental data for pressure distributions, density distributions, and heat transfer over spheres and cylinders in supersonic flow. Approximations to the Viking aeroshell and to a candidate Jupiter probe are presented and flow fields over these shapes are calculated.

17. Key Words (Suggested by Author(s))
Navier-Stokes equations
Coordinate transformation
Blunt body
Wake flow
Supersonic flow

18. Distribution Statement
Unclassified - Unlimited

Subject Category 34

19. Security Classif. (of this report)	20. Security Classif. (of this page)	21. No. of Pages	22. Price*
Unclassified	Unclassified	88	$6.00

* For sale by the National Technical Information Service, Springfield, Virginia 22161

NASA-Langley, 1978

National Aeronautics and
Space Administration

Washington, D.C.
20546

Official Business
Penalty for Private Use, $300

THIRD-CLASS BULK RATE

8 1 1U,D, 012378 S00903DS
DEPT OF THE AIR FORCE
AF WEAPONS LABORATORY
ATTN: TECHNICAL LIBRARY (SUL)
KIRTLAND AFB NM 87117

NASA

POSTMASTER: If Undeliverable (Section 158
Postal Manual) Do Not Return